UNIVERSITÄT PADERBORN
Die Universität der Informationsgesellschaft

FAKULTÄT FÜR
ELEKTROTECHNIK,
INFORMATIK UND
MATHEMATIK

Modeling, Optimization and Control Design for LCC Resonant Converter Applied in Very Low Frequency High Voltage Generator

Von der Fakultät für Elektrotechnik, Informatik und Mathematik
der Universität Paderborn

zur Erlangung des akademischen Grades

Doktor der Ingenieurwissenschaften (Dr.-Ing.)

genehmigte Dissertation

von

M.Sc. Manli Hu

Erster Gutachter: Prof. Dr.-Ing. Joachim Böcker
Zweiter Gutachter: Prof. Dr.-Techn. Felix Gausch

Tag der mündlichen Prüfung: 23.01.2014

Paderborn 2014

Diss. EIM-E/296

Declaration

I confirm that the work submitted in this dissertation is the result of my own investigation and all the sources I have used or quoted have been acknowledged by means of complete references.

Paderborn, July 09, 2013

Manli Hu

to my loving parents, husband and sons.

Acknowledgments

The work submitted in this dissertation has been carried out based on my research during the period as I was a scientific co-worker in the department of Power Electronics and Electric Drives (LEA) of Paderborn University, Germany.

Firstly, I would like to express my sincerely high appreciation to my advisor - Prof. Dr.-Ing. Joachim Böcker. His profound knowledge, extensive vision and creative viewpoint have been the source of my inspiration for the Ph.D work. His strict working style, meticulous scientific research attitude are always my exemplar for the future work.

I'd like to thank Dr.-Ing. Norbert Fröhleke sincerely. Six years before, he provided me the original opportunity, which let me have the chance to work in LEA. During all the time, he is like an expostulator, give me help, guidance and support.

I would like to thank Prof. Dr.-techn. Felix Gausch, as an important member of the committee, he offered much time and effort to review my manuscript, gave me good advices and suggestions. I also want to thank all of the other committee members.

It has been a great pleasure to work in the group of LEA, and to work with such talented, hard-working and creative colleagues. I would like to thank all of them, their friendships and help make my stay at LEA pleasant and enjoyable. This is a happy reminiscent stage in my life.

I also want to thank the administrative and technical co-workers of LEA for their great help. Special thanks are due to Mr. Norbert Sielemann for his hard-work on the laboratory prototype.

Thanks belong to the European Community for funding the PRC-HVTS-DCS

project as well as our project partners. Especially, I would like to thank Mr. Philipp Rekers for his great help and support.

I'd like to give my sincere thanks to my parents. They gave me life, offered me the opportunity to be educated, always supported me with their love and encouragement throughout my life.

At last but not the least, I would like to thank my husband - Rongyuan Li, he is always be there with his love, encouragement, understanding and support, especially in the difficult period of my doctoral study; I'd like to thank my sons - Xianquan and Xianhan, they gave me power, arouse my potential to overcome all the handicap.

Kurzfassung

Durch die breite Anwendung von Hochspannungskabeln heutzutage gewinnt ihr Test der kompletten Funktionalität und Isolierung mehr und mehr an Bedeutung. Das Testverfahren mit sehr niedriger Frequenz hat sich als eine bevorzugte Methode herausgestellt. Untersuchungen zeigten, dass es noch viele technische Hindernisse für die Entwicklung solcher Hochspannungs-Prüfgeneratoren (HVTS) gibt. Die Europäische Kommission finanziert diese Arbeit zugrunde liegende Projekt RPC-HVTS-DCS, um diese technischen Herausforderungen zu lösen.

Ziele dieser Dissertation sind, Modellierung der qualifiziertesten Schaltung für HVTS und Ermittlung der stationären und dynamischen Eigenschaften, modellbasierter mehrzielen Entwurfsoptimierung, und Verbesserung der Systemsteuerung durch Anwendung verschiedener Regelungsverfahren.

Literaturrecherchen zeigen, dass ein Serien-Parallel (LCC) Resonanzwandler mit Hochspannungs-Transformator, mehrstufigem symmetrischem Spannungsvervielfacher Gleichrichter (Greinacher Kaskade) im positiven und negativen Zweig, eine geeignete Topologie für HVTS-Anwendung ist.

Die wichtigsten Ergebnisse dieser Arbeit sind wie folgt zusammengefasst.

1. Hinsichtlich stationärer und dynamischer Aspekte kann ein mehrstufiger symmetrischer Greinacher Kaskade Gleichrichter wie ein einstufiger symmetrischer Greinacher Kaskade Gleichrichter unter Berücksichtigung des Spannungsabfalls und der Kapazitäten angenähert werden.

2. Eine Groß- und Kleinsignal-Modellierung des LCC Resonanzwandlers mit kapazitiver Last und äquivalenter Spannungsquellelast wurde durchgeführt. Der Vergleich der Dynamik zeigt, dass nur minimale Abweichungen auftreten, vor allem dann, wenn die kapazitive Last groß ist.

3. Basierend auf Großsignalmodell und Verlustmodell des LCC Resonanzwandlers, wurde eine Umgebung für den automatisierten Entwurf per Mehrzieloptimierung aufgebaut.

4. Verschiedene Regelungsschema wurden untersucht:

   (a) Ein herkömmlicher linearer Proportional-Integral-Regler wurde wegen seiner einfachen Struktur, einfachem Design und der geringen Kosten zuerst betrachtet. Simulierte und experimentelle Ergebnisse bestätigen die Richtigkeit der Entwicklung. Aber seine lineare Steuerungsstruktur entspricht der nichtlinearen Natur der Regelstrecke nicht, weshalb die Regelergebnisse in hohem Maße abhängig vom Betriebspunkt sind.

   (b) Fuzzy-Logik-Regelungen haben die Fähigkeit, Nichtlinearitäten zu handhaben und werden deshalb als Alternative zu linearen Steuerungen entwickelt. Obwohl simulierte und experimentelle Ergebnisse die Machbarkeit zeigen, ist die Regelqualität nicht besser als die des linearen Reglers.

   (c) Die modellbasierte Takagi-Sugeno (T-S) Fuzzy-Regelung wurde für diese Anwendung weiter entwickelt, um nicht nur Stabilität sondern auch hohe Regelqualität zu garantieren. Simulierte Ergebnisse zeigen die hervorragende Regelleistung: kürzere Einschwingzeit, hohe Regelbandbreite, keine statische Regelabweichung. Basierend auf einem herabskalierten Labormuster wurden experimentelle Ergebnisse ebenfalls gewonnen, um die Richtigkeit der Berechnungen und Simulationen zu überprüfen. Es sollte betont werden, dass solche modellbasierte T-S Fuzzy-Regelung Entwicklung ein origineller Beitrag in der Stromversorgung Gebiet mit realisierten Messungen ist.

Die vorgeschlagene Modellierung, Mehrzieloptimierung und Regelungsentwurf eignen sich nicht nur für LCC Resonanzwandlers in HVTS Anwendungen, sondern auch für Anwendungen mit Resonanzkonvertern für die Erzeugung hoher Spannungen für Röntgen-Generatoren und DC-Netzteile mit weitem Ausgangsspannungsbereich geeignet.

Abstract

Due to the wide application of high voltage cables nowadays, their test of fully functionality and insulation becomes more and more important. Very low frequency (VLF) high voltage (HV) generators are thought to be a preferable equipment to implement the test. Previous investigations showed many technical obstacles for further development of VLF HV generators, the European Commission funded the underlying project "PRC-HVTS-DCS" to this thesis to solve these technical challenges.

The purpose of this dissertation is to investigate the steady-state and dynamic characteristics of VLF HV generator through modeling of the most qualified topology, realize model-based multi-objective optimization to yield an economic and technical sound solution, and improve system control performance based on various control schemes research.

Literatures show that the circuit consisting of series-parallel (LCC) resonant converter with step-up high voltage transformer, multi-stage symmetrical Cockcroft-Walton (CW) multiplier in the positive and negative rail is an appropriate topology for VLF HV generators.

The main achievements of this dissertation are summarized as follows.

1. Regarding both steady-state and dynamic aspects, a multi-stage symmetrical CW multiplier can be approximated as the corresponding one-stage symmetrical CW multiplier with consideration of predictable voltage drop and accommodated CW capacitances.

2. Large-signal modeling and small-signal modeling of the LCC resonant converter with capacitive load and equivalent voltage source load are implemented. Their comparison shows that only minor deviation occur; especially, when the original capacitive load is large.

3. Based on LCC resonant converter large-signal model and loss model, a computer aided design and multi-objective optimization environment is developed, which provides a graphical guideline for practical implementation.

4. Various control schemes are investigated:

   (a) Conventional model-based linear proportional-integral controller is primarily developed due to its simple structure, ease of design and low cost. Its simulated and experimental results validate the correctness of mathematical modeling and control design. But its linear control structure does not agree with the nonlinear system nature, its control performance is highly dependent on the operating point.

   (b) Fuzzy logic control has the ability to handle nonlinearities and has been developed as an alternative to the former linear control. Although simulated and experimental results show its feasibility, its control performance has no predominant advantage compared to those of the linear controller.

   (c) A model-based Takagi-Sugeno (T-S) fuzzy controller is further developed in order to find a more advanced controller, which guarantees not only stability but also the closed loop control performance. Simulated results demonstrate the outstanding control performance: shorter settling time, wider control bandwidth, no static error. Based on a scaled-down laboratory prototype, experimental results are also provided to validate its correctness. It should be highlighted that such model-based T-S fuzzy control development is an original contribution, which adopts a nonlinear model-based fuzzy control scheme in power supply field with realized prototype measurements.

The proposed modeling, multi-objective optimization and control design are not only suitable for the LCC resonant converter applied in VLF HV generator application, but also appropriate for other applications using resonant converters, such as high voltage X-Ray generator, DC power supplies with wide output voltage range.

Nomenclature

A_c	Core cross-sectional area
ΔB	Peak AC flux density
C	Capacitor's value in CW multiplier
C_g	Parallel capacitor of C_s and C_p
C_{g1}	Capacitor in CW multiplier
C_L	Load capacitor
C_p	Parallel resonant capacitor
C_s	Series resonant capacitor
C_{s1}	Capacitor in CW multiplier
d	Duty cycle
D	Steady-state duty cycle
f_0	Resonant frequency
f_m	Modulation frequency
f_n	Normalized frequency
f_s	Switching frequency
f_{sn}	Normalized switching frequency
F_s	Steady-state switching frequency

G_{d0}	Low-frequency gain in duty cycle control mode
G_{f0}	Low-frequency gain in frequency control mode
h	Thickness of a square conductor
H_0	Magnetic field strength on the left side of the conductor
H_h	Magnetic field strength on the right side of the conductor
i_c	Reference signal of output current
i_{cw}	Output current of CW multiplier
Δi_{cw}	Small-signal output current of CW multiplier
i_{cw+}	Positive CW multiplier output current
i_{cw-}	Negative CW multiplier output current
i_{est}	Estimated output current
i_L	Resonant current in LCC tank
i_{Lc}	1st-order Fourier coefficients of resonant current i_L
i_{Leff}	RMS value of resonant current i_L
$i_{Leff}*$	Reference signal of effective resonant current i_L
i_{Lp}	Amplitude of resonant current i_L
i_{Ls}	1st-order Fourier coefficients of resonant current i_L
i_{out}	Output current
i_p	Current flowing through C_p
I_B	Fictive current
I_{cw}	Steady-state output current of CW multiplier
I_{Davg}	Average current flowing through the anti-parallel diode of MOSFET

I_{Drms}	Effective current flowing through the anti-parallel diode of MOSFET
I_{Lc}	Quasi-steady-state solution of i_{Lc}
I_{Leff}	Steady-state i_{Leff}
I_{Lp}	Steady-state i_{Lp}
I_{Ls}	Quasi-steady-state solution of i_{Ls}
I_{Moff}	Turn-off current of MOSFET
I_{Mrms}	Effective current flowing through MOSFET
I_{tot}	Total RMS winding current
k	Stage number of Cockcroft-Walton multiplier
K_u	Winding fill factor
l_m	Core mean magnetic path length
L_d	Loop gain in duty cycle control mode
L_f	Loop gain in frequency control mode
L_s	Series resonant inductor
m	Ratio of the magnetomotive force $F(h)$ to the layer ampere-turns N_pI_rms
M	Voltage conversion ratio of LCC resonant converter
MLT	Mean length per turn
n	Conversion turns ratio of step-up transformer
N_p	Turns of a layer
P	Average power loss in a uniform layer
P_{cs}	Losses of sereis capacitor C_s

P_{cu}	Low-frequency copper losses
P_{fe}	Core losses
P_{FB}	Losses of full-bridge inverter
P_o	Steady-state output power
P_{pri}	Primary winding copper losses
P_{SW}	MOSFET switching losses
P_{tot}	Sum of P_{fe} and P_{cu}
Q	Normalized load of LCC resonant converter
ΔQ	Delivered periodical charge of CW multiplier
R_{dc}	DC resistance of the layer
R_D	Diode on-state resistance
R_{DSon}	Drain-source on-state resistance of MOSFET
R_{ek}	Equivalent output resistance of k-stage CW multiplier
R_g	Discharge resistor
R_L	Equivalent resistance of output capacitance C_L in steady state
R_N	Negative discharge resistor
R_o	Equivalent output resistance in steady state
R_P	Positive discharge resistor
R_s	Series resistance considering the losses from full-bridge inverter and the LCC tank
t	Time
t_{fi}	Falling time during switching-off transient

t_{ru}	Rising time during switching-off transient
u_{AB}	Output voltage of full-bridge inverter
u_{cw}	Output voltage of CW multiplier
u_{cw+}	Positive CW multiplier output voltage
u_{cw-}	Negative CW multiplier output voltage
u_{in}	Input voltage
u_o	Output voltage
u_p	Voltage across over C_p, Transformer primary voltage
u_s	Voltage across series capacitor C_s
u_{sc}	1st-order Fourier coefficients of u_s
u_{ss}	1st-order Fourier coefficients of u_s
U_{cwk}	Steady-state output voltage of k-stage CW multiplier
ΔU_{cwk}	Voltage drop of k-stage CW multiplier
U_{in}	DC input voltage
U_o	Steady-state output voltage
U_{sc}	Quasi-steady-state solution of u_{sc}
U_{ss}	Quasi-steady-state solution of u_{ss}
V_F	Diode forward voltage
W_A	Core window area
Z	Impedance of LCC resonant converter
δ	Skin depth
δd	Small-signal of duty cycle

δf_s	Small-signal of switching frequency
δi_{Leff}	Error signal between reference signal and real value of effective resonant current
μ	Certainty value of membership function
λ_1	Primary volt-seconds
ρ	Wire effective resistivity
θ	Conduction angle of the CW multiplier diode
θ_{ss}	Conduction angle of the CW multiplier diode in steady state
φ	Ratio of a foil conductor layer width h to its skin depth δ'
φ_2	Phase angle between $u_{AB}(t)$ and $i_L(t)$
ω_0	Resonant frequency
ω_s	Switching frequency

GLOSSARY

AC	Alternating Current.
BJT	Bipolar Junction Transistor.
CAD	Computer Aided Design.
CAO	Computer Aided Optimization.
Converter	Consisting of inverter, LCC Tank, transformer and CW multiplier.
CPM	Current Programmed Mode.
CW	Cockcroft-Walton.
DC	Direct Current.
DUT	Device Under Test.
EDF	Extended Describing Function.
FLC	Fuzzy Logic Control.
GTO	Gate Turn-Off Thyristor.
HV	High Voltage.
IGBT	Insulated Gate Bipolar Transistor.
Inverter	Fundamental power circuitry built with high-power semiconductor switches such as power diodes, power MOSFETs and IGBTs
LCC	Series Parallel Resonant Converter.
LHP	Left Half-Plane.

LMI	Linear Matrix Inequality.
MOSFET	Metal-Oxide-Semiconductor Field-Effect Transistor.
PD	Proportional-Derivative.
PFC	Power Factor Correction.
PI	Proportional-Integral.
PID	Proportional-Integral-Derivative.
Power supply	Consisting of inverter, filter and cable.
PRC	Parallel Resonant Converter.
RHP	Right Half-Plane.
SCR	Silicon Controlled Rectifier.
SPRC	Series Parallel Resonant Converter.
SRC	Series Resonant Converter.
THD	Total Harmonic Distortion.
T-S	Takagi-Sugeno.
VLF	Very Low Frequency.
ZVS	Zero Voltage Switching.

Contents

Nomenclature **i**

1 Introduction **1**

1.1 Background, State of the Art 1

1.2 Motivation and Objectives 7

1.3 Dissertation Structure 10

2 Resonant Converter Topologies Compilation, Operation Principle and Simplification **13**

2.1 Resonant Converter Topologies Compilation 13

2.2 Operation Principle of the VLF HV Generator 15

2.3 Theoretical Analysis of Symmetrical Cockcroft-Walton (CW) Multiplier 18

2.4 LCC Resonant Converter Simplification 25

3 Modeling of the LCC Resonant Converter **27**

3.1 Introduction 27

3.2 Large-Signal Modeling of LCC Resonant Converter with a Capacitive Load 29

3.3 Steady-State Characteristics and Verification 35

3.4 Small-Signal Modeling and Verification 38

3.5 Modeling of LCC Resonant Converter with a Voltage Source Load 44

3.6 Comparison of the Small-Signal Models with a Capacitive Load or a Voltage Source Load 49

4 Model-Based Multi-Objective Optimization for LCC Resonant Converter **55**
4.1 Introduction . . . 55
4.2 Loss Modeling of LCC Resonant Converter . . . 56
4.2.1 Loss Model of Full-Bridge Inverter with MOSFETs . . . 57
4.2.2 Losses of Series Capacitor . . . 58
4.2.3 Losses of Magnetic Components . . . 59
4.2.4 Voltage Drop of Cockcroft-Walton (CW) Multiplier . . . 63
4.2.5 Multi-Objective Selection . . . 64
4.3 Optimization with Optimum f_s-d Combination and Parameters Selection . . . 66
4.3.1 Optimum f_s-d Combination . . . 66
4.3.2 Resonant Parameters Design . . . 66
4.4 Multi-Objective Optimization of LCC Resonant Converter . . . 68
4.5 Summary . . . 74

5 Conventional Linear Control Design **77**
5.1 Introduction . . . 77
5.2 Dynamics Analysis and Reduced-Order Transfer Functions . . . 78
5.3 Current Mode Linear Control Design . . . 84
5.4 Simulated Results of Linear PI Controller . . . 87
5.5 Real-Time Implementation Issues of Linear PI Controller . . . 89
5.6 Experimental Results of CPM Linear Controller . . . 91
5.7 Summary . . . 95

6 Fuzzy PD Control Design **97**
6.1 Introduction . . . 97
6.2 Conventional Fuzzy PD Controller Development . . . 98
6.3 Simulated Results of Fuzzy PD Controller . . . 106
6.4 Prototype Setup and Safety Issues of VLF HV Generator Prototype 107
6.5 Real-Time Implementation Issues of Fuzzy PD Controller . . . 110
6.6 Experimental Results of CPM Fuzzy PD Controller . . . 112
6.7 Summary . . . 114

7 Model-Based Fuzzy Control Design **115**
7.1 Introduction 115
7.2 Takagi-Sugeno (T-S) Fuzzy Model and Parallel Distributed Compensation (PDC) 116
7.3 Stability Analysis via Lyapunov Approach 119
7.4 Model Reduction of LCC Resonant Converter 119
7.5 T-S Fuzzy Control Design 125
7.6 Simulated Results of T-S Fuzzy Controller 130
7.7 Real-Time Implementation Issues and Experimental Verification . 134
7.8 Summary 137

8 Conclusion **139**

A Quasi-Steady-State Solutions **153**

B Non-zero Element in System Matrices: $\mathbf{A}_c$, $\mathbf{B}_c$, $\mathbf{C}_c$ **155**

C Parameters in the Small-Signal Circuit Model **159**

D Non-Zero Element in Normalized System Matrices: $\mathbf{A}_{cn}$, $\mathbf{B}_{cn}$, $\mathbf{C}_{cn}$ **161**

E Copper Loss Analysis Considering Eddy Current Effect **165**

F Overview of General Control Design Process **169**

G Continuous Lyapunov Equation Solutions **171**

Chapter 1

Introduction

1.1 Background, State of the Art

High voltage cables are widely used with the rapid growth of energy generation by regenerative decentralized sources and the continuous replacement of overhead power lines by underground cables for AC and DC electric power transmission. Fig. 1.1 represents the worldwide distribution of the underground high voltage power lines from year 1960 to year 2015 based on statistics and forecast, which reveals the big rise of the high voltage cable installation from year 1990, especially in Asia and America. Fig. 1.2 shows the existing, under constructing and proposed high voltage cables in Europe, most of them are built underwater.

A. Very Low Frequency (VLF) Cable Testing Technology

For such plenty of underground or submarine high voltage cables, cable testing during operation or commissioning is becoming necessary and important to ensure their fully functionality and insulation are not deteriorated due to the high voltage stress or mechanical damages.

There are various test and measurement methods to prove those buried high voltage cables are fully functional or to detect faulty ones. One of the favorite testing methods is VLF cable testing method, which uses a very low frequency (VLF) test voltage with frequencies in the range of 0.1 to 0.01 Hz. Compared with normal 50 Hz testing method, VLF cable testing method has considerable advantages in volume, weight and energy consumption; compared with DC testing

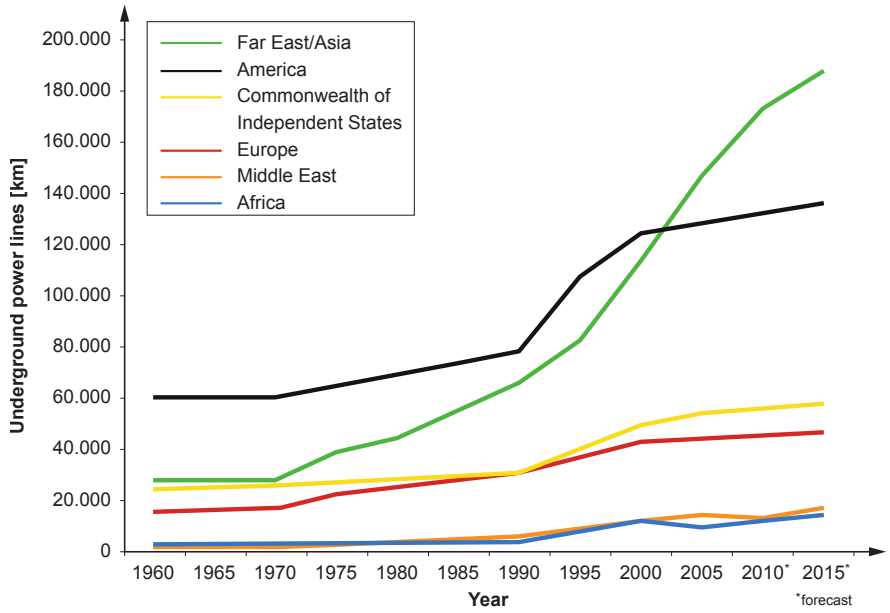

Figure 1.1: High and extra-high voltage underground power lines (beyond 50 kV) by region [GBL11]

methods, VLF testing method protects the high voltage cable from deteriorating due to the test itself. Because of those advantages, the VLF cable testing method has been adopted as standards by the European Union (EU) in 1996 [N.Nb] and by the International Electrotechnical Commission (IEC) in 2006 (IEC60060-3-2006) for high voltage cable testing.

B. Very Low Frequency (VLF) High Voltage (HV) Generator

By adopting VLF cable testing technology, it is feasible to develop mobile VLF HV generator in a usual van within a short set up time. Those VLF HV generators are capable of generating a true-sinus test voltage of 0.1 to 0.01 Hz or with other user-defined waveforms at some tens to hundreds kV. The required power is in the range of a few to some tens kW. Fig. 1.3 presents an illustration of a mobile VLF HV generator.

Historically there are many concepts for developing VLF HV generators, main of them are summarized as below:

1. Modulated amplitude high voltage generator with motorized variable trans-

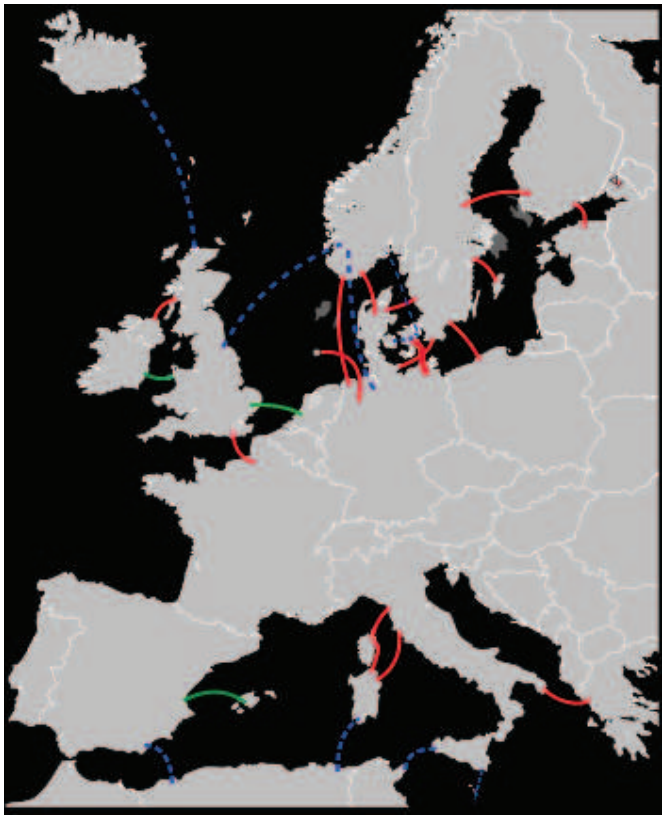

Figure 1.2: Distribution of high voltage power links in Europe refer to [Je08][Sie08][Gan07]. Red: existing links; green: under construction; blue: proposed

former [SKSC08][Rei]: Fig. 1.4 represents the operating principle of a modulated amplitude high voltage generator with a motorized variable transformer. By means of a variable transformer in automatic mode with a motor, the voltage amplitude of a downstream conventional high voltage transformer can be modulated from zero to maximal value with specified operating frequency. Combined with the control of the downstream demodulator and high voltage switches operation in corresponding time points, the polarity of the output voltage can be switched and results in an expected sinusoidal VLF high voltage. Such VLF high voltage generator has simple structure and operation principle, but the robustness of the demodulator and the realization of the polarity switch are a great challenge. The other critical disadvantage of this circuit is the motorized variable trans-

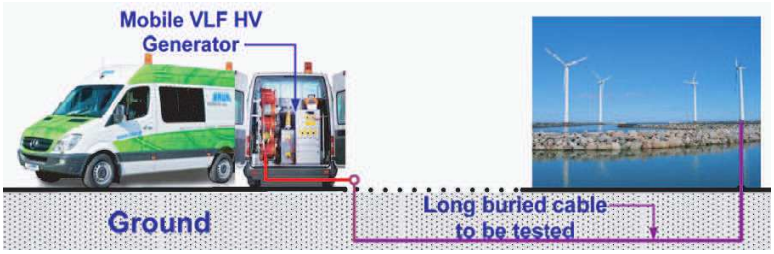

Figure 1.3: Illustration of underground high voltage cable testing by a mobile VLF HV generator

former, which is an obvious limitation for high power application with high or highest voltage.

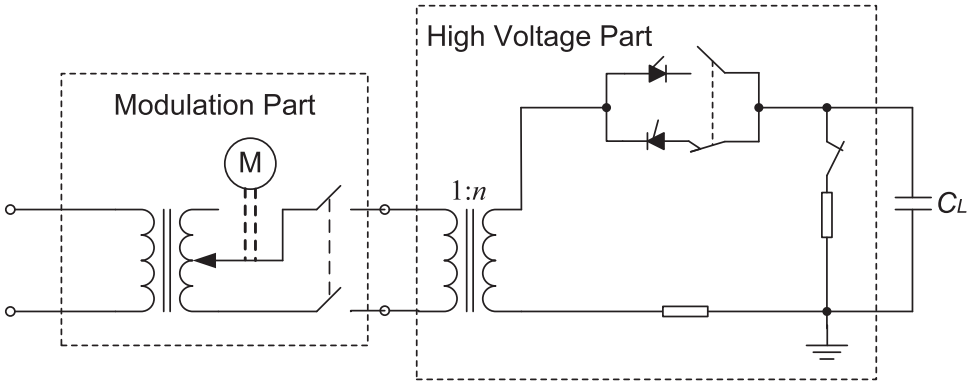

Figure 1.4: Modulated amplitude high voltage generator

2. High voltage generator with series resonant systems [JPGT] [N.Na]. As shown in Fig. 1.5, the voltage regulator provides an adjustable voltage to the exciter transformer, the exciter transformer excites the resonant circuit, which consists of the variable HV reactor L_R and the load capacitance C_L. C_L consists mainly of the capacitance of the device under test (DUT), but includes also the stray capacitance of the circuit, the capacitance of the HV divider and possibly a preload capacitor. R_L represents the losses in the HV reactor L_R. The inductance of the HV reactor L_R can be varied by adjusting the air gap in the core, it should be adjusted in such a way that its impedance is equal to the impedance of the load capacitance C_L

at power frequency to let the system in resonant condition. This high voltage generator has very simple structure and principle, has no additional demodulator and polarity switches. But it is difficult to generate VLF high voltage via such structure due to possible tremendous HV Reactor L_R. Another disadvantage of this circuit is similar as the aforementioned limitation of the variable transformer.

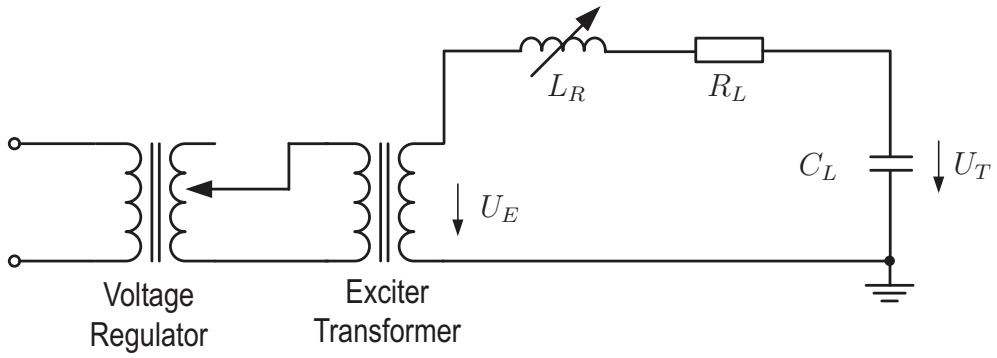

Figure 1.5: Series resonant system for generating high test voltage

3. Mohaupt derived an idea for generating VLF high voltage based on beat frequency principle [Moh08]. As shown in Fig. 1.6, based on two exciters, resonant circuit consisting of inductance and capacitance is forced to oscillate with corresponding frequency, respectively. The difference between both frequencies is two times as the expected VLF output voltage frequency, such as 1000 Hz and 1000.2 Hz for expected 0.1 Hz output voltage. Through absorbing the ideas from aforementioned high voltage generator with modulated amplitude and that with resonant systems, Mohaupt added the beat frequency principle in this structure. This new structure has no required mechanical components and it is also realizable for high power application over 100 kW. But similar as the motorized modulated amplitude high voltage generator, it is always a great challenge to implement the robust demodulator and the polarity switch.

4. Regulated power module with controllable discharge [uMG07]: Different from above, Fig. 1.7 provides another structure of VLF high voltage generator with positive part and negative part. Each part consists of a regulated

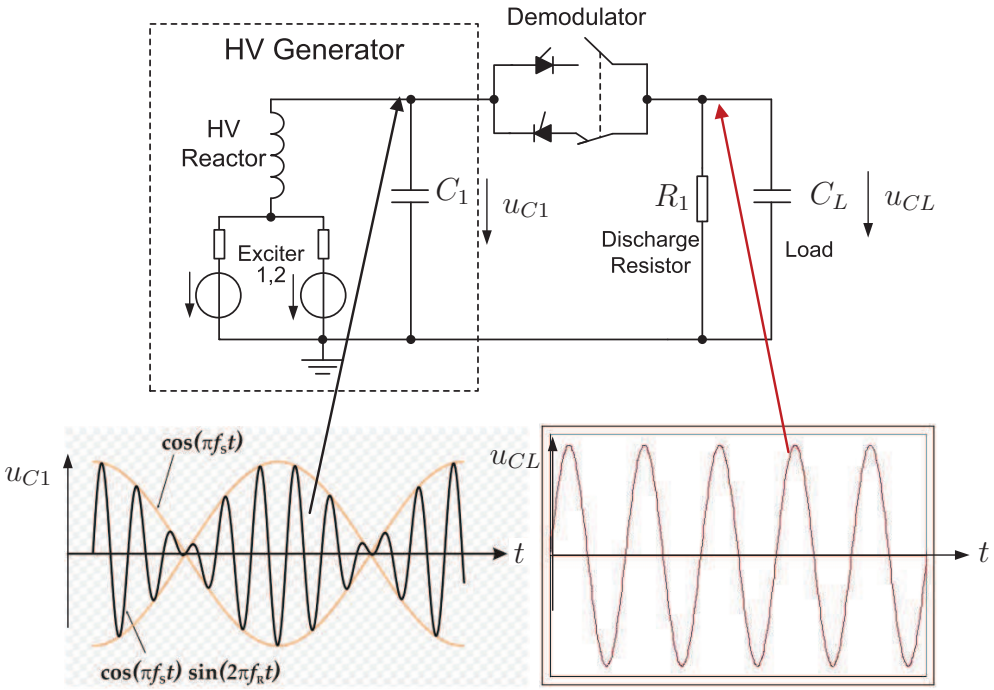

Figure 1.6: High voltage generator with beat frequency principle

power module, resonant tank, high voltage transformer, Cockcroft-Walton (CW) multiplier and controllable discharge. Among which, positive part is responsible to generate the positive VLF sinusoidal output voltage, while negative part is in charge of generating the negative part of the VLF sinusoidal output voltage. As shown in Fig. 1.7, this circuit has no motorized mechanical components, it needs no additional demodulation or high voltage switches. The DC input voltage U_{in} can be easily obtained from grid via usual AC-DC converter. By means of controllable switching frequency, duty cycle and discharge, the output VLF high voltage can be generated and its amplitude can be regulated in an expected wide region. Especially, such structure is advantageous for small portable VLF high voltage generator due to possible small dimension and weight with higher switching frequency. Disadvantage of this structure may result from the costly CW multiplier and discharge circuit, and the complexity of system control.

Based on above study and investigation of the existing VLF high voltage gen-

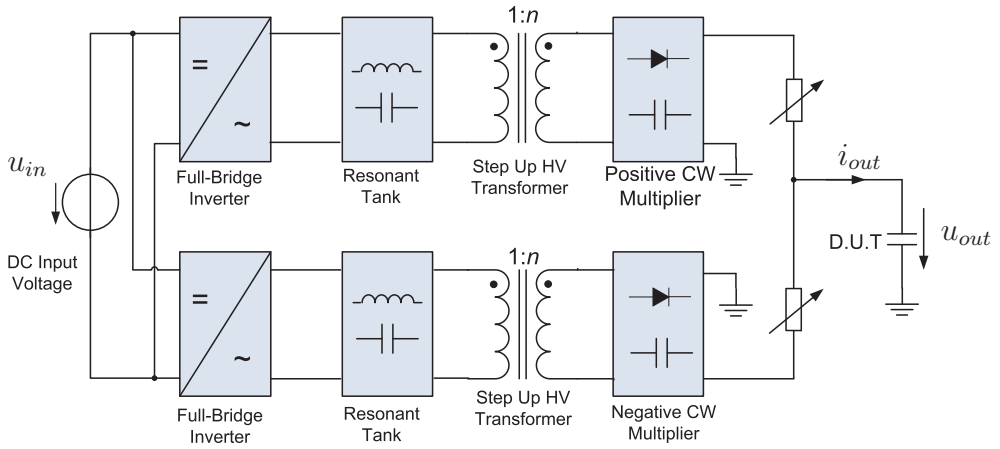

Figure 1.7: High voltage generator with regulated power module, resonant tank, HV-transformer, CW multiplier and controllable discharge

erator concepts, the last solution is thought to be a preferable one due to its feasibility with common electrical components and circuits, due to its control flexibility with modulated switching frequency and duty cycle, and also due to the possible extendibility of the VLF high voltage generator with various output voltages.

1.2 Motivation and Objectives

A. Motivation

With fast development in the field of power electronics and more requirements for VLF high voltage test system, the industries have stringent demands to understand system steady-state and dynamic behavior, to improve system efficiency and control performance, to implement computer aided design and optimization. Contrary to those, the limited availability of novel large-signal model and small-signal model, the lack of multi-objective optimization research, and the absence of modern nonlinear control strategy study, become the theoretical bottleneck. This incompatibility between industry and research restricts the development.

As a summary, the motivation can be described as the following aspects:

1. VLF high voltage generator has wide operating region regarding output voltage, output load and power. Investigations show that with separate

frequency or duty cycle control cannot meet system design specifications, both of them should be combined. Such control scheme was not realized in present VLF high voltage generator due to its complexity and novelty. Actually it is not so easy, since the precondition is that the system dynamic performance regarding switching frequency and duty cycle should be explicit; and the combined control regarding both control variables should be compatible and would not result in system instability.

2. Symmetrical Cockcroft-Walton (CW) multiplier circuit is thought to be more appropriate in high voltage application, but its detailed steady-state and dynamic characteristics are still not so clear; many problems are expected to be solved, such as: is it possible to precisely predict the voltage drop in the symmetrical CW multiplier; how to use CW multiplier more efficiently; is it feasible to replace a more-stage CW multiplier with a one-stage CW multiplier in modeling.

3. Nowadays, the increase of power conversion efficiency and reduction of the costs are gaining higher and higher concern. A demand with properly VLF high voltage generator design considering electrical component stress, power losses, conversion efficiency, weight, volume, cost, is undoubtedly more urgent from industry.

4. Besides the output voltage, the resonant current in resonant tank is also an important intermediate quantity in VLF high voltage generator, which has higher dynamics and determines the performance of other electrical quantities. Existing conventional linear control scheme has poor control performance regarding the higher dynamic, especially for some extra customer demands, such as user-defined pulsing form or DC form output voltage waveforms. The research about the modern nonlinear control methods or techniques besides the traditional one is necessary and inevitable.

Based on above motivation, European Commission financed the Seventh Framework Program - Theme 7: RPC-HVTS-DCS, in order to support and promote the small and medium enterprises, which dedicates to improve industrial capability for new products creation, cost reduction, quality improvement and market share

expansion.

B. Objectives

According to above motivations, this dissertation has the following objectives:

1. The most appropriate resonant topology for VLF high voltage generator application should be determined with consideration of the steady-state and dynamic characteristics, controllability, feasibility and extendibility.

2. Large-signal modeling and small-signal modeling of the selected resonant converter system should be implemented for the nonlinear VLF high voltage generator, since they are of important theoretical significance for system dynamic analysis, model-based optimization and model-based control design.

3. Loss modeling should be carried out in order to describe the real system more precisely. The power losses from resistive components, magnetic components, switching losses, and the voltage drop in CW multiplier should be considered.

4. The steady-state and dynamic characteristics of a symmetrical CW multiplier circuit should be researched. The feasibility of the replacement of a more-stage CW multiplier with corresponding one-stage CW multiplier in modeling should be investigated.

5. A multi-objective design and optimization for the VLF high voltage system should be implemented to provide design and optimization guideline for industry.

6. The conventional linear and modern nonlinear control schemes for VLF high voltage test system should be researched and compared, in order to solve the existing control problems and further improve system control performance.

1.3 Dissertation Structure

The dissertation is organized and divided into following sections:

1. At first, based on the state-of-the-art of VLF high voltage generator concepts, a preferable resonant circuit is confirmed in Chapter 2. The operating principle of the resonant converter applied in the VLF high voltage generator is then described. As an important part of the resonant converter, CW multiplier circuit is analyzed regarding its steady-state and dynamic characteristics for more-stage and one-stage, respectively. Based on such analysis, a simplification of the original resonant converter with more-stage CW multiplier circuit is implemented.

2. In Chapter 3, the detailed process of the large-signal modeling and small-signal modeling of the resonant converter with a capacitive load is represented. The experimental verification of the derived large-signal model and small-signal model are provided. As an additional study, the large-signal modeling and small-signal modeling of the resonant converter with an equivalent voltage source load is further derived in Chapter 3. The comparison between them is also implemented.

3. Loss modeling of the resonant converter is described in Chapter 4, which considers not only the usual resistive power losses, but also the losses of magnetic components and voltage drop from CW multiplier. Further, a model-based multi-objective optimization of the resonant converter with Pareto front is represented.

4. Based on the derived small-signal model, Chapter 5 develops the traditional CPM linear controller for VLF high voltage generator. A scaled-down prototype and a real VLF HV generator are represented. The experimental results are provided for the validation.

5. As an alternative of the linear PI controller, an investigation of a model-free CPM fuzzy PD controller is investigated in Chapter 6. A scaled-down labratory prototype is introduced. The simulated and experimental results are provided for the verification and validation.

6. In order to find a more appropriate control scheme, a model-based Takagi-Sugeno fuzzy controller is further developed in Chapter 7. The simulated results are represented for the verification. Based on the scaled-down labratory prototype, the experimental results are also provided for the validation.

7. Conclusions are finally stated in Chapter 8.

Chapter 2

Resonant Converter Topologies Compilation, Operation Principle and Simplification

2.1 Resonant Converter Topologies Compilation

In Chapter 1, the circuit demonstrated in Fig. 1.7 is thought to be the preferable structure for VLF HV generator.

From literatures [Ste88][MRDP+07][YLJ92], it can be concluded that resonant converters are a very attractive solution in high voltage high power applications due to the voltage conversion characterisitcs, the quasi-sinusoidal voltage and/or current waveforms, and the soft-switching features.

Among all the resonant topologies, the series resonant converters (SRCs) are commonly adopted in industry [RS98] due to the following advantages: inherent short circuit protection, zero-voltage commutations, limited harmonics in the resonant current, maximum power transfer at minimum switching frequency, transformer leakage inductance included in the resonant link. But their limitations cannot be neglected: they do not cope with the transformer stray capacitance; for reduced load current, they lose the soft commutation advantage, and the output voltage cannot be controlled any more.

In contrast to the SRCs, the parallel resonant converters (PRCs) appear to be a better choice, since they can include the stray capacitance and the leakage inductance of HV-transformer into the resonant net; they can also control the

output voltage at no load case. However, PRCs are difficult to control if the load and input voltage vary widely; moreover, the circulating current of PRCs are independent of load [MRDP+07].

The series parallel resonant converters (SPRCs) are also called LCCs, since they are comprised of a series inductor, a series capacitor and a parallel capacitor. Such converters take advantage of the best characteristics of the SRCs and the PRCs, while eliminating their weak points. The LCC resonant converter shows a number of more desirable features, which are capable of operating with wide output voltage, power and load ranges. It has the natural commutation for BJT, GTO and SCR devices at sub-resonant operation mode or zero-voltage switching (ZVS) for MOSFETs at over-resonant operation mode. A properly designed LCC resonant converter can make even use of the parasitics of HV-transformer and the balancing capacitors of rectifier diodes, which result in smaller tank size of series inductor L_s and parallel capacitor C_p. A number of high power high voltage applications adopting LCC resonant converter demonstrate its praticability and effectiveness in this field [MRDP+07][HFB09b][FJ05].

The LLCC resonant converter, which can be regarded as a LCC resonant converter combined with the inherent magnetizing inductance of the HV-transformer, is also considered for the VLF HV application. Due to the newly introduced parallel inductor L_p, it has the potential to realize the local reactive power compensation. But investigations show that the steady-state characteristics of the LLCC resonant converter are similar as those of the LCC resonant converter in the expected operation region; the attractive advantage of the local reactive power compensation capability cannot be effectively utilized for the given application, since it can only be realized in a selected narrow frequency region, but the VLF high voltage generator has a wide operation region and needs a wide frequency and duty cycle modulation range.

Based on above discussion, the LCC resonant converter is selected as the appropriate topology for the VLF HV generator application.

2.2 Operation Principle of the VLF HV Generator

The circuit diagram of a VLF HV generator with integrated LCC resonant inverter is represented in Fig. 2.1, which consists of similar positive and negative parts, each part comprises of input DC source, full-bridge inverter, LCC tank, step-up HV-transformer, more-stage symmetrical CW multiplier, adjustable discharge resistors and a capacitive output load [CHFB10].

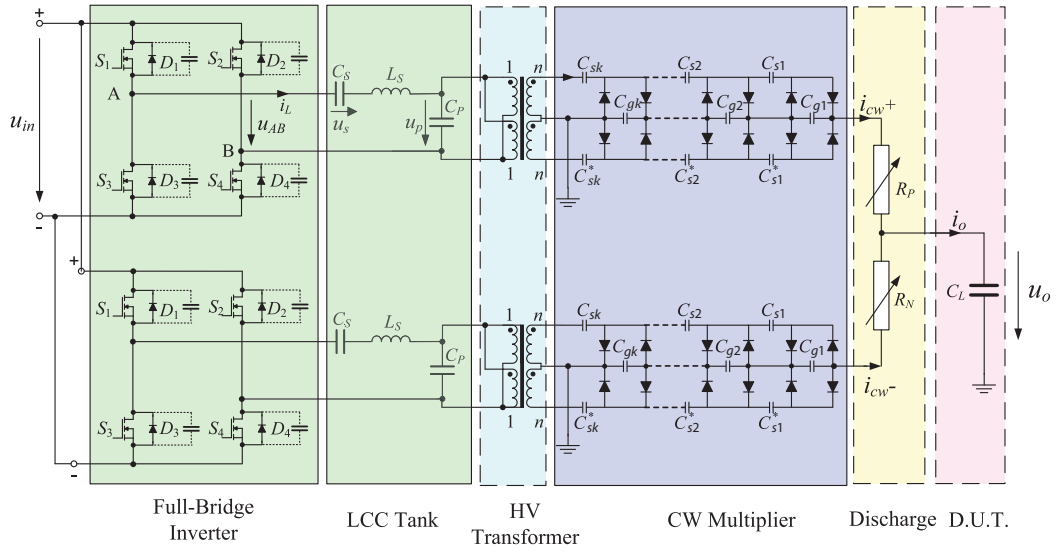

Figure 2.1: VLF HV generator consists of LCC resonant inverter, HV-transformer, symmetrical k-stage CW multiplier and controllable discharge

Depending on various VLF HV generator, the magnitude of the input voltage u_{in} can be regulated by front end PFC circuit and has the maximal value about 560 V. Full-bridge inverter consisting of MOSFETs or IGBTs generates u_{AB}, which has a square waveform with changeable duty cycle d and switching frequency f_s, the natural ZVS soft switching feature can be obtained since the LCC tank operates in over-resonant region. The LCC tank shapes the expected quasi-sinusoidal voltage u_p and resonant current i_L with preferable conversion ratio. HV-transformer is used for voltage enhancement, and the CW multiplier circuit is adopted for further voltage enhancement and rectification. Discharge

resistors R_P and R_N are adopted for output voltage discharge in order to get the expected sinusoidal waveform.

The operation principle of the VLF HV generator with 0.1 Hz sinusoidal output voltage is described below. Since the similar circuit structure and operation principle of positive part and negative part, also due to the sinusoidal output voltage waveform, only the positive part in the half-period interval from 0 to 5 seconds is represented in detail [CHFB10][uMG07].

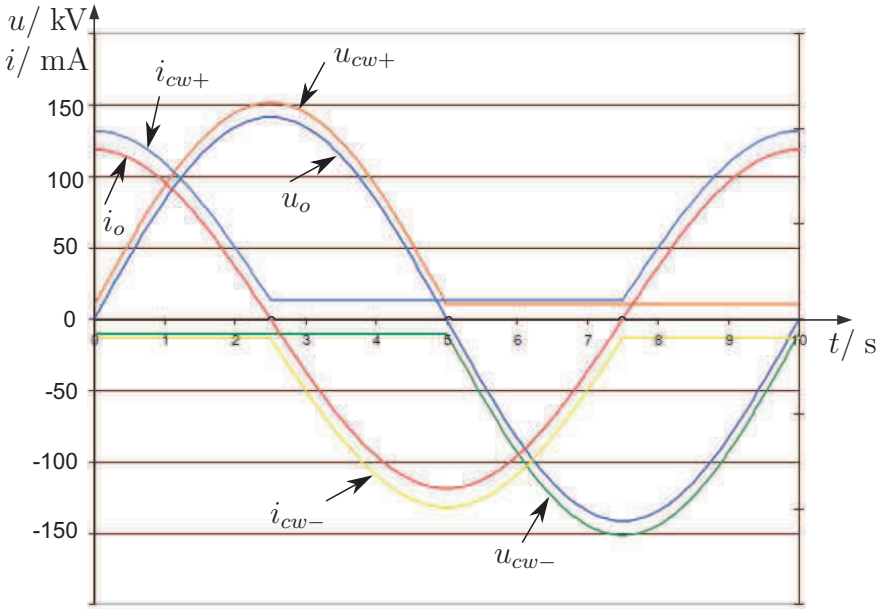

Figure 2.2: VLF HV generator output voltage and output current waveforms with ideal pure output capacitor

1. Referring to Fig. 2.2, during time interval $t = 0 \sim 2.5$ s, the positive LCC resonant converter is activated and both discharge resistors R_P and R_N are kept constant. The positive CW multiplier output voltage u_{cw+} can be regulated from zero to the positive peak value of the VLF sinusoidal voltage by duty cycle d and switching frequency f_s modulation. The output voltage u_o is derived from u_{cw+} and a constant voltage drop on R_P. The current i_{cw-} through R_N is kept at a small constant value. Fig. 2.3(a) shows the

voltage and current of C_L, R_P and R_N in this interval, among which, the red arrows represent the real current flow direction.

2. Referring to Fig. 2.2, during time interval $t = 2.5 \sim 5.0$ s, both LCC resonant converters are deactivated. The output voltage u_o is discharging through the controllable variable negative discharge resistor R_N for expected sinusoidal waveform. The current i_{cw+} through R_P kept at a small constant value. Fig. 2.3(b) shows the voltage and current of C_L, R_P and R_N in this interval, among which, the blue arrows represent the real current flow direction.

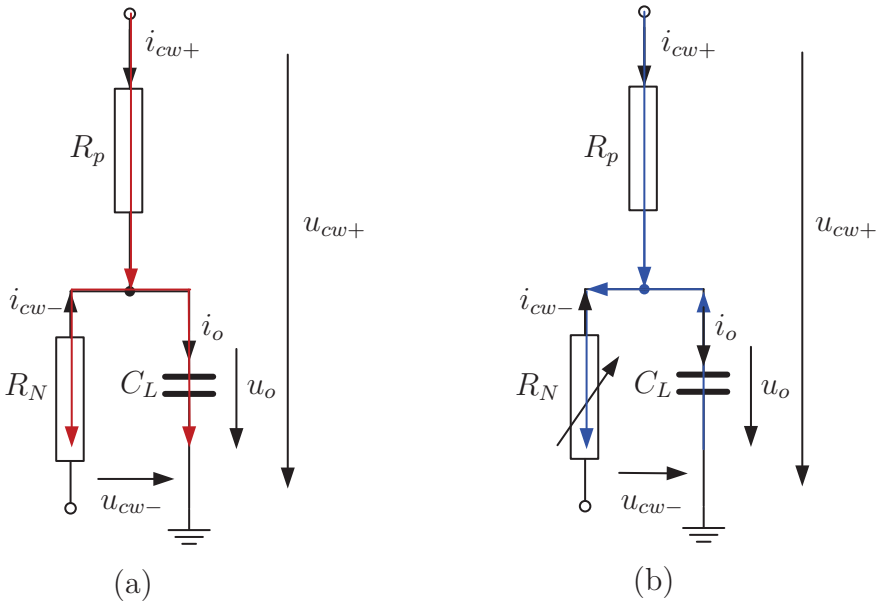

Figure 2.3: Output voltage and output current of R_P, R_N, C_L in the first half-period

For the negative part of the sinusoidal output voltage u_o, the negative LCC resonant converter and the positive discharge resistor R_P will be sequentially activated for the charge and discharge process, respectively. Since the operation principle is similar as that of the positive part, it is not repeated.

2.3 Theoretical Analysis of Symmetrical Cockcroft-Walton (CW) Multiplier

Cockcroft-Walton multiplier circuits have been widely used in many high voltage low current industrial applications [OPS01] [Bal59]. This circuit was first invented by Heinrich Greinacher in 1913 [Gre14]. It is later also called a Cockcroft-Walton (CW) multiplier after the particle accelerator machine built by John Cockcroft and Ernest Walton [DK01]. In order to deal with a wide range output voltage of VLF high voltage generator, a combination of a high voltage transformer and a CW multiplier is thought to be a preferable choice. The adoption of a CW multiplier can obviously reduce the size and losses of the high voltage transformer. Investigations show that the losses and size of the multiplier circuits do not exceed the savings made on the transformer, if the multiplier is limited to 3-5 stages [OPS01]. Theoretical modeling and performance analysis of an asymmetrical CW multiplier were implemented in literatures [Bal59][BWM92][Bru71][LMR94].

In this subsection, theoretical analysis and the results are briefly represented for a symmetrical more-stage and corresponding one-stage CW multiplier.

A. Theoretical Performance Analysis

Based on [Bal59], a detailed investigation about the steady-state characteristics of a k-stage symmetrical CW multiplier was executed, which considers not only the voltage drop from capacitors' charge and discharge, but also the resistive losses from transformer and diodes. Further, the diodes reverse recovery losses are also considered based on a simulated investigation. From those research results, it can be concluded that the effect from capacitors' charge and discharge is the most important factor, which determines the steady-state performance of the CW multiplier. Compared with those, the other factors occupy only a small part of the total losses, and would be neglected in the later discussion.

A k-stage symmetrical CW multiplier circuit is represented in Fig. 2.4 for the theoretical performance analysis. The following assumptions are thought to be true:

1. The output capacitive load C_o is sufficiently large that the output voltage U_{cwk} is essentially DC.

2. The diodes are ideal.

3. The input AC source swings u_{ts} regarding the ground can be depicted as: $u_{ts} = U_{ts}\cos(2\pi f_s t)$ with frequency f_s, and is of sufficiently low impedance for all RC time constants to be negligible.

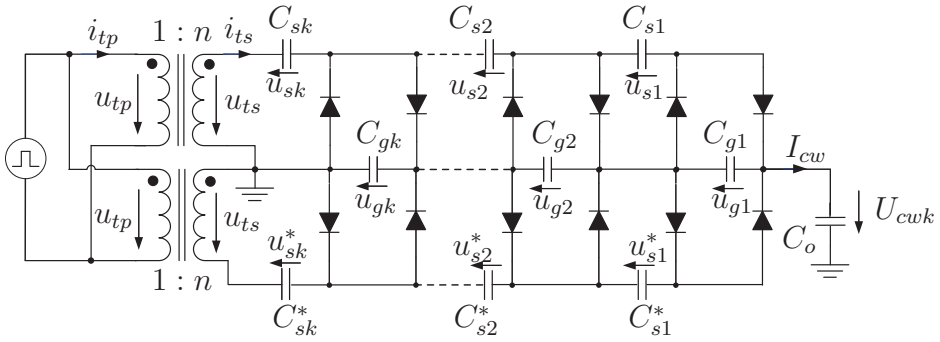

Figure 2.4: K-stage symmetrical CW multiplier with impedance load

Period	Charge Direction
0-	$U_{ts} \overset{\Delta Q/2}{\rightarrow} C_{sk}$, $U_{ts} \overset{\Delta Q/2}{\rightarrow} C^*_{sk}$
1+	$C_{sk} \overset{\Delta Q/2}{\rightarrow} C_{gk}$, $C^*_{sk} \overset{\Delta Q/2}{\rightarrow} C_{gk}$
1-	$C_{gk} \overset{\Delta Q}{\rightarrow} C_{s(k-1)}$, $C_{gk} \overset{\Delta Q}{\rightarrow} C^*_{s(k-1)}$
$\vdots$	$\vdots$
$(k-1)+$	$C_{s2} \overset{\Delta Q}{\rightarrow} C_{g2}$, $C^*_{s2} \overset{\Delta Q}{\rightarrow} C_{g2}$
$(k-1)$-	$C_{g2} \overset{\Delta Q}{\rightarrow} C_{s1}$, $C_{g2} \overset{2\Delta Q}{\rightarrow} C^*_{s1}$
$k+$	$C_{s1} \overset{\Delta Q/2}{\rightarrow} C_{g1}$, $C^*_{s1} \overset{\Delta Q/2}{\rightarrow} C_{g1}$
k-	$C_{g1} \overset{\Delta Q}{\rightarrow} C_o$

Table 2.1: Periodical charge (ΔQ) delivery consequence in k-stage symmetrical CW multiplier

In order to analyze the charge process for each capacitor, it requires a coupling handle through each diode for periodical charge ΔQ. The k-stage symmetrical CW multiplier is decomposed as two parts: one is the equivalent circuit during the

negative swing period of u_{ts}, the other is the equivalent circuit during the positive swing period of u_{ts}, as shown in Fig. 2.5(a) and Fig. 2.5(b), respectively. The characteristics of the symmetrical CW multiplier can be derived by alternatively considering Fig. 2.5(a) and Fig. 2.5(b). Table 2.1 lists the corresponding charge delivery sequence during i- period and i+ period ($i = 1, 2, \ldots, k$).

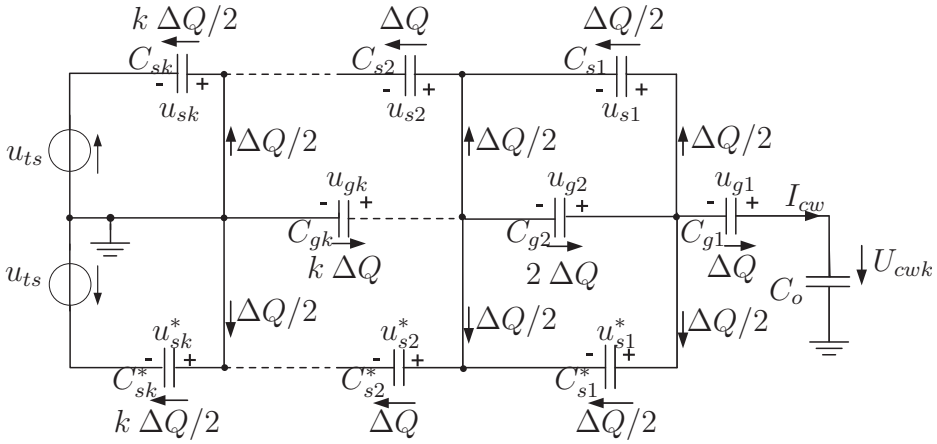

(a) During u_{ts} negative swing (i-) period: $i \cdot T_s \leq t \leq i \cdot T_s + D \cdot T_s$, $i \in N$

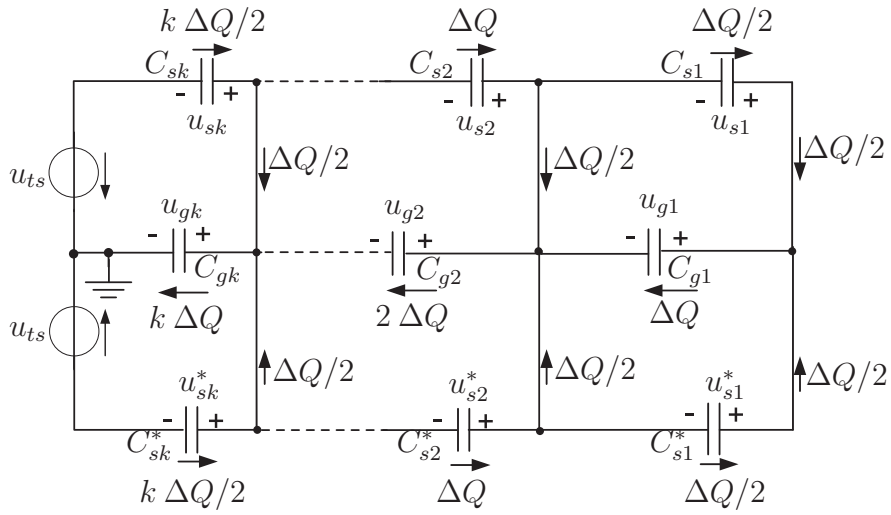

(b) During u_{ts} positive swing (i+) period:$i \cdot T_s + D \cdot T_s \leq t \leq (i+1) \cdot T_s$, $i \in N$

Figure 2.5: Equivalent circuit of a k-stage symmetrical CW multiplier

The output voltage of k-stage symmetrical CW multiplier U_{cwk} can be derived through summing each capacitor's voltage in smoothing route during i- period

$(i = 1, 2, \ldots, k)$ [Bru71][LMR94]:

$$\begin{aligned} U_{cwk} &= U_{gk} + U_{g(k-1)} + \ldots + U_{g1} \\ &= 2kU_{ts} - \frac{k^2\Delta Q}{2C_{sk}} - \frac{k^2\Delta Q}{C_{gk}} - \frac{(k-1)^2\Delta Q}{2C_{s(k-1)}} - \frac{(k-1)^2\Delta Q}{C_{g(k-1)}} - \ldots - \frac{\Delta Q}{2C_{s1}} - \frac{\Delta Q}{C_{g1}} \end{aligned} \tag{2.1}$$

Since the periodical delivered charge ΔQ equals the output current I_{cw} divides the frequency f_s:

$$\Delta Q = I_{cw}/f_s \tag{2.2}$$

The general output voltage U_{cwk} in Eq. 2.1 can be rewritten as:

$$U_{cwk} = 2kU_{ts} - \left(\frac{k^2}{2C_{sk}} + \frac{k^2}{C_{gk}} + \frac{(k-1)^2}{2C_{s(k-1)}} + \frac{(k-1)^2}{C_{g(k-1)}} + \ldots + \frac{1}{2C_{s1}} + \frac{1}{C_{g1}}\right)\frac{I_{cw}}{f_s} \tag{2.3}$$

From Eq. 2.3, conclusions can be drawn that the output characteristics of the symmetrical k-stage CW multiplier are determined by the multiplier stage k, the frequency f_s and the capacitor values. If the output current I_{cw} is zero, the full multiplication is obtained. Otherwise, the voltage decreases linearly with increasing I_{cw} and decreases exponentially with increasing k. An equivalent output resistance R_{ek} is adopted to describe the voltage drop ΔU_{cwk}:

$$R_{ek} = \left(\frac{k^2}{2C_{sk}} + \frac{k^2}{C_{gk}} + \frac{(k-1)^2}{2C_{s(k-1)}} + \frac{(k-1)^2}{C_{g(k-1)}} + \ldots + \frac{1}{2C_{s1}} + \frac{1}{C_{g1}}\right)\frac{1}{f_s} \tag{2.4}$$

If the total capacitance is constrained, a minimal R_{ek} can be obtained by use of unequal capacitors [Bru71], but since the minimal R_{ek} is not less than 75 percent of the resistance with equal capacitors, same capacitors are usually adopted for a simplified analysis.

If all the capacitors in a symmetrical CW multiplier are of same value C, the output voltage U_{cwk} in Eq. 2.3 can be further approximated:

$$U_{cwk} \approx 2kU_{ts} - \left(\frac{k^3}{2} + \frac{3k^2}{4} - \frac{k}{16}\right)\frac{I_{cw}}{Cf_s} \tag{2.5}$$

The corresponding voltage drop ΔU_{cwk} of a symmetrical k-stage CW multiplier with same capacitors is:

$$\Delta U_{cwk} = \left(\frac{k^3}{2} + \frac{3k^2}{4} - \frac{k}{16}\right)\frac{I_{cw}}{Cf_s} \tag{2.6}$$

The equivalent output resistance R_{ek} of a symmetrical k-stage CW multiplier with same capacitors can be represented as below.

$$R_{ek} = \left(\frac{k^3}{2} + \frac{3k^2}{4} - \frac{k}{16}\right)\frac{1}{Cf_s} \tag{2.7}$$

Based on above analysis, the theoretical performance of the symmetrical more-stage and one-stage CW multiplier are concluded and compared.

1. If $I_{cw} = 0$, then $\Delta U_{cwk} = 0$. The output voltage of k-stage CW multiplier U_{cwk} is simple k-times of that of the one-stage CW multiplier U_{cw1}.

$$U_{cwk} = kU_{cw1} \tag{2.8}$$

2. If $I_{cw} \neq 0$, since the equivalent resistance R_{ek} of k-stage CW multiplier is much larger than k-times of R_{e1} of the one-stage CW multiplier, the resulting voltage drop ΔU_{cwk} in k-stage CW multiplier is correspondingly much larger than k-times of ΔU_{cw1} in one-stage CW multiplier. U_{cwk} and U_{cw1} is not a simple k-time proportional relationship again, an additional voltage drop due to the increased output resistance should be considered:

$$U_{cwk} = kU_{cw1} - I_{cw}\left(R_{ek} - R_{e1}\right) \tag{2.9}$$

From above equations and analysis, it can be concluded that the symmetrical k-stage CW multiplier can be approximated as k-times of those of one-stage CW multiplier with consideration of the predictable increasing voltage drop.

B. Dynamic Characteristics

Dynamic characteristics of the symmetrical more-stage and the corresponding one-stage CW multiplier are analyzed and compared based on the following simulated results.

Fig. 2.6 shows a simulated circuit diagram of a LCC resonant converter with three-stage or one-stage symmetrical CW multiplier. For both CW multipliers, the input voltage and input current are the same, and the operating points with the same output power are selected for the analysis. For each CW multiplier

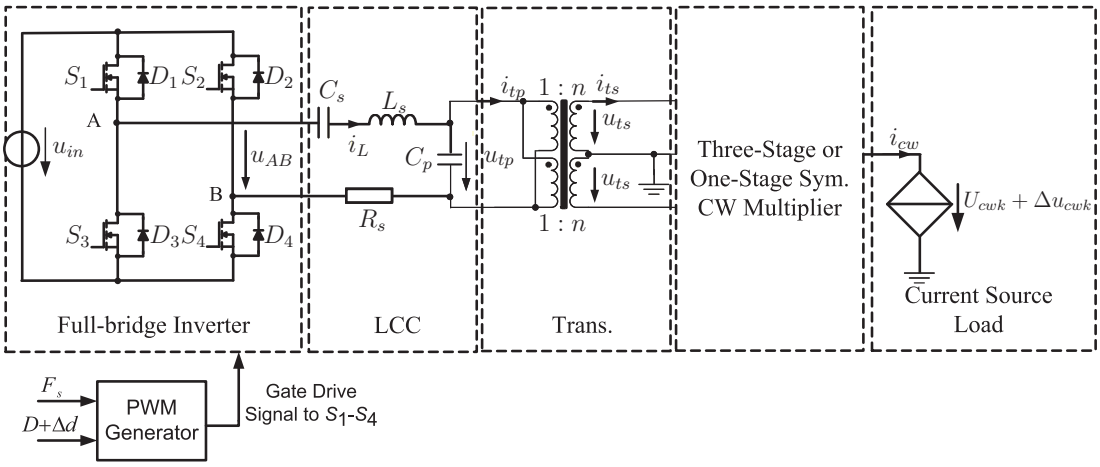

Figure 2.6: Simulated circuit diagram for CW multiplier dynamic characteristics analysis

analysis, the output current i_{cw} is kept as a small constant. Due to the different capacitors' voltage stress in both CW multipliers, their capacitances are accommodated: the capacitance in one-stage CW multiplier is three-times of their counterpart in three-stage CW multiplier.

Since the front-end circuit for both CW multiplier is the same, it is reasonable to directly analyze the dynamic characteristics of the control-to-output-voltage transfer function. In the simulated circuit, the dynamics of duty-cycle-to-normalized-output-voltage transfer function are investigated: a specified PWM driving signal with constant switching frequency F_s, constant duty cycle D plus a deviation Δd is generated and transferred to the full-bridge inverter, through LCC tank, HV-transformer, the resulting quasi-sinusoidal input voltage u_{ts} with the corresponding small signal amplitude variation is provided to the three-stage or one-stage CW multiplier, an output voltage u_{cwk} from each CW multiplier circuit with corresponding small signal amplitude variation Δu_{cwk} can then be obtained. The formulating forms of d and u_{cwk} are represented in Eq. 2.10 and Eq. 2.11, respectively.

$$d = D + \Delta d \cos(2\pi f_m t) \tag{2.10}$$

$$u_{cwk} = U_{cwk} + \Delta u_{cwk} \cos(2\pi f_m t + \varphi) \tag{2.11}$$

The normalized voltages are defined as follows. Among which, U_{in} is the magnitude of the steady-state input voltage.

$$u_{cwkn} = u_{cwk}/U_{in} \tag{2.12}$$

$$\Delta u_{cwkn} = \Delta u_{cwk}/U_{in} \tag{2.13}$$

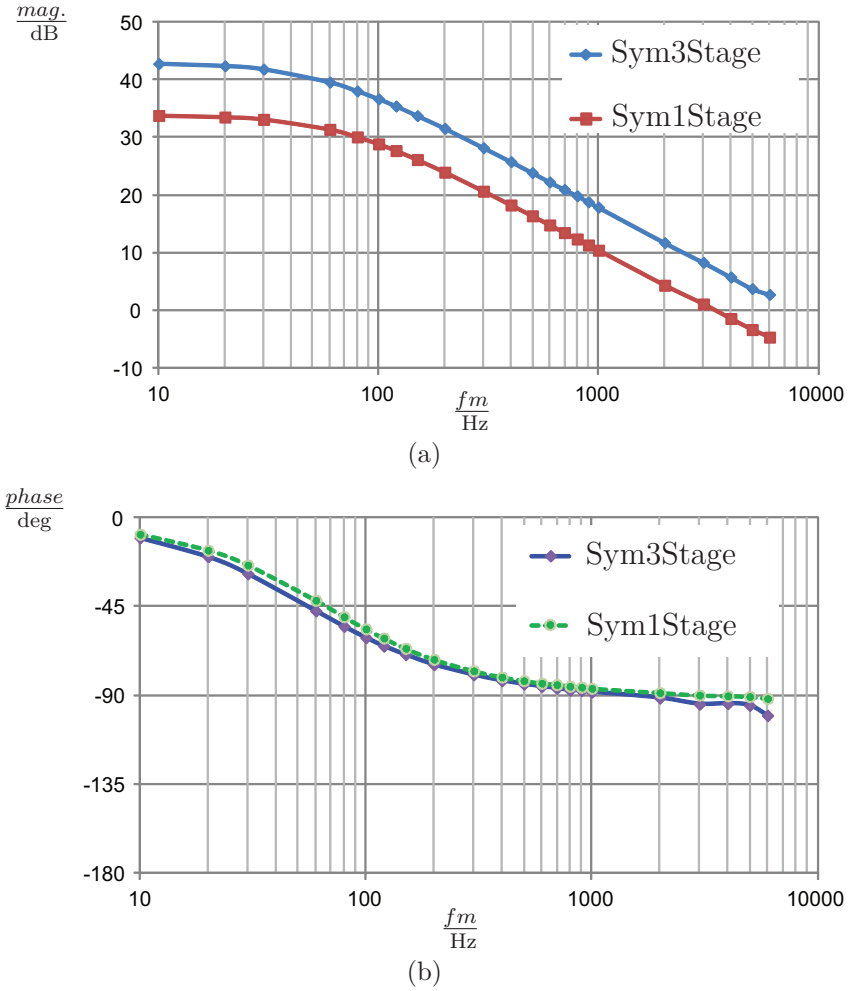

Figure 2.7: Bode diagram of three-stage and one-stage symmetrical CW multiplier based on simulated Δd-to-Δu_{cwkn} dynamic characteristics analysis

Based on the simulated results, the dynamic characteristics of Δd-to-Δu_{cwkn} for both symmetrical CW multipliers can be obtained. In latter dynamic characteristics or transfer functions representations, the small signal symbol "Δ" is omitted for simplification. Their Bode diagrams are provided in Fig. 2.7(a) and

Fig. 2.7(b). Among which, Fig. 2.7(a) represents the magnitude Bode diagrams of the three-stage and one-stage CW multiplier, both of the diagrams have nearly the same crossover frequency, their magnitude difference is almost the same in the complete studied frequency range, which is due to the steady-state characteristics difference resulting from the different stage number and is about: $20\log\frac{3}{1}_{10} = 9.54dB$; Fig. 2.7(b) shows the phase Bode diagrams of the three-stage and one-stage CW multiplier, both agree well in the studied range besides a little deviation.

Based on above comparisons, it can be concluded that the dynamic characteristics of the symmetrical more-stage CW multiplier are similar as those of the corresponding one-stage CW multiplier under the specified conditions.

Considering both the steady-state and dynamic aspects, it can be said that under the specified conditions, the replacement of the symmetrical k-stage CW multiplier by the corresponding one-stage CW multiplier is feasible.

2.4 LCC Resonant Converter Simplification

In order to effectively understand the operation behavior of the complex system represented in Fig. 2.1 by mathematical means, it is necessary to make some simplifications and assumptions.

Referring to Section 2.2, the studied VLF high voltage generator adopts similar positive and negative LCC resonant converters, both of them have the similar circuit structure and similar operation principle. Such reality let it possible to investigate only the positive part LCC resonant converter in the next Chapters.

Based on the analysis of CW multipliers' steady-state and dynamic characteristics, it can be seen that with approximations and under some specified conditions, the replacement of a symmetrical more-stage CW multiplier with the corresponding one-stage CW multiplier for later modeling is acceptable.

Moreover, assuming the HV-transformer is an ideal component. Since the ideal transformer satisfies the following voltage and current conversion principles between primary side and secondary side: $u_{ts}/u_{tp} = n$, $i_{tp}/i_{ts} = n$, $u_{ts} * i_{ts} = u_{tp} * i_{tp}$, the step-up HV-transformer with 1:n conversion turns ratio can be simplified as the transformer with 1:1 conversion turns ratio. After such simplification, the

corresponding secondary side quantities are transformed proportionally regarding those in 1:n transformer.

As mentioned in Section 2.2, in order to obtain the complete period sinusoidal VLF output voltage, besides the LCC resonant converter for charging, the adjustable resistive circuit is adopted for discharging. In practice, such discharge circuit is comprised of tens to hundreds of series-connected transistors, which operate in linear mode and their equivalent resistors are adjusted by the controllable gain voltage. Through a current control circuit, the transistors' gain voltages can be individually modulated to get the appropriate discharging resistors at each time point, the sine wave output voltage is then realized. Since the emphasis of this dissertaion is the LCC resonant converter, detailed discussion about the current control circuit and the discharge process would not be included. A constant discharge resistor is used in the next Chapters.

With above approximations and simplifications, the resulting simplified LCC resonant converter is shown in Fig. 2.8.

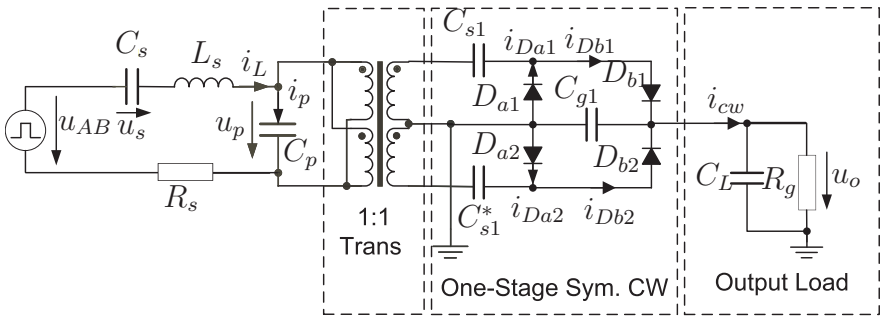

Figure 2.8: Simplified LCC resonant converter

Chapter 3

Modeling of the LCC Resonant Converter

3.1 Introduction

Modeling is an effective way to understand the operation behavior of a complex system, and becomes an important experimental and analytical tool to predict the steady-state and dynamic characteristics of a complex system before taking on any risk from technical, financial or actual construction.

In engineering, it is desired to model the important dominant behavior of a system, while neglecting other insignificant phenomena. Simplified terminal equations of the component elements are usually used, and many aspects of the system response are neglected. The resulting simplified model yields physical insight into the system behavior, which aids the engineer in designing the system to operate in a given specified manner. Thus, the modeling process involves use of approximations to neglect small but complicating phenomena, in an attempt to understand what is most important. It is a fact of life that real, physical systems are complex, and their detailed analysis can easily lead to an intractable and useless mathematical mess. Approximate models are an important tool for gaining understanding and physical insight.

Historically, there are some classic and extended modeling methods for switched power converters:

1. Middlebrook and Cuk created state-space averaging method in 1976, which is thought to be the mainstay of modern control theory [MC76]. It is widely

adopted in those systems, whose state variables have small ripple and can be linearly approximated. This method has been successfully applied to PWM power converters, but has limitation with switched circuits or resonant converters that do not satisfy the "small ripple" condition [MC76][ECM82].

2. Sampled-data modeling taken in [VEK86][VC83] for analysis and control design in resonant converters results in a small-signal model for the underlying resonant converter with the perturbation in switching frequency as the input. One difficulty with this approach is the requirement of obtaining a nominal periodic solution as a first step in the analysis. The utility of the resulting model is then limited by its small signal nature.

3. The phase plane method of [OL85] is a basic approach to obtaining a steady-state solution for a resonant converter, and the control scheme of [OYL87] based on this method is evidently effective. A limitation of this approach is its restriction to second order systems; it is not obvious how one can incorporate additional state variables that are associated with the load or the source dynamics.

4. Steigerwald introduced classical AC analysis techniques for deriving the steady-state characteristics of the resonant converters operating above resonance in 1988 [Ste88], which take the fundamental components of all the waveforms and load the resonant circuits with an equivalent resistance with consideration of the nonlinear behavior of the output rectifiers.

5. Sanders and Verghese published the generalized averaging method in 1989, which is thought to be a more general averaging scheme that can, in principle, accommodate arbitrary types of waveforms [SNL+91]. The method is based on a time-dependent Fourier series representation for a "sliding window" of a given waveform. This technique is shown to be effective to a much broader class of circuits and systems, including resonant type converters.

6. Eric Yang represented extended describing function concept in 1991, which principle assumption is to approximate the resonant waveforms by their fundamental components [YLJ91]. This method has very good transient

response correlation, but complex mathematical formulation and computational effort. This technique can only be used in continuous conduction modes.

In electrical engineering, physical large-signal modeling and small-signal modeling are common analysis techniques for years. Large-signal modeling is used to describe nonlinear devices in terms of the nonlinear equations, which is dedicated to predict the steady-state characteristics of the nonlinear system; while small-signal modeling is adopted to approximate the behavior of nonlinear devices with linear equations around its operating point with sufficient accuracy, which is useful for system dynamic characteristics estimation and model-based controller design.

3.2 Large-Signal Modeling of LCC Resonant Converter with a Capacitive Load

As aforementioned in Chapter 2, the derived simplified circuit diagram Fig. 3.1 is thought to be preferable for modeling the LCC resonant converter in the first quarter period of the VLF test voltage, since it replaces the original complicated circuits (Fig. 2.1) with consideration of the important dominant physical phenomena in both steady-state and dynamic aspects. The simplified LCC resonant converter is consisting of a full-bridge inverter with an input DC source, a LCC tank, a transformer with 1:1 conversion turns ratio, a symmetrical one-stage CW multiplier and a capacitive load.

Fig. 3.2 represents the simulated principal waveforms. From which, it can be seen that the resonant current i_L has a nearly sinusoidal shape with amplitude i_{LP}. This current flows continuously through series capacitor C_s, which shows a nearly sinusoidal voltage u_s. Voltage u_k remains at a nearly constant value, which is one half of the output voltage u_o. When u_p is lower than u_k, the rectifier is in the turn-off state, i_L flows through the parallel capacitor C_p completely. During this interval, voltage u_p shows piecewise sinusoidal evolution, which is determined by i_L and C_p. When u_p equals u_k, the rectifier diodes D_{b1} and D_{a2} turn on, the current flows either through C_{s1} and D_{b1} to the load or through D_{a2}

and C_{s1}* to return back. During this interval, u_p is clamped to $u_o/2$. When i_L reaches zero, the rectifier will turn off again, and the above process will be repeated with opposite sign. The sum of i_{Db1} and i_{Db2} yields the output current i_{cw}.

A. Nonlinear State Equations

After investigations of Fig. 3.1 and Fig. 3.2, the system behavior can be described by the following nonlinear state equations.

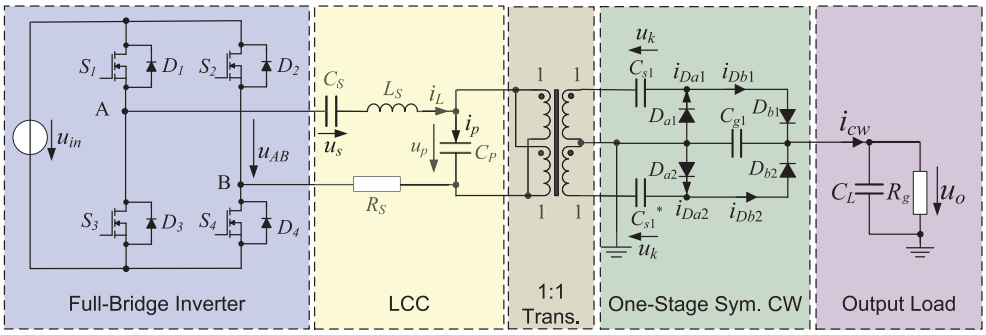

Figure 3.1: Simplified equivalent circuit of the LCC resonant converter with capacitive load

Among which, $u_{AB}(t)$ is the output voltage of full-bridge inverter, R_s is the approximated series resistance with consideration of the circuit losses in the full-bridge inverter and the LCC tank; C_{s1}, C_{s1}*, C_{g1} are capacitors of the CW multiplier, and C_L is the output capacitor; R_g reflects the discharge resistor, which is assumed to be constant in the studied quarter period.

$$\begin{aligned}
\frac{di_L(t)}{dt} &= \frac{u_{AB}(t) - R_s \cdot i_L(t) - u_s(t) - u_p(t)}{L_s} \\
\frac{du_s(t)}{dt} &= \frac{1}{C_s} \cdot i_L(t) \\
\frac{du_o(t)}{dt} &= \frac{1}{C_L} \cdot \left(i_{cw}(t) - \frac{u_o(t)}{R_g} \right)
\end{aligned} \tag{3.1}$$

Apparently, three independent variables, inductor current $i_L(t)$, voltage $u_s(t)$, and output voltage $u_o(t)$ are taken as the components of the state vector:

$$\mathbf{x}_o(t) = [i_L(t), u_s(t), u_o(t)]^T \tag{3.2}$$

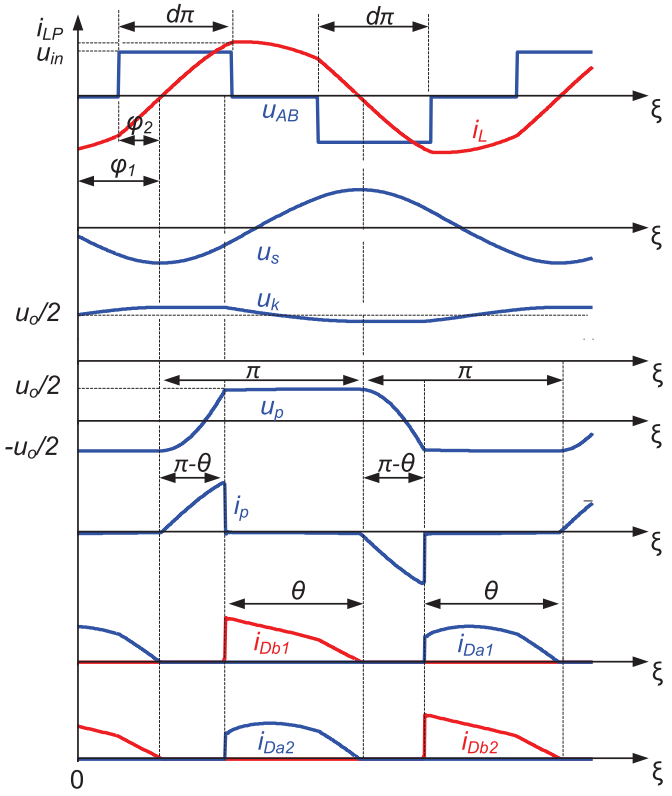

Figure 3.2: Main waveforms of LCC resonant converter

As aforementioned, $u_p(t)$ is not independent, but determined by $i_L(t)$ and $u_o(t)$, it is not considered as a state variable.

B. State Variable Harmonic Approach

The generalized averaging method [SNL+91] is adopted for the resonant converter modeling, which is based on the fact that the state variable can be approximated in a period $[0, T_s]$ by a Fourier series representation of the form:

$$f(t) = \sum_{m=-\infty}^{+\infty} f_{(m)} \cdot e^{jm\omega_s t},\ f_{(m)} = \frac{1}{T_s}\int_0^{T_s} f(t) \cdot e^{-jm\omega_s t}dt,\ \omega_s = \frac{2\pi}{T_s} = 2\pi f_s. \quad (3.3)$$

Since the resonant current $i_L(t)$ and the voltage $u_s(t)$ are predominantly sinusoidal (Fig. 3.2), it is accurate enough to approximate them by their fundamental terms in the Fourier series. The following equations are obtained if the sinusoidal formulation is used:

$$i_L(t) \approx i_{Ls}\sin(\omega_s t) + i_{Lc}\cos(\omega_s t) \tag{3.4}$$

$$u_s(t) \approx u_{ss}\sin(\omega_s t) + u_{sc}\cos(\omega_s t) \tag{3.5}$$

where i_{Ls}, i_{Lc} and u_{ss}, u_{sc} are their 1st-order Fourier coefficients.

The resonant current amplitude i_{Lp} and the effective resonant current i_{Leff} are denoted as below, respectively.

$$i_{Lp} = \sqrt{i_{Ls}^2 + i_{Lc}^2} \tag{3.6}$$

$$i_{Leff} = \sqrt{\frac{i_{Ls}^2 + i_{Lc}^2}{2}} \tag{3.7}$$

Since the output VLF sinusoidal voltage u_o varies very slowly compared to the resonant quantities, a zero-order approximation is implemented.

Based on above approximations, the initial state vector $\mathbf{x}_o$ now can be replaced with the new state vector $\mathbf{x}$.

$$\mathbf{x} = [i_{Ls}, i_{Lc}, u_{ss}, u_{sc}, u_o]^T \tag{3.8}$$

Due to the wide range of the output voltage and the output load, both the switching frequency ω_s and the duty cycle d are adopted as the control variables. Considering the input DC voltage u_{in}, the corresponding input vector $\mathbf{u}$ is defined as:

$$\mathbf{u} = [u_{in}, d, \omega_s]^T \tag{3.9}$$

The output vector $\mathbf{y}$ is defined as:

$$\mathbf{y} = [u_o, i_{cw}, i_{Lp}]^T \tag{3.10}$$

C. Extended Describing Functions (EDFs)

The state equations Eq. 3.1 cannot be explicitly solved because the terms: $u_{AB}(t)$, $u_p(t)$ and $i_{cw}(t)$ are unknown. It is necessary to represent them with the new state variables and the control variables. The EDF concept [YLJ91] is adopted. That is to say, $u_{AB}(t)$, $u_p(t)$ and $i_{cw}(t)$ will be represented as their Fourier formulation,

respectively. With neglecting the insignificant phenomena, they are approximated either by the fundamental terms or only by the DC terms of their Fourier series, as shown below:

1) The output voltage from the full-bridge inverter u_{AB} has a quasi-square form, which is relevant to the input DC voltage u_{in} and duty cycle d. u_{AB} is approximated by its fundamental components.

$$u_{AB}(\xi) \approx u_{AB(1)} \cdot e^{j\xi} + u_{AB(-1)} \cdot e^{-j\xi} = \frac{4}{\pi} u_{in} \sin\left(\frac{d\pi}{2}\right) \sin(\xi),\ \xi = \omega_s t \quad (3.11)$$

2) With the information from Fig. 3.1 and Fig. 3.2, it can be seen that when diodes D_{b1} and D_{a2} are on, $i_p \approx 0$, $i_{Db1} \approx i_{Da2} \approx 0.5 i_L$; similarly, when diodes D_{b2} and D_{a1} are on, $i_{Db2} \approx i_{Da1} \approx 0.5 i_L$. The sum of i_{Db1} and i_{Db2} yields i_{cw}, which is approximated only by the DC component.

$$i_{cw} \approx 2 i_{Db1(0)} = \frac{1}{2\pi} \int_{\pi-\theta}^{\pi} i_{Lp} \sin(\xi) e^{-j0\xi} d\xi = \frac{(1-\cos\theta)\sqrt{i_{Ls}^2 + i_{Lc}^2}}{2\pi} \quad (3.12)$$

here, θ is the conduction angle of the diode D_{b1}.

3) According to Fig. 3.2, $u_p(\xi)$ can be described piecewise as follows [MRDP+07]:

$$u_p(\xi) \approx -\frac{u_o}{2} + \frac{i_{Lp}\left[1 - \cos(\xi - \varphi_1)\right]}{C_p \cdot \omega_s},\ \varphi_1 \le \xi \le \pi - \theta + \varphi_1 \quad (3.13)$$

$$u_p(\xi) \approx \frac{u_o}{2} - \frac{i_{Lp}\left[1 + \cos(\xi - \varphi_1)\right]}{C_p \cdot \omega_s},\ \pi + \varphi_1 \le \xi \le 2\pi - \theta + \varphi_1 \quad (3.14)$$

$$u_p(\xi) \approx \frac{u_o}{2},\ \pi - \theta + \varphi_1 \le \xi \le \pi + \varphi_1 \quad (3.15)$$

$$u_p(\xi) \approx -\frac{u_o}{2},\ 2\pi - \theta + \varphi_1 \le \xi \le 2\pi + \varphi_1 \quad (3.16)$$

The fundamental terms of the Fourier series of u_p are considered:

$$u_p(\xi) \approx u_{p(1)} \cdot e^{j\xi} + u_{p(-1)} \cdot e^{-j\xi} = u_{ps} \cdot \sin(\xi) + u_{pc} \cdot \cos(\xi) \quad (3.17)$$

where

$$u_{ps} = \frac{i_{Lc}}{\pi C_p \omega_s}\left[\pi - \theta + \frac{1}{2}\sin(2\theta)\right] + \frac{i_{Ls}}{\pi C_p \omega_s}\sin^2(\theta) \quad (3.18)$$

$$u_{pc} = \frac{i_{Lc}}{\pi C_p \omega_s} \sin^2(\theta) - \frac{i_{Ls}}{\pi C_p \omega_s} \left[\pi - \theta + \frac{1}{2} \sin(2\theta) \right] \tag{3.19}$$

4) At the end of the diode conduction phase, where $\xi = \pi - \theta + \varphi_1$, u_p can be represented as Eq. 3.20 based on Fig. 3.2, Eq. 3.13 and Eq. 3.15.

$$u_p(\xi) \approx \frac{u_o}{2} \approx -\frac{u_o}{2} + \frac{i_{Lp} \left[1 - \cos(\pi - \theta) \right]}{C_p \cdot \omega_s} \tag{3.20}$$

The conduction angle θ is further derived as follow.

$$\theta = \cos^{-1} \left[\frac{C_p \omega_s u_o}{i_{Lp}} - 1 \right] \tag{3.21}$$

Till now, all the nonlinear terms: $u_{AB}(t)$, $u_p(t)$, $i_{cw}(t)$ and $\theta(t)$ are represented by the new state variables and the control variables.

D. Harmonic Balance

By substituting the initial state variables and the nonlinear terms in Eq.3.1 with the results of the harmonic approximation in Section B and the EDFs in Section C, and by equating the coefficients of DC, sine and cosine terms respectively, the state equations Eq.3.1 can then be rewritten. The newly derived state equations are shown in Eq. 3.22. Here, the switching frequency ω_s and the duty cycle d are assumed as time-invariant magnitudes.

$$\frac{di_{Ls}}{dt} = \frac{1}{L_s} \left[\frac{4u_{in} \sin(\frac{\pi}{2}d)}{\pi} - R_s i_{Ls} - u_{ss} - \frac{i_{Ls} \sin^2\theta + i_{Lc} \left(\pi - \theta + \frac{\sin(2\theta)}{2} \right)}{\pi \omega_s C_p} + L_s \omega_s i_{Lc} \right] \tag{3.22a}$$

$$\frac{di_{Lc}}{dt} = \frac{1}{L_s} \left[-R_s i_{Lc} - u_{sc} - \frac{i_{Lc} \sin^2\theta - i_{Ls} \left(\pi - \theta + \frac{\sin(2\theta)}{2} \right)}{\pi \omega_s C_p} - L_s \omega_s i_{Ls} \right] \tag{3.22b}$$

$$\frac{du_{ss}}{dt} = \frac{1}{C_s} \cdot i_{Ls} + \omega_s \cdot u_{sc} \tag{3.22c}$$

$$\frac{du_{sc}}{dt} = \frac{1}{C_s} \cdot i_{Lc} - \omega_s \cdot u_{ss} \tag{3.22d}$$

$$\frac{du_o}{dt} = \frac{1}{C_L} \left[\frac{(1 - \cos\theta)\sqrt{i_{Ls}^2 + i_{Lc}^2}}{2\pi} - \frac{u_o}{R_g} \right] \tag{3.22e}$$

E. Quasi-Steady-State Solution

For quasi-steady-state analysis, since the state variables in Eq. 3.22 are regarded

as varying slowly in time, it is reasonable to set their derivatives to zero to obtain the quasi-steady-state solutions.

At each quiescent operating point, both the sinusoidal output voltage and the corresponding cosinoidal output current can be regarded as constant at the specified time point. It is then possible to approximate the output capacitance C_L as an equivalent resistance R_L at this time point for steady-state analysis. Such resistance R_L is parallel connected with the discharge resistance R_g and comprises the output resistance R_o for quasi-steady-state analysis.

$$R_o = \frac{R_L \cdot R_g}{R_L + R_g} \tag{3.23}$$

Since the VLF output voltage $u_o(t)$ is regarded as DC voltage U_o at quasi-steady-state, only the average value of the output current $i_{cw}(t)$ is considered for quasi-steady-state analysis.

$$i_{cw(0)} \approx \frac{U_o}{R_o} \tag{3.24}$$

The CW multiplier diode conduction angle θ can be simplified as θ_{ss} at quasi-steady-state condition by using Eq. 3.12, Eq. 3.20 and Eq. 3.24. Among which, Ω_s is the quasi-steady-state magnitude of ω_s.

$$\theta_{ss} = 2tg^{-1}\sqrt{\frac{2\pi}{C_p\Omega_s R_o}} \tag{3.25}$$

The other quasi-steady-state solutions of the state variables are attached in Appendix A.

3.3 Steady-State Characteristics and Verification

According to above quasi-steady-state analysis and the large-signal model, the steady-state characteristics of the LCC resonant converter can be obtained, as shown in Fig. 3.3. Among which, Fig. 3.3(a) represents the voltage conversion ratio M vs. the normalized switching frequency f_{sn} with the constant duty cycle: $d = 0.95$; while Fig. 3.3(b) represents M vs. d with the constant switching frequency: $f_s = 40$kHz. The LCC resonant converter operation region is marked as the shaded area, which are determined by the given output voltage range,

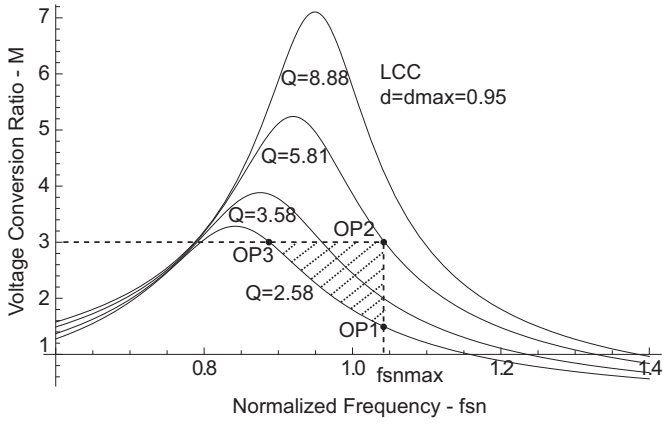

(a)

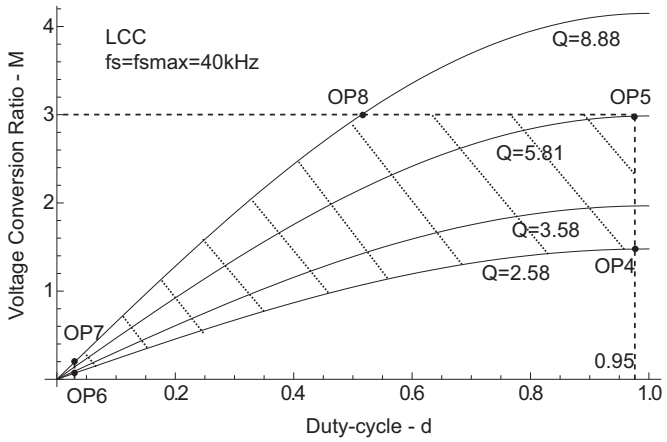

(b)

Figure 3.3: Voltage conversion ratio of LCC resonant converter vs. (a) normalized switching frequency f_{sn} and (b) duty cycle d

load range and modulation limit of f_s and d. OP1-OP8 are the corresponding boundary operating points. Below equations provide the parameters' definition for Fig. 3.3. Among which, n is the conversion turns ratio of the HV-transformer, k is the stage number of the CW multiplier.

$$M = \frac{U_o}{2nkU_{in}} \tag{3.26}$$

$$f_{sn} = \frac{\omega_s}{2\pi f_0} = \frac{f_s}{f_0} \tag{3.27}$$

$$f_0 = \frac{1}{2\pi\sqrt{L_s C_g}} \tag{3.28}$$

$$C_g = \frac{C_s C_p}{C_s + C_p} \tag{3.29}$$

$$Z = \sqrt{\frac{L_s}{C_g}} \tag{3.30}$$

$$Q = \frac{R_o}{2^2 n^2 k^2 Z} \tag{3.31}$$

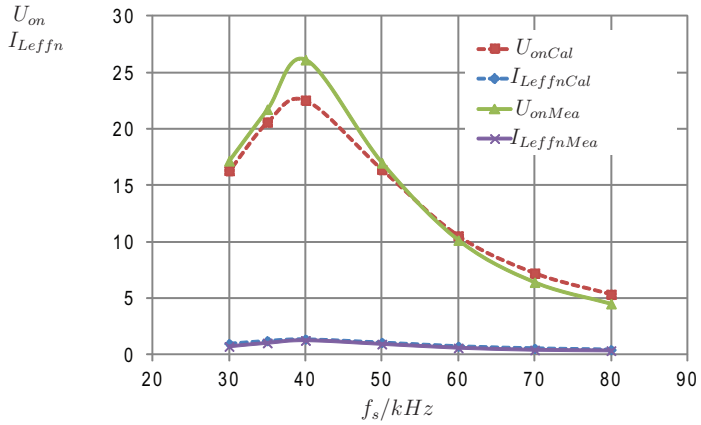

(a) $d = 0.4$

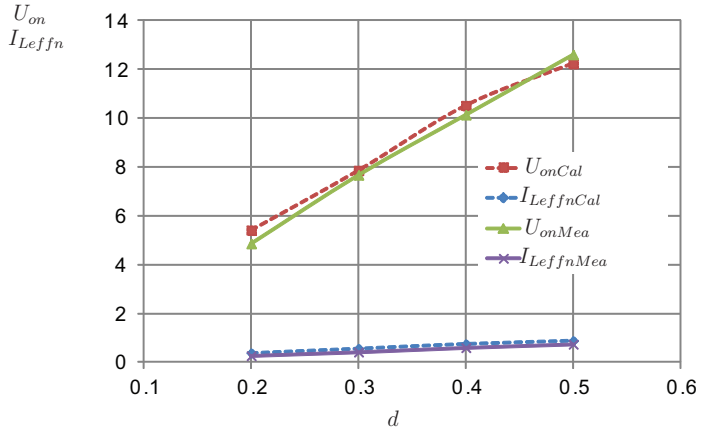

(b) $f_s = 60$ kHz

Figure 3.4: Normalized steady-state characteristics with LCC resonant converter parameters: $L_s = 600$ μH, $C_s = 100$ nF, $C_p = 22$ nF, $n = 7$, $k = 2$, $U_{in} = 109.5$ V, $R_s = 10$ Ω, $R_o = 250$ kΩ

The predicted and experimental results are provided in Fig. 3.4, the output voltage and the resonant current are predicted based on the derived large-signal

model (Eq.3.22) and CW multiplier voltage drop (Eq.2.6). Among which, Fig. 3.4(a) gives the results of the normalized output average voltage U_{on} and the normalized effective resonant current $I_{L_{effn}}$ regarding variable f_s and constant d, while Fig. 3.4(b) represents the results of U_{on} and $I_{L_{effn}}$ regarding variable d and constant f_s. The red and blue dash lines denote the predicted voltage U_{onCal} and current $I_{LeffnCal}$, respectively; while the green and purple solid lines denote the measured voltage U_{onMea} and current $I_{LeffnMea}$, respectively.

From Fig. 3.4, a general close correspondence is seen between the predicted and experimental results, which verifies the correctness of the derived large-signal model and the voltage drop from CW multiplier circuit. Some deviation between them is due to the coarsely approximated R_s, which is assumed with consideration of the circuit losses from the full-bridge inverter and the LCC tank, the additional losses in magnetic components and stray capacitors' effect in CW multiplier are not taken into account. A more detailed investigation about the LCC resonant converter losses should be implemented for a more accurate steady-state characteristics prediction.

3.4 Small-Signal Modeling and Verification

F. Linearization

The corresponding linearized small-signal model can be deduced via a small-signal perturbation around the quasi-steady-state operating point. As shown in Eq. 3.32, the state variable $\mathbf{x}(t)$ and the corresponding input $\mathbf{u}(t)$ and output $\mathbf{y}(t)$ are divided into their quasi-steady-state part: $\mathbf{X}_d$, $\mathbf{U}_d$, $\mathbf{Y}_d$ and the small-signal pertubation part: $\delta\mathbf{x}(t)$, $\delta\mathbf{u}(t)$, $\delta\mathbf{y}(t)$, respectively.

$$\begin{aligned} \mathbf{x}(t) &= \mathbf{X}_d + \delta\mathbf{x}(t) \\ \mathbf{u}(t) &= \mathbf{U}_d + \delta\mathbf{u}(t) \\ \mathbf{y}(t) &= \mathbf{Y}_d + \delta\mathbf{y}(t) \end{aligned} \tag{3.32}$$

where

$$\begin{aligned} \mathbf{X}_d &= [I_{Ls}, I_{Lc}, U_{ss}, U_{sc}, U_o]^T \\ \mathbf{U}_d &= [U_{in}, D, \Omega_s]^T \\ \mathbf{Y}_d &= [U_o, I_{cw}, I_{Lp}]^T \end{aligned} \tag{3.33}$$

$$\begin{aligned}\delta\mathbf{x} &= [\delta i_{Ls}, \delta i_{Lc}, \delta u_{ss}, \delta u_{sc}, \delta u_o]^T \\ \delta\mathbf{u} &= [\delta u_{in}, \delta d, \delta\omega_s]^T \\ \delta\mathbf{y} &= [\delta u_o, \delta i_{cw}, \delta i_{Lp}]^T\end{aligned} \tag{3.34}$$

The linearized small-signal model of the LCC resonant converter at the specified operating point ($\mathbf{X}_d$, $\mathbf{U}_d$) is represented as below.

$$\delta\dot{\mathbf{x}} = \mathbf{A}_c(\mathbf{X}_d, \mathbf{U}_d) \cdot \delta\mathbf{x} + \mathbf{B}_c(\mathbf{X}_d, \mathbf{U}_d) \cdot \delta\mathbf{u} \tag{3.35}$$

$$\delta\mathbf{y} = \mathbf{C}_c(\mathbf{X}_d, \mathbf{U}_d) \cdot \delta\mathbf{x} + \mathbf{E}_c(\mathbf{X}_d, \mathbf{U}_d) \cdot \delta\mathbf{u} \tag{3.36}$$

where

$$\begin{aligned}
\mathbf{A}_c(\mathbf{X}_d, \mathbf{U}_d) &= \left.\frac{\partial\mathbf{f}(\mathbf{x},\mathbf{u})}{\partial\mathbf{x}}\right|_{\mathbf{x}=\mathbf{X}_d,\mathbf{u}=\mathbf{U}_d} = \left[\begin{array}{cccc:c} a_{11} & a_{12} & a_{13} & 0 & a_{15} \\ a_{21} & a_{22} & 0 & a_{24} & a_{25} \\ a_{31} & 0 & 0 & a_{34} & 0 \\ 0 & a_{42} & a_{43} & 0 & 0 \\ \hdashline a_{51} & a_{52} & 0 & 0 & a_{55} \end{array}\right] \\
\mathbf{B}_c(\mathbf{X}_d, \mathbf{U}_d) &= \left.\frac{\partial\mathbf{f}(\mathbf{x},\mathbf{u})}{\partial\mathbf{u}}\right|_{\mathbf{x}=\mathbf{X}_d,\mathbf{u}=\mathbf{U}_d} = \left[\begin{array}{ccc} b_{11} & b_{12} & b_{13} \\ 0 & 0 & b_{23} \\ 0 & 0 & b_{33} \\ 0 & 0 & b_{43} \\ \hdashline 0 & 0 & b_{53} \end{array}\right] \\
\mathbf{C}_c(\mathbf{X}_d, \mathbf{U}_d) &= \left.\frac{\partial\mathbf{g}(\mathbf{x},\mathbf{u})}{\partial\mathbf{x}}\right|_{\mathbf{x}=\mathbf{X}_d,\mathbf{u}=\mathbf{U}_d} = \left[\begin{array}{cccc:c} 0 & 0 & 0 & 0 & 1 \\ \hdashline c_{21} & c_{22} & 0 & 0 & c_{25} \\ c_{31} & c_{32} & 0 & 0 & 0 \end{array}\right] \\
\mathbf{E}_c(\mathbf{X}_d, \mathbf{U}_d) &= \left.\frac{\partial\mathbf{g}(\mathbf{x},\mathbf{u})}{\partial\mathbf{u}}\right|_{\mathbf{x}=\mathbf{X}_d,\mathbf{u}=\mathbf{U}_d} = \left[\begin{array}{ccc} 0 & 0 & 0 \\ \hdashline 0 & 0 & e_{23} \\ 0 & 0 & 0 \end{array}\right]
\end{aligned} \tag{3.37}$$

Each non-zero element in the matrices $\mathbf{A}_c$, $\mathbf{B}_c$ and $\mathbf{C}_c$ is listed in Appendix B.

An analytical derivation for the LCC resonant converter was implemented under the small-signal assumptions using computer algebra tool (Mathematica, etc.). The resulting equivalent circuit of the small-signal model is depicted in Fig. 3.5, the corresponding parameters are attached in Appendix C [HFB09b]. Those parameters vary, however, depending on the given operating point.

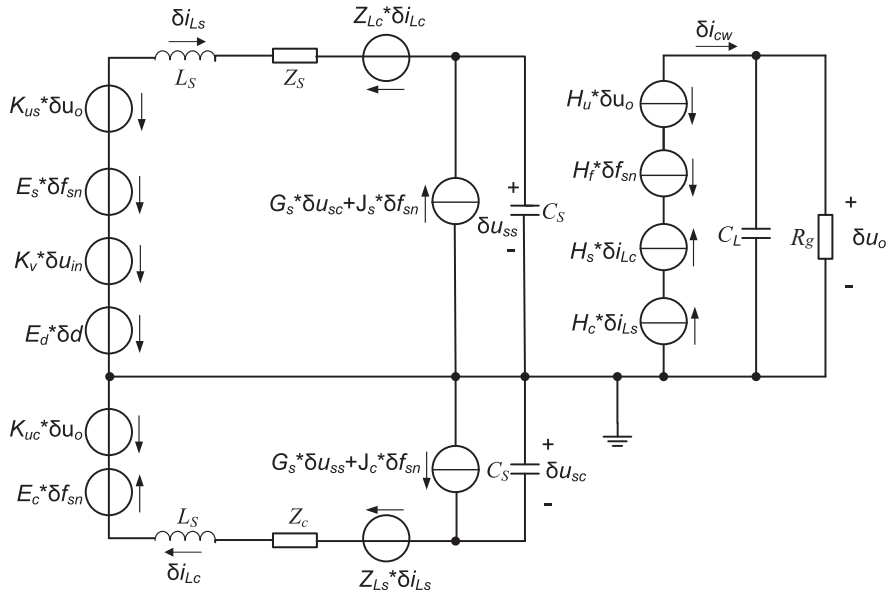

Figure 3.5: Small-signal equivalent circuit model of LCC resonant converter with capacitive load

G. Normalization and Transfer Functions

Normalization was further implemented in order to generalize the modeling. The base magnitudes are fictive supply current I_B, input voltage U_{in} and the resonant frequency Ω_0. Among which,

$$I_B = \frac{U_{in}}{Z}, \tag{3.38}$$

U_{in} is the steady-state input voltage, and Ω_0 is the steady-state resonant frequency.

The normalized state variables, input variables and output variables are represented below.

$$\delta i_{Lsn} = \frac{\delta i_{Ls}}{I_B}, \delta i_{Lcn} = \frac{\delta i_{Lc}}{I_B}, \delta u_{ssn} = \frac{\delta u_{ss}}{U_{in}}, \delta u_{scn} = \frac{\delta u_{sc}}{U_{in}}, \tag{3.39}$$

$$\delta u_{inn} = \frac{\delta u_{in}}{U_{in}}, \delta d_n = \delta d, \delta \omega_{sn} = \frac{\delta \omega_s}{\Omega_0}, \tag{3.40}$$

$$\delta u_{on} = \frac{\delta u_o}{U_{in}}, \delta i_{cwn} = \frac{\delta i_{cw}}{I_B}, \delta i_{Lpn} = \frac{\delta i_{Lp}}{I_B}. \tag{3.41}$$

After normalization, the system matrices: $\mathbf{A}_c$, $\mathbf{B}_c$ and $\mathbf{C}_c$, are transferred as the normalized one: $\mathbf{A}_{cn}$, $\mathbf{B}_{cn}$ and $\mathbf{C}_{cn}$, respectively. The corresponding normalized small-signal model of the LCC resonant converter at the specified normalized operating point ($\mathbf{X}_{dn}$, $\mathbf{U}_{dn}$) are provided below.

$$\delta\dot{\mathbf{x}}_n = \mathbf{A}_{cn}(\mathbf{X}_{dn}, \mathbf{U}_{dn}) \cdot \delta\mathbf{x}_n + \mathbf{B}_{cn}(\mathbf{X}_{dn}, \mathbf{U}_{dn}) \cdot \delta\mathbf{u}_n \tag{3.42}$$

$$\delta\mathbf{y}_n = \mathbf{C}_{cn}(\mathbf{X}_{dn}, \mathbf{U}_{dn}) \cdot \delta\mathbf{x}_n + \mathbf{E}_{cn}(\mathbf{X}_{dn}, \mathbf{U}_{dn}) \cdot \delta\mathbf{u}_n \tag{3.43}$$

where

$$\begin{aligned}
\mathbf{A}_{cn}(\mathbf{X}_{dn}, \mathbf{U}_{dn}) &= \left.\frac{\partial \mathbf{f}(\mathbf{x}_n, \mathbf{u}_n)}{\partial \mathbf{x}_n}\right|_{\mathbf{x}_n=\mathbf{X}_{dn}, \mathbf{u}_n=\mathbf{U}_{dn}} = \left[\begin{array}{cccc:c} a_{11n} & a_{12n} & a_{13n} & 0 & a_{15n} \\ a_{21n} & a_{22n} & 0 & a_{24n} & a_{25n} \\ a_{31n} & 0 & 0 & a_{34n} & 0 \\ 0 & a_{42n} & a_{43n} & 0 & 0 \\ \hdashline a_{51n} & a_{52n} & 0 & 0 & a_{55n} \end{array}\right] \\
\mathbf{B}_{cn}(\mathbf{X}_{dn}, \mathbf{U}_{dn}) &= \left.\frac{\partial \mathbf{f}(\mathbf{x}_n, \mathbf{u}_n)}{\partial \mathbf{u}_n}\right|_{\mathbf{x}_n=\mathbf{X}_{dn}, \mathbf{u}_n=\mathbf{U}_{dn}} = \left[\begin{array}{ccc} b_{11n} & b_{12n} & b_{13n} \\ 0 & 0 & b_{23n} \\ 0 & 0 & b_{33n} \\ 0 & 0 & b_{43n} \\ \hdashline 0 & 0 & b_{53n} \end{array}\right] \\
\mathbf{C}_{cn}(\mathbf{X}_{dn}, \mathbf{U}_{dn}) &= \left.\frac{\partial \mathbf{g}(\mathbf{x}_n, \mathbf{u}_n)}{\partial \mathbf{x}_n}\right|_{\mathbf{x}_n=\mathbf{X}_{dn}, \mathbf{u}_n=\mathbf{U}_{dn}} = \left[\begin{array}{cccc:c} 0 & 0 & 0 & 0 & 1 \\ \hdashline c_{21n} & c_{22n} & 0 & 0 & c_{25n} \\ c_{31n} & c_{32n} & 0 & 0 & 0 \end{array}\right] \\
\mathbf{E}_{cn}(\mathbf{X}_{dn}, \mathbf{U}_{dn}) &= \left.\frac{\partial \mathbf{g}(\mathbf{x}_n, \mathbf{u}_n)}{\partial \mathbf{u}_n}\right|_{\mathbf{x}_n=\mathbf{X}_{dn}, \mathbf{u}_n=\mathbf{U}_{dn}} = \left[\begin{array}{ccc} 0 & 0 & 0 \\ \hdashline 0 & 0 & e_{23n} \\ 0 & 0 & 0 \end{array}\right]
\end{aligned} \tag{3.44}$$

Each non-zero element in the matrices $\mathbf{A}_{cn}$, $\mathbf{B}_{cn}$ and $\mathbf{C}_{cn}$ is listed in Appendix D.

Based on the normalized system matrices, the control-to-output transfer functions of the LCC resonant converter can be obtained.

$$\mathbf{G}_{cn}(s) = \mathbf{C}_{cn} \cdot \left[s_n\mathbf{I} - \mathbf{A}_{cn}\right]^{-1} \cdot \mathbf{B}_{cn} \tag{3.45}$$

In order to verify the small-signal model of the LCC resonant converter, an experimental setup is built for control-to-output transfer function's measurement, whose schematic diagram is shown in Fig. 3.6.

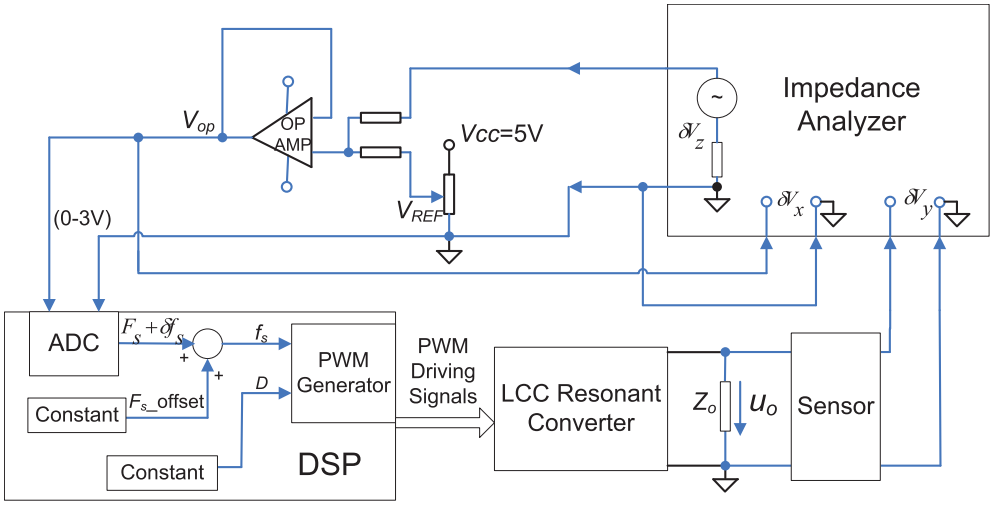

Figure 3.6: Schematic diagram of control-to-output transfer function measurement

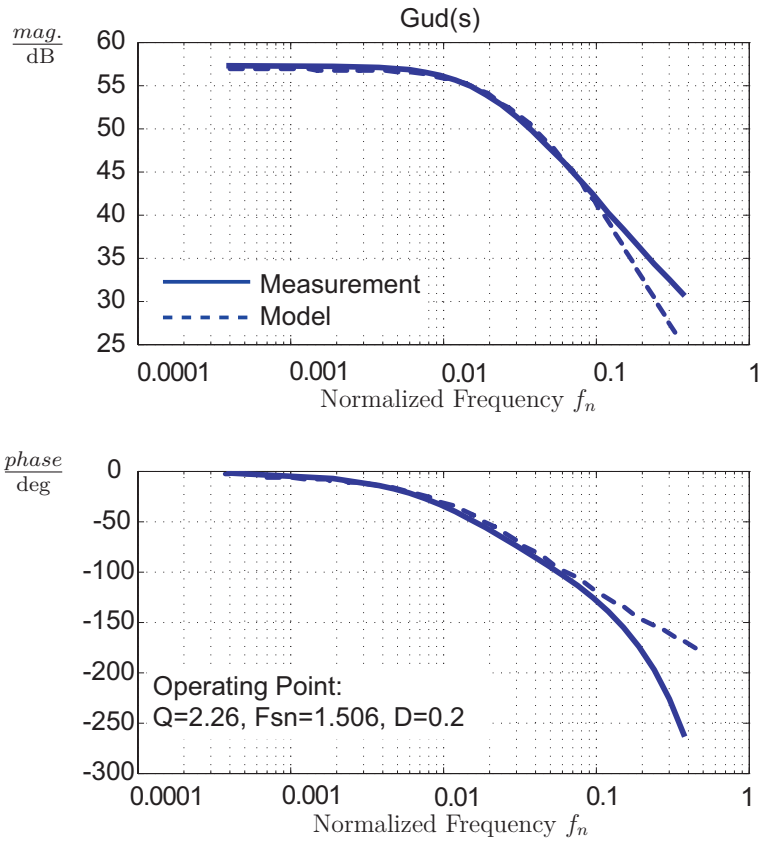

Figure 3.7: Control-to-output transfer functions comparison: variable duty cycle with constant switching frequency (f_s=40 kHz)

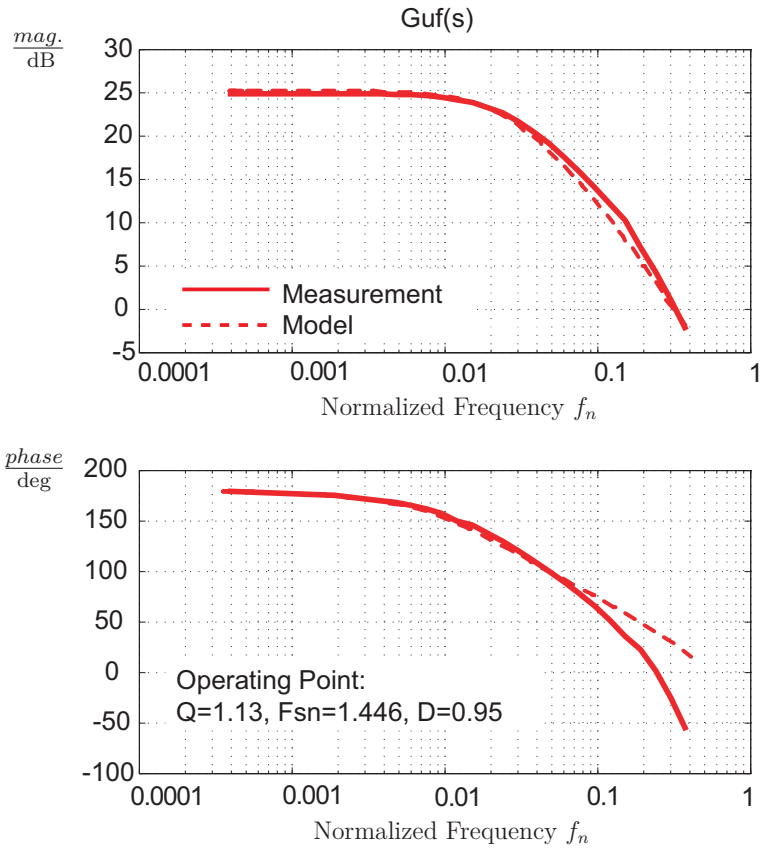

Figure 3.8: Control-to-output transfer functions comparison: Variable switching frequency with constant duty cycle (d=0.95)

A small-signal perturbation with sweeping frequency is generated from an impedance analyzer and sent to a conditioning circuit. After simple signal processing and A/D converting, such small-signal perturbation is given to the PWM generator in a DSP, and the corresponding PWM driving signals with a small perturbation are created and sent to the LCC resonant converter. Through measuring the output voltage of the LCC resonant converter, the control-to-output transfer function can be obtained.

The predicted and measured control-to-output transfer functions are represented in Fig. 3.7 and Fig. 3.8. Fig. 3.7 shows the Bode diagram of d-to-u_{on} transfer function at the steady-state operating point: $Q = 2.26$, $F_{sn} = 1.506$, $D = 0.2$; while Fig. 3.8 shows the Bode diagram of f_{sn}-to-u_{on} transfer function at the steady-state operating point: $Q = 1.13$, $F_{sn} = 1.446$, $D = 0.95$. Among

which, F_{sn} and D denotes the steady-state normalized switching frequency and duty cycle, respectively.

$$F_{sn} = \frac{F_s}{f_0} \tag{3.46}$$

The solid line is based on the experimental results, while the dash line is predicted from the small-signal model. It can be seen that in the most interested frequency range, the measured control-to-output characteristics are agree with those of the predicted results. There has some deviation in high frequency range, but since they have little effect on the closed-loop performance, and can be neglected.

3.5 Modeling of LCC Resonant Converter with a Voltage Source Load

Since the LCC resonant converter has a capacitive output load C_L, the output voltage u_o across over C_L is almost a constant and cannot be changed instantaneously. It is then reasonable to adopt an equivalent voltage source to replace the capacitive load C_L, which is likely to simplifiy above modeling process.

Fig. 3.9 gives the schematic diagram of the LCC resonant converter with a voltage source load. Based on the aforementioned large- and small-signal modeling with a capacitive load, a similar derivation for the LCC resonant converter with a voltage source load is provided below.

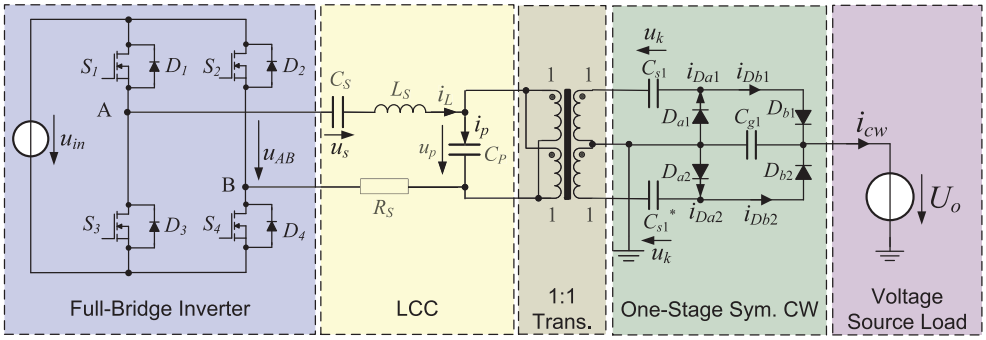

Figure 3.9: Simplified equivalent circuit of the LCC resonant converter with voltage source load

A. Nonlinear State Equations

The nonlinear state equations of the LCC resonant converter with a voltage source load is represented in Eq. 3.47. Compared to the state equations with a capacitive load shown in Eq. 3.1, the following state equations have only two state variables: resonant current i_L, and series capacitor voltage u_s. Since the present output load is a given voltage source, the output voltage $u_o(t)$ is regarded as a constant U_o, the corresponding third differential equation in Eq. 3.1 about $u_o(t)$ can be neglected.

$$\begin{aligned} \frac{di_L(t)}{dt} &= \frac{u_{AB}(t) - R_s \cdot i_L(t) - u_s(t) - u_p(t)}{L_s} \\ \frac{du_s(t)}{dt} &= \frac{1}{C_s} \cdot i_L(t) \end{aligned} \tag{3.47}$$

The symbols and parameters in Eq. 3.47 have the same definitions as those in Eq. 3.1. The present state vector $\mathbf{x}_o(t)$ is comprised of $i_L(t)$ and $u_s(t)$.

$$\mathbf{x}_o(t) = [i_L(t), u_s(t)]^T \tag{3.48}$$

B. State Variable Harmonic Approach

Similar as Eq. 3.4 and Eq. 3.5, adopting the generalized averaging method [SNL+91], $i_L(t)$ and $u_s(t)$ can be approximated quite accurately by their first-order Fourier series representations, respectively. The corresponding first-order Fourier coefficients: i_{Ls}, i_{Lc}, u_{ss} and u_{sc} are adopted as the new state variables.

$$\mathbf{x} = [i_{Ls}, i_{Lc}, u_{ss}, u_{sc}]^T \tag{3.49}$$

C. Extended Describing Functions (EDFs)

Similar as before, the extended describing functions concept [YLJ91] is adopted to solve the nonlinear terms in state equations Eq. 3.47. Among which, $u_{AB}(t)$, $i_{cw}(t)$ and $u_p(t)$ has the same representation as those in the LCC resonant converter with a capacitive load. Only the CW multiplier diode conduction angle θ has a little change due to the constant U_o, as shown below.

$$\theta = \cos^{-1}\left[\frac{C_p \omega_s U_o}{i_{Lp}} - 1\right] \tag{3.50}$$

Since all the nonlinear terms are expressed by the state variables and the control variables, the state equations Eq. 3.47 can be solved.

D. Harmonic Balance

Based on the results of Section B and Section C, the new state equations can be derived, as shown in Eq. 3.51. The switching frequency ω_s and the duty cycle d are assumed as time-invariant magnitudes.

$$\frac{di_{Ls}}{dt} = \frac{1}{L_s}\left[\frac{4u_{in}\sin(\frac{\pi}{2}d)}{\pi} - R_s i_{Ls} - u_{ss} - \frac{i_{Ls}\sin^2\theta + i_{Lc}\left(\pi - \theta + \frac{1}{2}\sin(2\theta)\right)}{\pi\omega_s C_p} + L_s\omega_s i_{Lc}\right] \tag{3.51a}$$

$$\frac{di_{Lc}}{dt} = \frac{1}{L_s}\left[-R_s i_{Lc} - u_{sc} - \frac{i_{Lc}\sin^2\theta - i_{Ls}\left(\pi - \theta + \frac{1}{2}\sin(2\theta)\right)}{\pi\omega_s C_p} - L_s\omega_s i_{Ls}\right] \tag{3.51b}$$

$$\frac{du_{ss}}{dt} = \frac{1}{C_s}\cdot i_{Ls} + \omega_s \cdot u_{sc} \tag{3.51c}$$

$$\frac{du_{sc}}{dt} = \frac{1}{C_s}\cdot i_{Lc} - \omega_s \cdot u_{ss} \tag{3.51d}$$

Due to the constant output voltage U_o, compared to Eq. 3.10, the output vector $\mathbf{y}$ of the LCC resonant converter with a voltage source load is simplified as below.

$$\mathbf{y} = [i_{cw}, i_{Lp}]^T \tag{3.52}$$

E. Quasi-Steady-State Solution

Since the quasi-steady-state solutions of the LCC large-signal model with a voltage source load are same as those with a capacitive load, the details are not repeated here.

F. Linearization and Small-Signal Model

Based on the nonlinear state equations Eq. 3.51: $\dot{\mathbf{x}} = \mathbf{f}(\mathbf{x}, \mathbf{u})$ and the output equations Eq. 3.52: $\mathbf{y} = \mathbf{g}(\mathbf{x}, \mathbf{u})$, the corresponding linearized small-signal model of the LCC resonant converter with a voltage source load can be deduced via

a small-signal perturbation around the quasi-steady-state operating point: ($\mathbf{X}_d$, $\mathbf{U}_d$), as shown below.

$$\delta\dot{\mathbf{x}} = \mathbf{A}_u(\mathbf{X}_d, \mathbf{U}_d) \cdot \delta\mathbf{x} + \mathbf{B}_u(\mathbf{X}_d, \mathbf{U}_d) \cdot \delta\mathbf{u} \tag{3.53}$$

$$\delta\mathbf{y} = \mathbf{C}_u(\mathbf{X}_d, \mathbf{U}_d) \cdot \delta\mathbf{x} + \mathbf{E}_u(\mathbf{X}_d, \mathbf{U}_d) \cdot \delta\mathbf{u} \tag{3.54}$$

where

$$\begin{aligned}
\mathbf{A}_u(\mathbf{X}_d, \mathbf{U}_d) &= \left.\frac{\partial \mathbf{f}(\mathbf{x}, \mathbf{u})}{\partial \mathbf{x}}\right|_{\mathbf{x}=\mathbf{X}_d, \mathbf{u}=\mathbf{U}_d} = \begin{bmatrix} a_{11} & a_{12} & a_{13} & 0 \\ a_{21} & a_{22} & 0 & a_{24} \\ a_{31} & 0 & 0 & a_{34} \\ 0 & a_{42} & a_{43} & 0 \end{bmatrix} \\
\mathbf{B}_u(\mathbf{X}_d, \mathbf{U}_d) &= \left.\frac{\partial \mathbf{f}(\mathbf{x}, \mathbf{u})}{\partial \mathbf{u}}\right|_{\mathbf{x}=\mathbf{X}_d, \mathbf{u}=\mathbf{U}_d} = \begin{bmatrix} b_{11} & b_{12} & b_{13} \\ 0 & 0 & b_{23} \\ 0 & 0 & b_{33} \\ 0 & 0 & b_{43} \end{bmatrix} \\
\mathbf{C}_u(\mathbf{X}_d, \mathbf{U}_d) &= \left.\frac{\partial \mathbf{g}(\mathbf{x}, \mathbf{u})}{\partial \mathbf{x}}\right|_{\mathbf{x}=\mathbf{X}_d, \mathbf{u}=\mathbf{U}_d} = \begin{bmatrix} c_{21} & c_{22} & 0 & 0 \\ c_{31} & c_{32} & 0 & 0 \end{bmatrix} \\
\mathbf{E}_u(\mathbf{X}_d, \mathbf{U}_d) &= \left.\frac{\partial \mathbf{g}(\mathbf{x}, \mathbf{u})}{\partial \mathbf{u}}\right|_{\mathbf{x}=\mathbf{X}_d, \mathbf{u}=\mathbf{U}_d} = \begin{bmatrix} 0 & 0 & e_{23} \\ 0 & 0 & 0 \end{bmatrix}
\end{aligned} \tag{3.55}$$

Through comparison between Eq. 3.37 and Eq. 3.55, it can be seen that the matrices of the system with a voltage source load: $\mathbf{A}_u$, $\mathbf{B}_u$, $\mathbf{C}_u$, $\mathbf{E}_u$, are a part of the matrices of the original system with a capacitive load: $\mathbf{A}_c$, $\mathbf{B}_c$, $\mathbf{C}_c$, $\mathbf{E}_c$, respectively. Their relationship is represented in Eq. 3.37 with the divided dash line. Since each non-zero element in $\mathbf{A}_u$, $\mathbf{B}_u$ and $\mathbf{C}_u$ has the same value as their respective counterpart in $\mathbf{A}_c$, $\mathbf{B}_c$ and $\mathbf{C}_c$, refer to Appendix B for the details.

The resulting small-signal equivalent circuit model of the LCC resonant converter with a voltage source load is shown in Fig. 3.10, which is obviously simpler than that with a capacitive load due to the constant U_o.

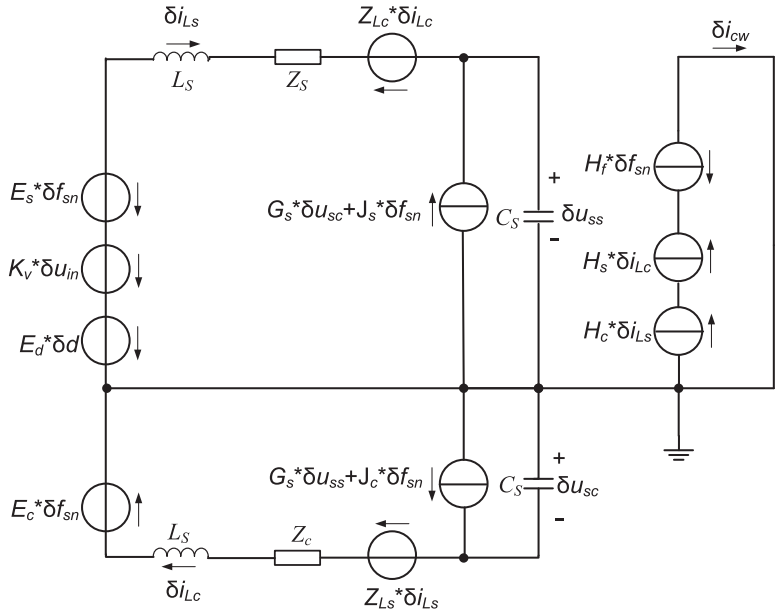

Figure 3.10: Small-signal equivalent circuit model of LCC resonant converter with voltage source load

G. Normalization and Transfer Function

Similar as Section 3.4, normalization is further implemented, the resulting normalized system matrices are denoted as $\mathbf{A}_{un}$, $\mathbf{B}_{un}$, $\mathbf{C}_{un}$ and $\mathbf{E}_{un}$, respectively. The corresponding normalized small-signal model of the LCC resonant converter at the specified operating point ($\mathbf{X}_{dn}$, $\mathbf{U}_{dn}$) is provided below.

$$\delta\dot{\mathbf{x}}_n = \mathbf{A}_{un}(\mathbf{X}_{dn}, \mathbf{U}_{dn}) \cdot \delta\mathbf{x}_n + \mathbf{B}_{un}(\mathbf{X}_{dn}, \mathbf{U}_{dn}) \cdot \delta\mathbf{u}_n \tag{3.56}$$

$$\delta\mathbf{y}_n = \mathbf{C}_{un}(\mathbf{X}_{dn}, \mathbf{U}_{dn}) \cdot \delta\mathbf{x}_n + \mathbf{E}_{un}(\mathbf{X}_{dn}, \mathbf{U}_{dn}) \cdot \delta\mathbf{u}_n \tag{3.57}$$

where

$$\begin{aligned}
\mathbf{A}_{un}(\mathbf{X}_{dn},\mathbf{U}_{dn}) &= \left.\frac{\partial \mathbf{f}(\mathbf{x}_n,\mathbf{u}_n)}{\delta \mathbf{x}_n}\right|_{\mathbf{x}_n=\mathbf{X}_{dn},\mathbf{u}_n=\mathbf{U}_{dn}} = \begin{bmatrix} a_{11n} & a_{12n} & a_{13n} & 0 \\ a_{21n} & a_{22n} & 0 & a_{24n} \\ a_{31n} & 0 & 0 & a_{34n} \\ 0 & a_{42n} & a_{43n} & 0 \end{bmatrix} \\
\mathbf{B}_{un}(\mathbf{X}_{dn},\mathbf{U}_{dn}) &= \left.\frac{\partial \mathbf{f}(\mathbf{x}_n,\mathbf{u}_n)}{\delta \mathbf{u}_n}\right|_{\mathbf{x}_n=\mathbf{X}_{dn},\mathbf{u}_n=\mathbf{U}_{dn}} = \begin{bmatrix} b_{11n} & b_{12n} & b_{13n} \\ 0 & 0 & b_{23n} \\ 0 & 0 & b_{33n} \\ 0 & 0 & b_{43n} \end{bmatrix} \\
\mathbf{C}_{un}(\mathbf{X}_{dn},\mathbf{U}_{dn}) &= \left.\frac{\partial \mathbf{g}(\mathbf{x}_n,\mathbf{u}_n)}{\delta \mathbf{x}_n}\right|_{\mathbf{x}_n=\mathbf{X}_{dn},\mathbf{u}_n=\mathbf{U}_{dn}} = \begin{bmatrix} c_{21n} & c_{22n} & 0 & 0 \\ c_{31n} & c_{32n} & 0 & 0 \end{bmatrix} \\
\mathbf{E}_{un}(\mathbf{X}_{dn},\mathbf{U}_{dn}) &= \left.\frac{\partial \mathbf{g}(\mathbf{x}_n,\mathbf{u}_n)}{\delta \mathbf{u}_n}\right|_{\mathbf{x}_n=\mathbf{X}_{dn},\mathbf{u}_n=\mathbf{U}_{dn}} = \begin{bmatrix} 0 & 0 & e_{23n} \\ 0 & 0 & 0 \end{bmatrix}
\end{aligned} \tag{3.58}$$

Since each non-zero element of them has the same value as their respective counterpart in $\mathbf{A}_{cn}$, $\mathbf{B}_{cn}$ and $\mathbf{C}_{cn}$, refer to Appendix D for the details. The control-to-resonant-current transfer function of the LCC resonant converter with a voltage source load is represented below.

$$\mathbf{G}_{un}(s) = \mathbf{C}_{un} \cdot \left[s_n\mathbf{I} - \mathbf{A}_{un}\right]^{-1} \cdot \mathbf{B}_{un} \tag{3.59}$$

3.6 Comparison of the Small-Signal Models with a Capacitive Load or a Voltage Source Load

In order to further verify the correctness of the simplified modeling with a voltage source load, a comparison between the LCC resonant converters with a capacitive load and a voltage source load is implemented. As shown in Fig. 3.11 - Fig. 3.14, the Bode diagrams of d-to-i_{Lpn} and f_{sn}-to-i_{Lpn} transfer functions of both circuits are provided.

Among which, the blue lines represent the small-signal characteristics of the LCC resonant converter with a capacitive load; while the red lines give the corresponding small-signal characteristics of the LCC resonant converter with a voltage source load. Since the output capacitor's value has effect on the transient characteristics of the transfer functions, various capacitive loads are investigated: Fig.

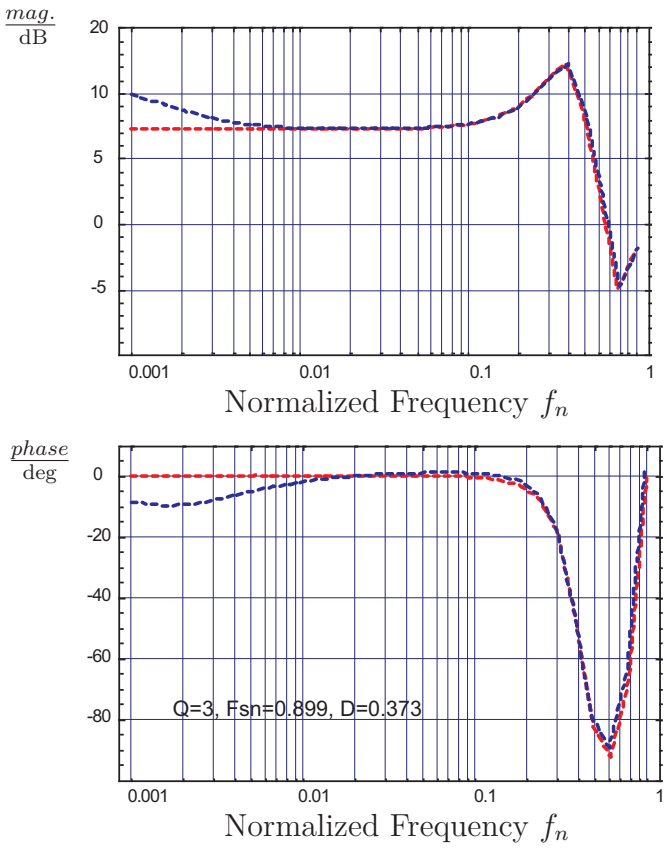

Figure 3.11: Comparison of d-to-i_{Lpn} Transfer functions with capacitive (blue) and voltage source (red) load with LCC resonant converter parameters: C_s=200 nF, C_p=50 nF, L_s=500 μH, R_s=1 Ω, C_L = 10 μF

3.11 and Fig. 3.12 show the results with a relative large capacitive load (10 μF), while Fig. 3.13 and Fig. 3.14 show the results with a relative small capacitive load (10 nF).

From the comparison in Fig. 3.11 and Fig. 3.12, conclusions can be drawn that besides a little magnitude deviation in very low frequency region, the small-signal characteristics of the LCC resonant converter with a voltage source load are almost the same as those of the LCC resonant converter with a large capactive load.

From Fig. 3.13 and Fig. 3.14, it can be seen that when adopting the simplified model to replace a LCC resonant converter model with a small capacitive load, the magnitude deviation between them keeps at a small constant level (about

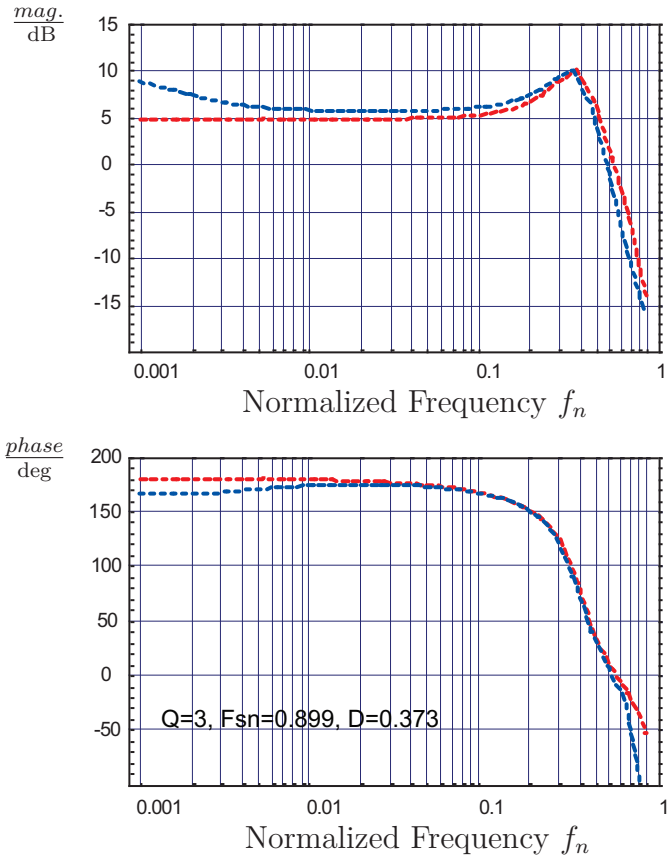

Figure 3.12: Comparison of f_{sn}-to-i_{Lpn} Transfer functions with capacitive (blue) and voltage source (red) loadwith LCC resonant converter parameters: C_s=200 nF, C_p=50 nF, L_s=500 μH, R_s=1 Ω, C_L = 10 μF

$3-5$ dB) in most of the studied frequency region, their phase characteristics are almost the same besides a little deviation in high frequency region.

Since the dynamic deviations between both models are in an acceptable range, the replacement of the original LCC resonant converter model with a capacitive load by the simplified one with an equivalent voltage source load is thought to be reasonable; especially, when the original capacitive load is large.

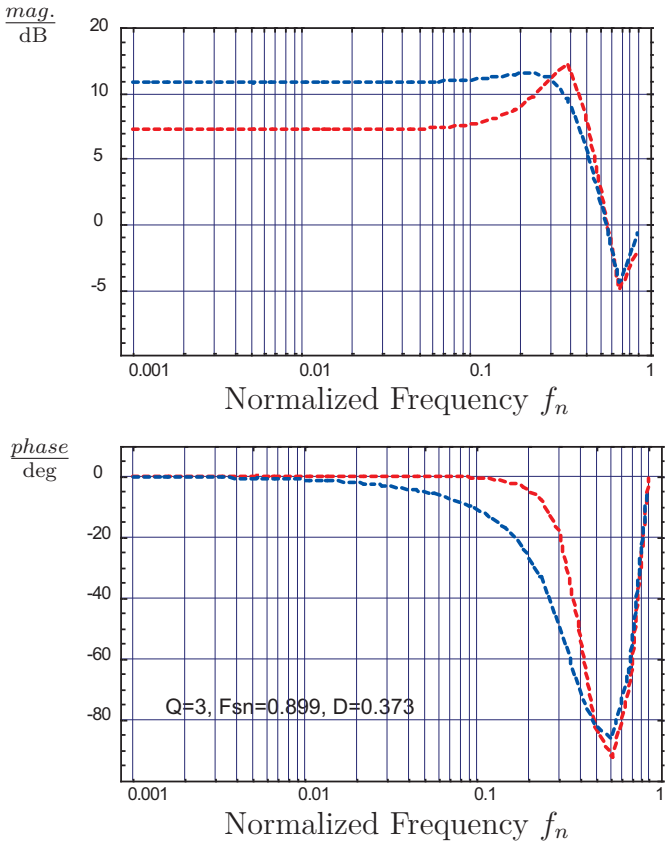

Figure 3.13: Comparison of d-to-i_{Lpn} Transfer functions with capacitive (blue) and voltage source (red) load with LCC resonant converter parameters: C_s=200 nF, C_p=50 nF, L_s=500 μH, R_s=1 Ω, C_L = 10 nF

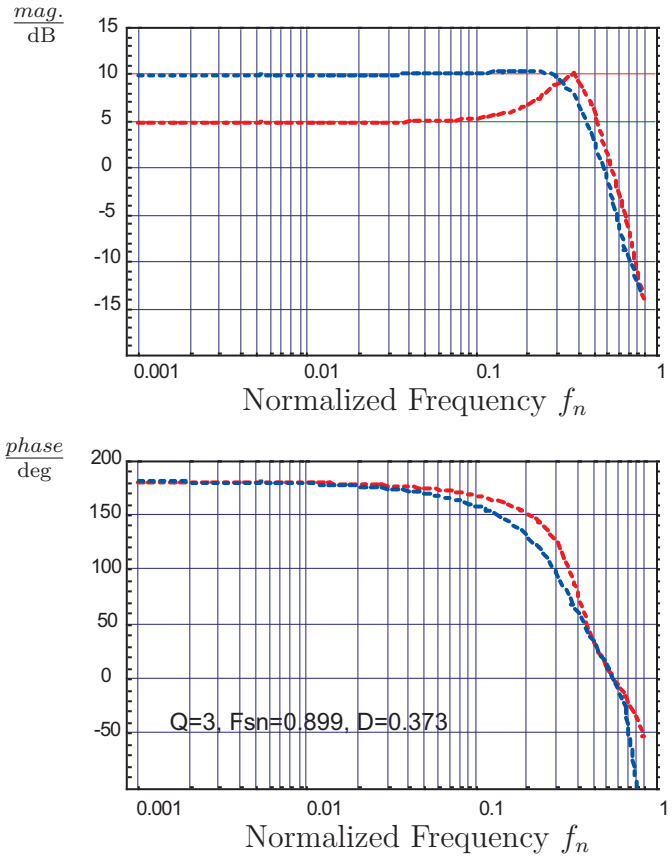

Figure 3.14: Comparison of f_{sn}-to-i_{Lpn} Transfer functions with capacitive (blue) and voltage source (red) load with LCC resonant converter parameters: C_s=200 nF, C_p=50 nF, L_s=500 μH, R_s=1 Ω, C_L = 10 nF

Chapter 4

Model-Based Multi-Objective Optimization for LCC Resonant Converter

4.1 Introduction

The demand of system optimization regarding cost reduction, increased functionality, and limited weight or space (e.g., automative, aircraft) is more and more urgent in power electronic systems nowadays. In 2003, the roadmapping initiative of the European Center of Power Electronics (ECPE) has been started based in a future vision of society in 2020 in order to define the future role of power electronics. In the framework of this initiative a new mathematically supported approach for the roadmapping in power electronics has been developed, which describes the procedure relying on a comprehensive mathematical modeling and subsequent multi-objective optimization of a converter system. The relationship between the technological base and the performance of the system then exists as a mathematical representation, whose optimization assures the best possible exploitation of the available degrees of freedom and technologies [KBW+10].

Based on such concept, a mathematical loss model of the LCC resonant converter system is primarily derived in this Chapter, which taking the full-bridge inverter, the LCC tank, the transformer and the CW multiplier into account. The objectives, i.e. resonant current and voltage drop are subsequently determined. The optimum modulation regarding f_s and d, and the optimal resonant param-

eters' design are also discussed. Finally, a possible optimization procedure, the corresponding simulated results, and the trade-off limit curve (Pareto Front) of a computer aided multi-objective optimization are represented.

4.2 Loss Modeling of LCC Resonant Converter

As aforementioned, the derived large-signal model of the LCC resonant converter considers only the circuit losses from the full-bridge inverter and the LCC tank by adopting a coarsely approximated R_s, the additional losses in the HV-transformer and the voltage drop in the CW multiplier are not taken into account. Investigations show that the predicted output quantities of the VLF high voltage generator based on such large-signal model has an obvious deviation compared with an experimental result because of the neglected losses. Due to such shortage, loss modeling of the LCC resonant converter applied in VLF high voltage generator is necessary and critical for a correct understanding and the estimation of the system steady-state characteristics.

The steady-state model of the LCC resonant converter is the basis for deriving the loss model. By substituting the derivative of each state variable in Eq. 3.22 with zero, the steady-state model can be obtained, Fig. 4.1 represents its equivalent circuit [MRDP+07]. From which, it can be seen that the LCC resonant converter is divided into two parts: the first part represents the behaviour of the LCC resonant tank; while the second part is to describe the characteristics of the output regarding to the transformer primary side. The effects in the resonant tank of the output rectifier, including the parallel capacitor C_p, the CW multiplier and the output load is modeled by a series-connected capacitor C_x and resistor R_x. The voltage across C_x and R_x is u_p. The output part can be regarded as a resistor R_o connecting with a current source i_{cw}, since the output current i_{cw} is approximately constant.

Based on the derived large-signal model, the corresponding variables in Fig. 4.1 can be expressed by the state variables: i_L, u_o and the control variable: ω_s:

$$u_p = (R_x + \frac{1}{j\omega_s C_x}) \cdot i_L, \tag{4.1}$$

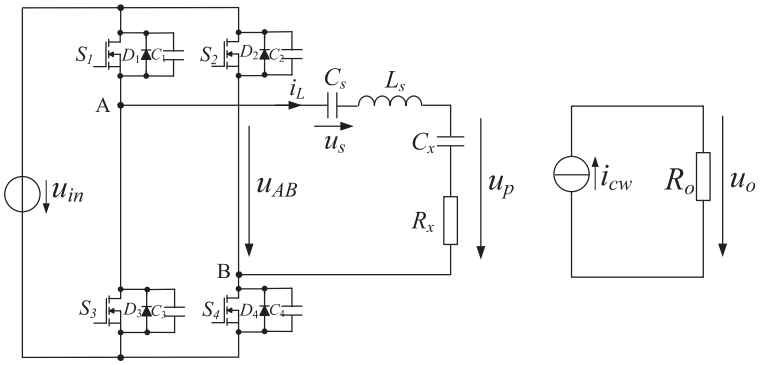

Figure 4.1: Equivalent circuit of LCC resonant converter in steady-state [MRDP+07]

$$i_{cw} = \frac{1 - \cos(\theta)}{2\pi} \cdot i_{Lp}, \tag{4.2}$$

in conjunction with Eq. 3.17 - Eq. 3.19, it is known that

$$R_x = \frac{1}{\pi C_p \omega_s} \cdot \sin^2(\theta), \tag{4.3}$$

$$C_x = \frac{\pi C_p}{\pi - \theta + \frac{1}{2}\sin(2\theta)}, \tag{4.4}$$

$$\theta = \cos^{-1}\left[\frac{C_p \omega_s u_o}{i_{Lp}} - 1\right]. \tag{4.5}$$

From above representations, it can be seen that the resonant current i_L or its amplitude i_{Lp} is an important intermediate variable, which reflects the component stress and the losses of the full-bridge inverter, LCC resonant tank and HV-transformer. The details of the loss model for each part are depicted below, respectively.

4.2.1 Loss Model of Full-Bridge Inverter with MOSFETs

Based on Fig. 4.1, the losses of the full-bridge inverter consisting of MOSFETs under ZVS operation condition with optimum switching line [MRDP+07] are approximated, which includes the conduction losses and switching losses of MOSFETs, and the conduction losses of the anti-parallel diodes [BBK09]:

$$P_{FB} = 4 \cdot R_{DSon} \cdot I_{Mrms}^2 + 2 \cdot P_{SW} + 4\left(V_F \cdot I_{Davg} + R_D \cdot I_{Drms}^2\right), \tag{4.6}$$

where I_{Mrms} is the effective current of MOSFET, R_{DSon} is the drain-source on-state resistance of MOSFET; I_{Davg} and I_{Drms} are the anti-parallel diode average current and effective current, respectively; V_F is the diode forward voltage; R_D is the diode on-state resistance; and P_{SW} represents the MOSFET switching losses. Their calculations are expressed below, among which, t_{ru} and t_{fi} are rising and falling time during the switch-off transient, respectively. I_{Moff} is the turn-off MOSFET current.

$$I_{Mrms} = \sqrt{\frac{1}{T_s} \int_{0}^{\frac{DT_s}{2}} [I_{Lp} \cdot \sin(\omega_s t)]^2 \cdot dt} \tag{4.7}$$

$$I_{Davg} = \frac{1}{T_s} \int_{\frac{DT_s}{2}}^{\frac{T_s}{2}} I_{Lp} \cdot \sin(\omega_s t) \cdot dt \tag{4.8}$$

$$I_{Drms} = \sqrt{\frac{1}{T_s} \int_{\frac{DT_s}{2}}^{\frac{T_s}{2}} [I_{Lp} \cdot \sin(\omega_s t)]^2 \cdot dt} \tag{4.9}$$

$$P_{SW} = U_{in} \cdot I_{Moff} \cdot \frac{t_{ru} + t_{fi}}{2} \cdot f_s \leq U_{in} \cdot I_{Lp} \cdot \frac{t_{ru} + t_{fi}}{2} \cdot f_s \tag{4.10}$$

Since P_{SW} can be neglected if I_{Moff} is small [BBK09], it can be said that: Besides the transistor parameters, the resonant current amplitude i_{Lp} determines the power losses of the full-bridge inverter.

4.2.2 Losses of Series Capacitor

The losses of the series capacitor C_s is approximated below, where $\tan\delta$ is the capacitor losses factor.

$$P_{Cs} = \left(\frac{{U_{ss}}^2 + {U_{sc}}^2}{2} \right) \cdot \omega_s \cdot C_s \cdot \tan\delta = \frac{{I_{Lp}}^2 \cdot \tan\delta}{\omega_s \cdot C_s} \tag{4.11}$$

From Eq. 4.11, it can be concluded that the resonant current amplitude i_{Lp} is predominant to determine the losses of C_s.

4.2.3 Losses of Magnetic Components

The losses of magnetic components, such as the series inductor L_s and the HV-transformer, are considered according to [EM00], which includes not only the core losses P_{fe} and the low-frequency copper winding losses P_{cu}, but also the power losses in winding conductors due to eddy currents. They are briefly depicted below, respectively.

A. Core Losses P_{fe}

The core losses of the magnetic components P_{fe} [EM00] is

$$P_{fe} = K_{fe0} \cdot f_s^{\xi} \cdot (\Delta B)^{\beta} \cdot A_c \cdot l_m \tag{4.12}$$

where K_{fe0}, ξ and β are the core loss coefficients depending on the specified core material and can be obtained from datasheet (see Table. 4.1 for an example); f_s is the converter switching frequency with unit kHz; ΔB is the peak AC flux density with unit Tesla; A_c is the core cross-sectional area with unit cm^2; lm is the core mean magnetic path length with unit cm; obviously, $A_c \cdot l_m$ is the volume of the core.

Core Material	K_{fe0} ($W/cm^3T^{\beta}(kHz)^{\xi}$)	ξ	β	Loss (mW/cm^3) @ Temperature (°C) (typical condition: 100 kHz, 0.1 Tesla)
K core material f_s <500kHz	0.0375	1.60	3.15	- - -
R core material f_s <100kHz	0.1045	1.43	2.85	140@25, 100@60, 70@100
P core material f_s <100kHz	0.2181	1.36	2.86	125@25, 80@80, 125@100
F core material 10kHz≤ f_s ≤500kHz	0.1569	1.72	2.66	100@25, 180@60, 225@100

Table 4.1: Manufacturing datasheet for various core materials (MAGNETICS)

Table. 4.1 also shows the measured core losses of R, P and F core materials at specified conditions, respectively. Considering the VLF high voltage generator application, the temperature of cooling oil tank is up to 80 °C, which implies the highest temperature of the high-voltage transformer and CW-multiplier is up to

80 °C. According to Table. 4.1, P and R core materials are more appropriate for such applications.

B. Low-Frequency Copper Loss P_{cu}

According to [EM00], the transformer low-frequency copper loss P_{cu} is

$$P_{cu} = \frac{\rho \cdot \lambda_1^2 \cdot {I_{tot}}^2 \cdot MLT}{4 \cdot K_u \cdot W_A \cdot {A_c}^2 \cdot \Delta B^2} \tag{4.13}$$

where ρ is the wire effective resistivity; λ_1 is the applied primary volt-seconds; I_{tot} is the total rms winding current referred to the primary; MLT is the mean length per turn; K_u is the winding fill factor, typical values of K_u for cores with winding bobbins are: 0.5 for a simple low-voltage inductor, 0.05 to 0.2 for a high-voltage transformer supplying several kV; W_A is the core window area, A_c is the core cross-sectional area. According to Fig. 3.2 and Fig. 4.1, λ_1 can be expressed as Eq. 4.14, and I_{tot} can be depicted with resonant current amplitude i_{Lp}.

$$\lambda_1 = \int_0^{\frac{T_s}{2}} u_p \cdot dt = \int_0^{\frac{T_s}{2}} (R_x + \frac{1}{\omega_s C_x}) \cdot I_{Lp} \cdot \sin(\omega_s t) \cdot dt \tag{4.14}$$

$$I_{tot} = \sqrt{2} \cdot I_{Lp} \tag{4.15}$$

As an example, Fig. 4.2 gives a typical diagram of P_{fe}, P_{cu} and their sum P_{tot} with specified core geometry and core material of a transformer applied in a LCC resonant converter. It shows that it is possible to minimize P_{fe}, P_{cu} and their sum P_{tot} of a magnetic component by choosing preferable core geometry, core material or operating point.

C. Eddy Current Effect

In high-current conductors of multi-layer windings, particularly in high-frequency converters, the skin effect and the proximity effect resulting from the conductor eddy currents are most pronounced and lead to significant copper losses. Considering eddy current effects, an optimized winding design can be employed to realize the minimal total copper loss.

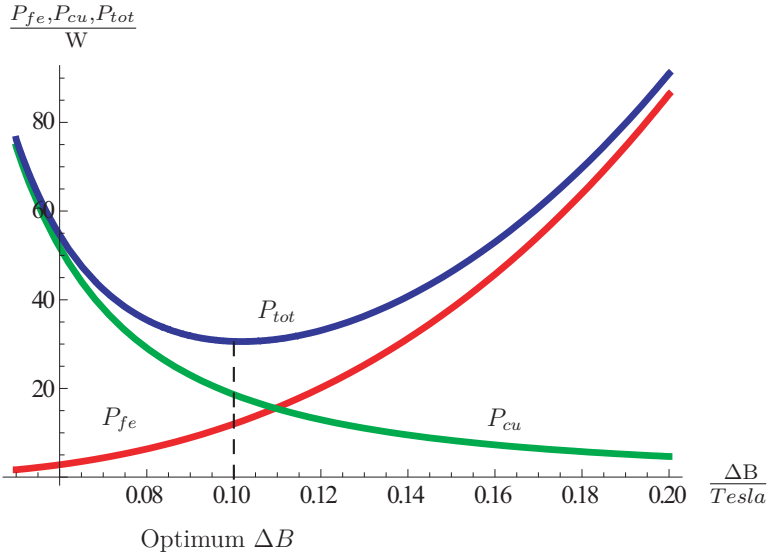

Figure 4.2: P_{fe}, P_{cu} and their sum P_{tot} with 8*EE70/68/19 and R material

According to [EM00], the proximity effect increases the copper loss in each layer by the factor:

$$\frac{P}{P_{dc}} = \varphi(2m^2 - 2m + 1)G_1(\varphi) - 4m(m-1)G_2(\varphi), \tag{4.16}$$

where the functions $G_1(\varphi)$ and $G_2(\varphi)$ are

$$G_1(\varphi) = \frac{\sinh(2\varphi) + \sin(2\varphi)}{\cosh(2\varphi) - \cos(2\varphi)}, \tag{4.17}$$

$$G_2(\varphi) = \frac{\sinh(\varphi)\cos(\varphi) + \cosh(\varphi)\sin(\varphi)}{\cosh(2\varphi) - \cos(2\varphi)}. \tag{4.18}$$

Among which, factor φ is the ratio of a foil conductor layer width h to its skin depth δ', MMF ratio m is the ratio of the magnetomotive force $F(h)$ to the layer ampere-turns $N_p I_{rms}$. Refer to Appendix E for more details.

Considering a conventional transformer, the proximity effect increases the copper loss in L layers primary windings by the factor:

$$F_R = \frac{P_{pri}}{P_{pri,dc}} = \frac{1}{L}\sum_{m=1}^{L} \varphi[(2m^2 - 2m + 1)G_1(\varphi) - 4m(m-1)G_2(\varphi)]. \tag{4.19}$$

where

$$\sum_{m=1}^{L} m = \frac{L(L+1)}{2}, \tag{4.20}$$

$$\sum_{m=1}^{L} m^2 = \frac{L(L+1)(2L+1)}{6}. \tag{4.21}$$

In conjunction with Eq. 4.17, Eq. 4.18, Eq. 4.20 and Eq. 4.21, Eq. 4.19 can be rewritten as:

$$F_R = \frac{P_{pri}}{P_{pri,dc}} = \varphi \left[\frac{\sinh(2\varphi) + \sin(2\varphi)}{\cosh(2\varphi) - \cos(2\varphi)} + \frac{2(L^2-1)}{3} \frac{\sinh(\varphi) - \sin(\varphi)}{\cosh(\varphi) + \cos(\varphi)} \right] \tag{4.22}$$

Since the trigonometric and hyperbolic functions may be approximated by the series expansions [HGB00]:

$$\frac{\sinh(2\varphi) + \sin(2\varphi)}{\cosh(2\varphi) - \cos(2\varphi)} \approx \frac{1}{\varphi} + \frac{4}{45}\varphi^3, \tag{4.23}$$

$$\frac{\sinh(\varphi) - \sin(\varphi)}{\cosh(\varphi) + \cos(\varphi)} \approx \frac{1}{6}\varphi^3, \tag{4.24}$$

Eq. 4.22 can be further approximated as:

$$F_R \approx 1 + \frac{(5L^2-1)}{45}\varphi^4. \tag{4.25}$$

Refer to [HGB00], under sinusoidal excitation, the minimal total copper loss can be obtained with φ_{opt} at given L layers. Among which,

$$\varphi_{opt} \approx \sqrt[4]{\frac{15}{5L^2-1}} \tag{4.26}$$

The increase factor F_R with φ_{opt} is

$$F_R(\varphi_{opt}) \approx 1 + \frac{(5L^2-1)}{45}(\varphi_{opt})^4 = \frac{4}{3} \tag{4.27}$$

The optimal thickness h_{opt} of the square conductors is derived based on φ_{opt} and δ. As an example, assuming the switching frequency remains 50 kHz, the skin depth δ in copper at this frequency is 0.295 mm, when the length of the foil $N_p h$ does not stretch (Fig. E.1(c)), the corresponding optimal layer or foil thickness h_{opt} can be calculated, as shown in Eq. 4.28 and Table 4.2. When the length of the foil $N_p h$ stretches to the width of the core window l_w (Fig. E.1(d)), the corresponding optimal layer or foil thickness h_{opt} is expressed in Eq. 4.29.

$$h_{opt} = \delta \cdot \varphi_{opt} = 0.295\varphi_{opt} \approx 0.295\sqrt[4]{\frac{15}{5L^2-1}} \tag{4.28}$$

L	1	2	3	4	5	6	7	8	9	10
φ_{opt}	1.392	0.943	0.764	0.660	0.590	0.538	0.498	0.466	0.439	0.416
$h_{opt}(mm)$	0.411	0.278	0.225	0.195	0.174	0.159	0.147	0.137	0.129	0.123

Table 4.2: Optimal layer or foil thickness, as a function of L with 50 kHz sinusoidal excitation

$$h_{opt} = \delta' \cdot \varphi_{opt} = \frac{\delta \cdot \varphi_{opt}}{\sqrt{\eta}} = \sqrt[3]{\frac{(\varphi_{opt})^2 \delta^2 l_w}{N_p}} \tag{4.29}$$

From Eq. 4.28, Eq. 4.29 and the determined core geometry, an optimal layer or foil conductor thickness for the transformer primary windings can be selected to get the minimal total copper loss. The analog method can be adopted for the secondary windings design.

4.2.4 Voltage Drop of Cockcroft-Walton (CW) Multiplier

As aforementioned, the voltage drop of a CW multiplier is mainly resulting from the capacitors' charge and discharge process. The derived equations of a symmetrical k-stage CW multiplier voltage drop ΔU_{cwk} is already provided in Chapter 2.3.

When considering the total losses of the VLF high voltage generator, the CW multiplier cannot be regarded as a separate part again. As a high voltage part, it is built in an isolated oil cage, the stray capacitors' effect between the components of the CW multiplier and the isolated cage shell is inevitable, which results additional voltage drop [Bal59]. An additional factor F is introduced to approximate the increasing voltage drop. Since it is difficult to individually measure those stray capacitors due to the knowledge shortage in the fields of high voltage measurement and magnetic field interference, all the stray capacitors are assumed having the same value C_q, which depends on the CW multiplier capacitance C and an experience value b [Bal59]. The relationship between C_q, C and b is represented in Eq. 4.30, the corresponding F is approximated in Eq. 4.31 [Bal59].

$$C_q = \frac{C}{b^2} \tag{4.30}$$

$$F = \frac{b \cdot \left[1 - e^{\frac{-4k}{b}}\right]}{2k \cdot \left[1 + e^{\frac{-4k}{b}}\right]} \leq 1 \tag{4.31}$$

With consideration of the stray capacitors, the real CW multiplier output voltage U_{cwk} is derived as follows

$$U_{cwk} = F \cdot (2nkU_p - \Delta U_{cwk}) \tag{4.32}$$

Table 4.3 gives some F values regarding usual stage number k and experience value b [Bal59].

k	b	F
3	11	0.911
4	11	0.854
5	11	0.793

Table 4.3: Estimated F regarding specified stage number k and experience value b

Table 4.4 provides the experimental results of a four-stage CW multiplier. In which, the CW multiplier output current I_{cw} and input voltage nU_{tp} are specified; $U_{cwk\_measure}$ is the measured actual CW multiplier output voltage, while $U_{cwk\_predict}$ is the calculated output voltage with consideration of ΔU_{cwk} and F; *error* denotes the percentage deviation between $U_{cwk\_predict}$ and $U_{cwk\_measure}$. The approximated F value of a four-stage CW multiplier in Table 4.3 is adopted for calculating $U_{cwk\_predict}$. From Table 4.4, it can be seen that the predicted $U_{cwk\_predict}$ agrees with the measured $U_{cwk\_measure}$ in an acceptable tolerance range. Such results further verify the rationality of the approximated F based on the experience value b.

Since F can be estimated in an acceptable tolerance region, the CW multiplier voltage drop ΔU_{cwk} is thought to be an important factor for the converter optimization.

4.2.5 Multi-Objective Selection

From above analysis, conclusions can be drawn from the following two aspects: First, the resonant current amplitude i_{Lp} is an important intermediate variable,

nU_{tp} (kV)	I_{cw} (mA)	$2nkU_{tp} - \Delta U_{cwk}$ (kV)	F	$U_{cwk\_predict}$ (kV)	$U_{cwk\_measure}$ (kV)	error (%)
1.475	1	11.53		9.85	10	1.50
2.721	1	21.50	0.854	18.261	20	8.20
4.069	1	32.28		27.57	30	8.10
5.341	1	42.46		36.26	40	9.35
2.190	25	10.77		9.20	10	8.00
3.710	25	22.93	0.854	19.58	20	2.10
5.210	25	34.93		29.83	30	0.57
6.710	25	46.93		40.08	40	-0.20

Table 4.4: Estimated and measured four-stage CW multiplier output voltage with consideration of stray capacitor's effect

which determines the component stress of the full-bridge inverter, the LCC tank and the HV-transformer; further, i_{Lp} directly indicates the power losses of the resonant converter, since the losses caused by transistors, series capacitor C_s and magnetic components (L_s, transformer) have either proportional or exponential relationship with i_{Lp}. Hence, through the investigation and observation of i_{Lp}, the component stress and power losses of the LCC resonant converter can be obtained and supervised. From the other aspect, the voltage drop of a k-stage CW multiplier ΔU_{cwk} determines most of the deviation between the investment and the earnings, i.e. utilisation rate. Such voltage drop has a great influence on the expected output voltage, and directly indicates the useless wasteful cost.

In a summary, the resonant current amplitude i_{Lp} and the voltage drop from the CW multiplier ΔU_{cwk} are selected as the two objectives for the LCC converter multi-objective optimization.

It should be noted that besides the component stress, power losses and voltage drop, the total converter volume is also an important factor for an optimal design. But since the HV-transformer and CW multiplier in real VLF high voltage generator are usually housed in an oil tank, the actual volume is not only the volume sum of all the components, the tank volume and the additional insulation space must also be taken into account. The resulting total volume would be much larger than the volume sum of the components, especially in very high voltage applications. An accurate volume calculation needs the special knowledge

and experience in the fields of high voltage technique, magnetics, and prototype building. This is beyond the region of this dessertation.

4.3 Optimization with Optimum f_s-d Combination and Parameters Selection

The optimum modulation regarding f_s-d combination and the appropriate LCC tank parameters (C_s, C_p) design are briefly discussed below.

4.3.1 Optimum f_s-d Combination

Plenty of f_s and d combinations can realize the same output voltage U_o and output power P_o under specified output load Q. Among which, there exists an optimum f_s-d combination, which can realize the expected U_o and P_o under specified Q with minimal reactive power resulting from the LCC resonant tank.

The converter operates with an optimum f_s-d combination is defined as such condition that the phase angle φ_2 between $u_{AB}(t)$ and $i_L(t)$ is larger than zero but very close to zero (Refer to Fig. 3.2 for the definition of φ_2) [MRDP+07]: φ_2 is greater than zero, which ensures the converter operating under ZVS with minimized switching losses; φ_2 is very close to zero, which ensures the minimal reactive power generating by the LCC resonant tank. Under optimum f_s-d combination, the overall losses should be minimized and overall efficiency will be maximized.

Under optimum f_s-d combination condition, the duty cycle d depends on the Fourier coefficients of the resonant current, and can be calculated according to instantaneous switching frequency f_s and normalized output load Q:

$$d_{\varphi 2>0\&\varphi 2\to 0} = 1 - \frac{2}{\pi}\arctan(-\frac{I_{Lc}}{I_{Ls}}) \propto f(f_s, Q) \tag{4.33}$$

4.3.2 Resonant Parameters Design

The resonant parameters are series capacitor C_s, parallel capacitor C_p and series inductor L_s in the LCC tank. Investigations show that an expected LCC resonant

converter output quantity can be achieved with minimal component stress and minimal power losses through an optimized resonant parameters' selection.

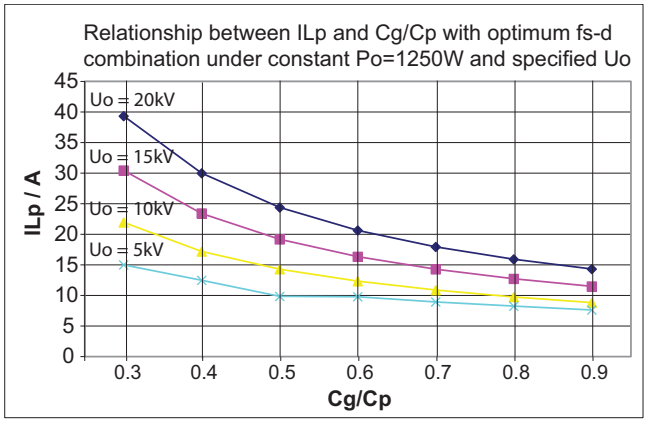

(a)

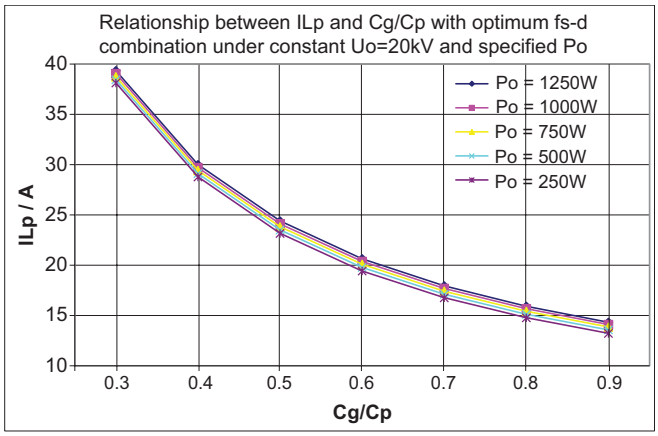

(b)

Figure 4.3: Relationship between i_{Lp} and C_g/C_p with optimum f_s-d combination under constant P_o and specified U_o (a) or under constant U_o and specified P_o (b)

As an example, Fig. 4.3(a) shows the relationship between I_{Lp} and the resonant capacitance ratio C_g/C_p with the same output power P_o and various output voltage U_o, while Fig. 4.3(b) shows the relationship between I_{Lp} and C_g/C_p with the same U_o and various P_o under the optimum f_s-d combination. Among which, C_g is defined as follows

$$C_g = \frac{C_s C_p}{C_s + C_p} \tag{4.34}$$

From Fig. 4.3, it can be concluded that larger C_g/C_p results in lower component stress I_{Lp} with the same output quantities. In practice, the value of C_g/C_p between 0.5 and 0.8 is preferable [MRDP+07].

4.4 Multi-Objective Optimization of LCC Resonant Converter

Optimization can be defined as the science of determining the "best" solutions to certain mathematically defined problems. If an optimization problem involves only one objective function, it is termed single-objective optimization. Since most engineering problems are required to optimize a number of conflicting objectives, they are also referred to as multi-criteria or vector optimization problems. It can be formulated by the following: Find a decision variable $\mathbf{x} = (x_1, x_2, \ldots, x_m)^T$, that satisfies the given constraints Ω and optimizes a vector function $\mathbf{f}(\mathbf{x}) = (\mathbf{f}_1(\mathbf{x}), \ldots, \mathbf{f}_m(\mathbf{x}))^T$, whose components are objective functions, as stated below:

minimize $\mathbf{f}(\mathbf{x}) = [\mathbf{f}_1(x_1, \ldots, x_m), \mathbf{f}_2(x_1, \ldots, x_m), \ldots, \mathbf{f}_l(x_1, \ldots, x_m)]^T$

subject to $\mathbf{x} \in \Omega$

where $\mathbf{f} : \Re^m \rightarrow \Re^l$ and $\Omega \subset \Re^m$

A point $\mathbf{x}^* \in \Omega$ is a Pareto minimizer, or a non-dominated solution, if there exists no other feasible decision variable $\mathbf{x}$ that would decrease some objectives without causing simultaneous increase at least of one other objective [Ce08].

For multi-objective optimization of the LCC resonant converter, the so-called Pareto solution is defined as: there exists no other feasible decision variable $\mathbf{x} = (C_s, C_p, L_s, f_s, n, k)^T$, that would decrease one component of objective vector $\mathbf{f}(\mathbf{x}) = (I_{Lp}(x), \Delta U_{cwk}(x))^T$ without increasing the other component at the same time.

In order to reduce the optimization complexity, the core material and geometry of transformer and inductor are preliminarily fixed and implemented in an inner optimization loop with the compromise of acceptable volume and losses. The optimal layer or foil thickness h_{opt} according to Table 4.2, Eq. 4.28, Eq. 4.29 is adopted in the inner optimization loop. The transformer turns ratio n is set to 7, which are kept constant during the outer loop optimization.

The outer loop optimization procedure of the LCC resonant converter regarding the two objectives is shown in Fig. 4.4. The design specifications of VLF high voltage generator, such as the input and output quantities (U_{in}, U_o, I_o, P_o) are provided from the customer. The operating point with maximal output power is studied and selected for the optimization due to its importance in practice. As an example, the corresponding specifications of a scaled-down VLF high voltage generator are provided in Table 4.5.

Input voltage	360 V
Maximal output voltage	10 kV
Maximal output power	200 W
Maximal output current	40 mA
Selected operating point: P_{o_max}	Input voltage 360 V Output power 200 W Output voltage 7.07 kV Output current 28.3 mA

Table 4.5: Specifications of a scaled-down VLF HV generator

From Fig. 4.4, the optimization procedure is depicted: under provided specifications of the VLF high voltage generator, a set of start value of the decision variables (C_s, C_p, L_s, f_s, k) are initially coarsely given. Those decision variables are imported into the LCC resonant converter large-signal model, the corresponding lossless electrical quantities can be primarily calculated, such as resonant current i_L, transformer primary voltage u_p, CW multiplier diode conduction angle θ_{ss}, optimum duty cycle d and ideal output voltage. Some of them are further inputted into the loss model of the full-bridge inverter, magnetic components and CW multiplier for deriving the corresponding losses and voltage drop. Combining above calculation results, the actual output quantities under provided specifications and given decision variables' start values can be obtained. Comparing the actual calculation results with the expected output quantities (U_o, P_o, R_o), if both of them agree, then this set of decision variable's value $(C_s, C_p, L_s, f_s, k)^T$ and the corresponding objective vector $(i_{Lp}(x), \Delta U_{cwk}(x))^T$ will be recorded; otherwise, a modification of the value of decision variables will be executed, and above calculation process is repeated [HFB11].

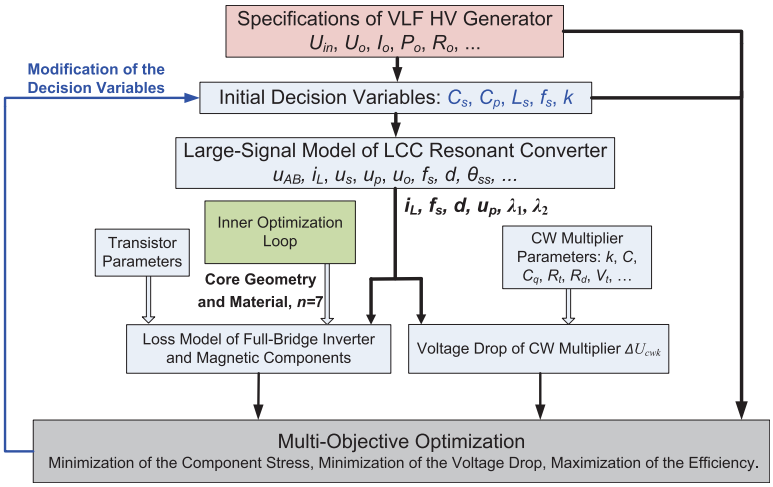

Figure 4.4: Multi-objective optimization procedure of LCC resonant converter

Based on above model-based calculation, plenty of objective vectors $(I_{Lp}, \Delta U_{cwk})^T$ with feasible decision variable $(C_s, C_p, L_s, f_s, k)^T$ for the same operating point (such as P_{o_max}) are obtained. The multi-objective optimization with minimal component stress and maximal efficiency can then be derived.

In cooperation with iXtronics, above multi-objective optimization process was implemented in a computer aided design and optimization (CAD-CAO) environment: CAMeL-View-MOPO. Under given specifications and provided decision variable's modulation range, the multi-objective optimization procedure of a LCC resonant converter can be automatically executed for an expected operating point, the corresponding objective factor $(I_{Lp}, \Delta U_{cwk})^T$ and the decision variable $(C_s, C_p, L_s, f_s, k)^T$ at the satisfying operating point are automatically recorded and marked, as shown by each separate point in Fig. 4.6 - Fig. 4.8. The CAD-CAO project structure, simulation window and the multi-objective optimization window in CAMeL-View-MOPO environment are briefly shown in Fig. 4.5.

Based on such model-based computer aided design and optimization environment, the graphical results about the interested relationship between decision variables $(C_s, C_p, L_s, f_s, k)^T$ and I_{Lp}, and the two dimensional illustration about the objective vector $(I_{Lp}, \Delta U_{cwk})^T$ at the operating point with maximal output power are obtained, as shown in Fig. 4.6 and Fig. 4.7.

Fig. 4.6 represents the relationship between f_s and I_{Lp} with decision variables'

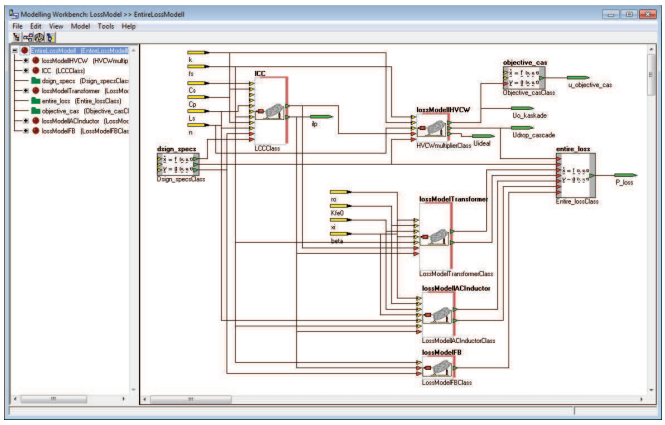

(a) CAD-CAO Project structure

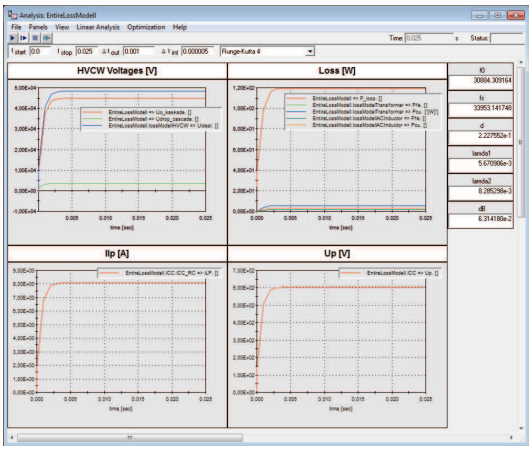

(b) Simulation window

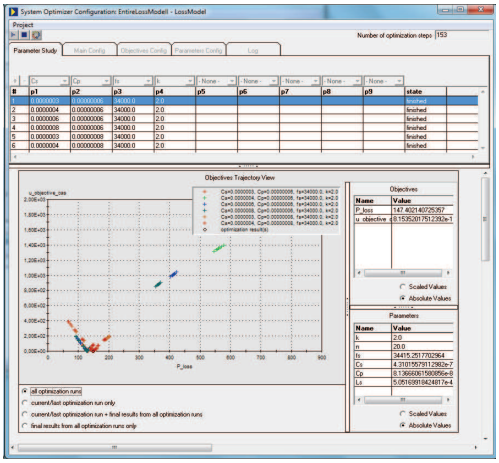

(c) Multi-objective optimization window

Figure 4.5: Model-based CAD and CAO environment: CAMeL-View-MOPO

range: $C_s = 100 - 400$ nF, $C_p = 10 - 200$ nF, $L_s = 100 - 1000$ μH, $n = 7$, $k = 2$. The other samples with k =3, 4 have also been calculated, but since those results are not optimal compared to those with k =2, they are not shown here. Fig. 4.7 provides a two dimensional illustration about I_{Lp}-ΔU_{cwk} relationship regarding the same decision variables' range.

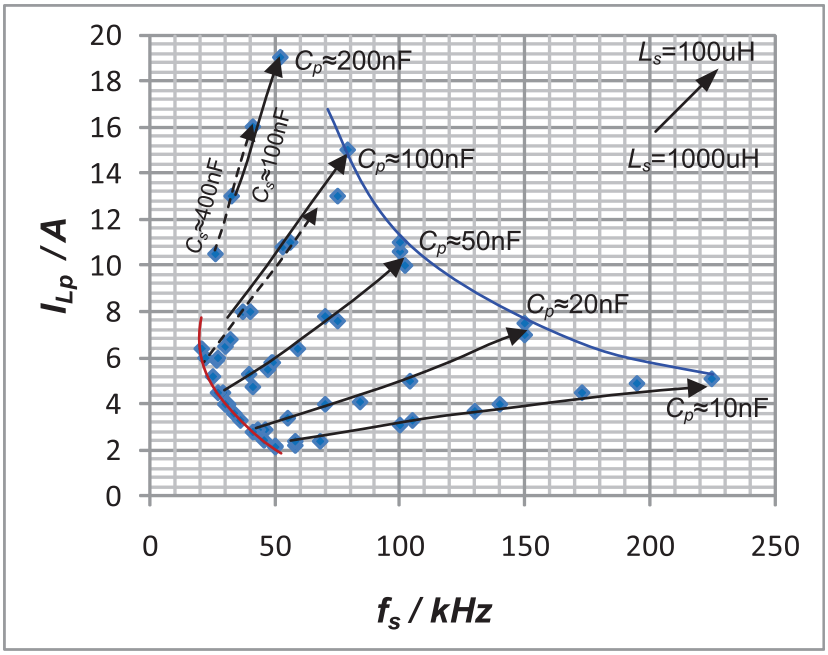

Figure 4.6: Graphical results of the relationship between f_s and i_{Lp} with decision variables' range: $C_s = 100 - 400$ nF, $C_p = 10 - 200$ nF, $L_s = 100 - 1000$ μH, $n = 7$, $k = 2$

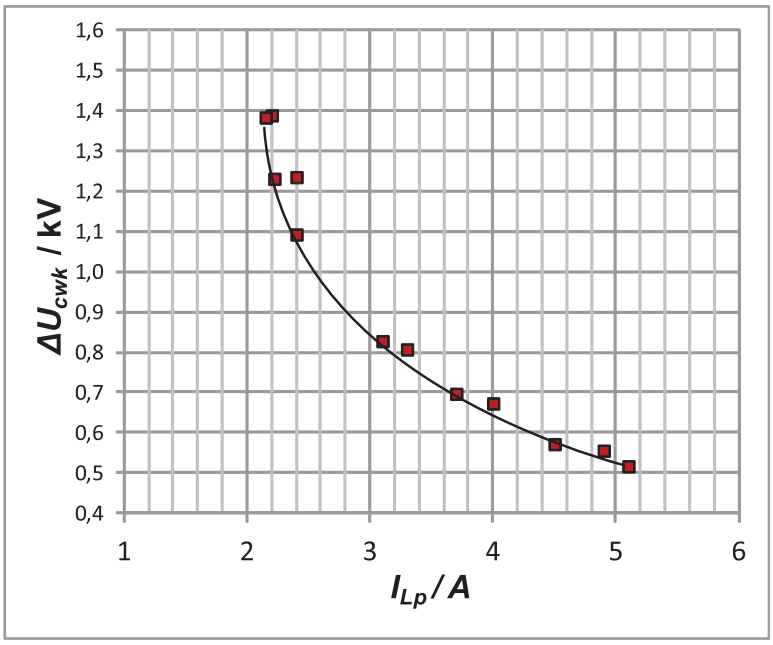

Figure 4.8: Pareto front of i_{Lp} and ΔU_{cwk} with minimal $C_p = 10$ nF

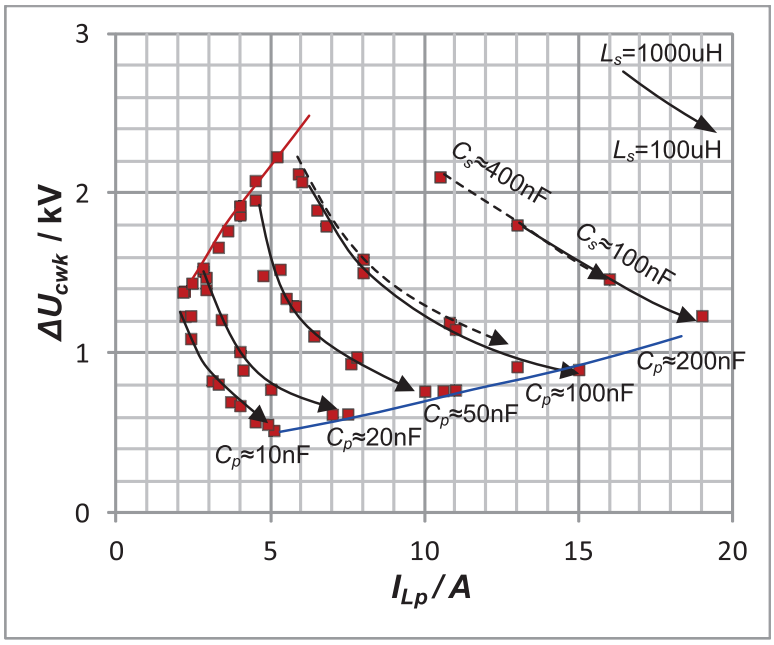

Figure 4.7: Two dimensional illustration for objectives: i_{Lp} and ΔU_{cwk} in decision variables' range: $C_s = 100 - 400$ nF, $C_p = 10 - 200$ nF, $L_s = 100 - 1000$ μH, $n = 7$, $k = 2$

From Fig. 4.6 and Fig. 4.7, it can be seen that there exists rules of the f_s-I_{Lp} relationship and the I_{Lp}-ΔU_{cwk} relationship regarding various decision variables. They are summarized as follows:

1. Along with the arrow direction of each black solid line, the L_s value varies from 1000 μH to 100 μH with the specified same C_p value and 100 nF C_s value. The red line and blue line marks the boundary of the maximal and minimal L_s value, respectively. With such decision variables, I_{Lp} has nearly a positive proportional relationship with f_s, the slope depends on the corresponding C_p value (refer to Fig. 4.6); while ΔU_{cwk} has an inverse variational relationship with I_{Lp} (refer to Fig. 4.7).

2. Further investigations show that various C_s value has almost no influence on the f_s-I_{Lp} or the I_{Lp}-ΔU_{cwk} relationship, if the value of C_p is less than about 50 nF; but has a translational effect with large C_p value. As shown in the figures, the black dashed lines demonstrate the translational effect with

400 nF C_s value regarding those with 100 nF C_s value, the corresponding large C_p values is 100 nF or 200 nF.

3. It is obvious that larger C_s/C_p ratio results in smaller I_{Lp}. If the C_p value is about 10 nF, the minimal I_{Lp} is obtained near $f_s = 50$ kHz (refer to Fig. 4.6).

4. Since ΔU_{cwk} has an inverse variational relationship with I_{Lp}, the trade-off limit curve, i.e. Pareto Front based on non-dominated solutions, can be obtained with each specified C_p value.

Based on Fig. 4.7, as an example, when the C_p value is about 10 nF, the corresponding Pareto front regarding I_{Lp} and ΔU_{cwk} can be obtained, as represented in Fig. 4.8. The point on the Pareto front is the so-called non-dominated solution, that is to say, there exists no feasible decision variable: $(C_s, C_p, L_s, f_s, k)^T$, that would decrease I_{Lp} without increasing ΔU_{cwk} at the same time, or vice versa. The Pareto front with the other C_p value can also be derived based on Fig. 4.7.

4.5 Summary

Based on the derived large-signal model and the loss model, and considering the optimum f_s-d modulation and optimal resonant parameters' design, a multi-objective optimization of a LCC resonant converter applied in the VLF high voltage generator is presented in this Chapter. The resonant current amplitude I_{Lp} and the voltage drop in a k-stage symmetrical CW multiplier ΔU_{cwk} are selected as the objectives, since they are critical intermediate variables to determine the component stress, reflect the power losses and the unutilized expenditure of the resonant converter system. With the help of a computer aided design and optimization environment, an automatic model-based simulation and multi-objective optimization is implemented. The graphical results about the relationship between decision variables and objectives, and the two dimensional illustration of the objectives are represented. A Pareto front based on non-dominant solutions is derived under the constraints of decision variables.

Such research and optimization results provide a graphical guideline for optimal design and multi-objective optimization of the LCC resonant converter

applied in VLF high voltage generator. The developed model-based computer aided design and optimization environment can be conveniently utilized in practical implementation and is beneficial for industry.

Chapter 5

Conventional Linear Control Design

5.1 Introduction

Model-based controller can be developed based on the derived small-signal model in Chapter 3. As well known, the conventional linear control schemes are still the most widely adopted method in industry for various control applications, due to their simple structure, ease of design, and low cost in implementation. In this Chapter, the conventional proportional-integral (PI) controller is primarily considered and designed for the LCC resonant converter applied in VLF high voltage generator.

In order to ensure the control performance of the closed loop, a cascaded two-loop control strategy is decided, which comprises the inner current-mode control and the outer voltage control. Both of them adopt the conventional linear control scheme. The output current i_{cw} is selected as the control object for the inner control loop, while the output voltage u_o is selected as the control object of the outer control loop. Since the inner current-mode control represents the more complex task and is the emphasis of the control design, it is treated below.

5.2 Dynamics Analysis and Reduced-Order Transfer Functions

Based on the small-signal model (Fig. 3.5), the typical control-to-output-current transfer functions at given operating point can be obtained, as shown in Eq. 5.2 and Eq. 5.3 [HFB09b] [HFB09a]. Among which, the small-signal output current Δi_{cw} is normalized with a fictive supply current I_B, which is defined by Eq. 5.1. Since the frequency control mode and the duty cycle control mode are respectively adopted for different operating points, the poles of $G_{if}(s)$ and $G_{id}(s)$ are denoted as ω_{fpi} or ω_{dpi}, respectively.

$$\Delta i_{cwn} = \frac{\Delta i_{cw}}{I_B},\ I_B = \frac{U_{in}}{Z} \tag{5.1}$$

$$\begin{aligned} G_{if}(s) &= \frac{\Delta i_{cwn}}{\Delta f_{sn}} \\ &= \frac{G_{f0}\left(1+\frac{s}{\omega_{fz1}}\right)\left[1-2\xi_{fz2,3}(\frac{s}{\omega_{fz2,3}})+(\frac{s}{\omega_{fz2,3}})^2\right]\left[1+2\xi_{fz4,5}(\frac{s}{\omega_{fz4,5}})+(\frac{s}{\omega_{fz4,5}})^2\right]}{\left(1+\frac{s}{\omega_{fp1}}\right)\left[1+2\xi_{fp2,3}(\frac{s}{\omega_{fp2,3}})+(\frac{s}{\omega_{fp2,3}})^2\right]\left[1+2\xi_{fp4,5}(\frac{s}{\omega_{fp4,5}})+(\frac{s}{\omega_{fp4,5}})^2\right]} \end{aligned} \tag{5.2}$$

$$\begin{aligned} G_{id}(s) &= \frac{\Delta i_{cwn}}{\Delta d} \\ &= \frac{G_{d0}\left(1+\frac{s}{\omega_{dz1}}\right)\left(1+\frac{s}{\omega_{dz2}}\right)\left[1+2\xi_{dz3,4}(\frac{s}{\omega_{dz3,4}})+(\frac{s}{\omega_{dz3,4}})^2\right]}{\left(1+\frac{s}{\omega_{dp1}}\right)\left[1+2\xi_{dp2,3}(\frac{s}{\omega_{dp2,3}})+(\frac{s}{\omega_{dp2,3}})^2\right]\left[1+2\xi_{dp4,5}(\frac{s}{\omega_{dp4,5}})+(\frac{s}{\omega_{dp4,5}})^2\right]} \end{aligned} \tag{5.3}$$

As an example, in the specified operating regions in Fig. 3.3(a) and Fig. 3.3(b), the eight boundary operating points: OP1-OP8, are thought to have the worst dynamic characteristics. Table 5.1 gives the corresponding parameters of OP1-OP8. The model-based linear controller design is implemented at those worst cases.

Control Variable	Operating Point	Q	f_{sn}	d
Switching Frequency f_s	OP1	2.58	1.046	0.95
	OP2	5.81	1.046	0.95
	OP3	2.58	0.893	0.95
Duty Cycle d	OP4	2.58	1.046	0.95
	OP5	5.81	1.046	0.95
	OP6	2.58	1.046	0.025
	OP7	8.88	1.046	0.025
	OP8	8.88	1.046	0.503

Table 5.1: Parameters of Boundary Operating Points OP1-OP8

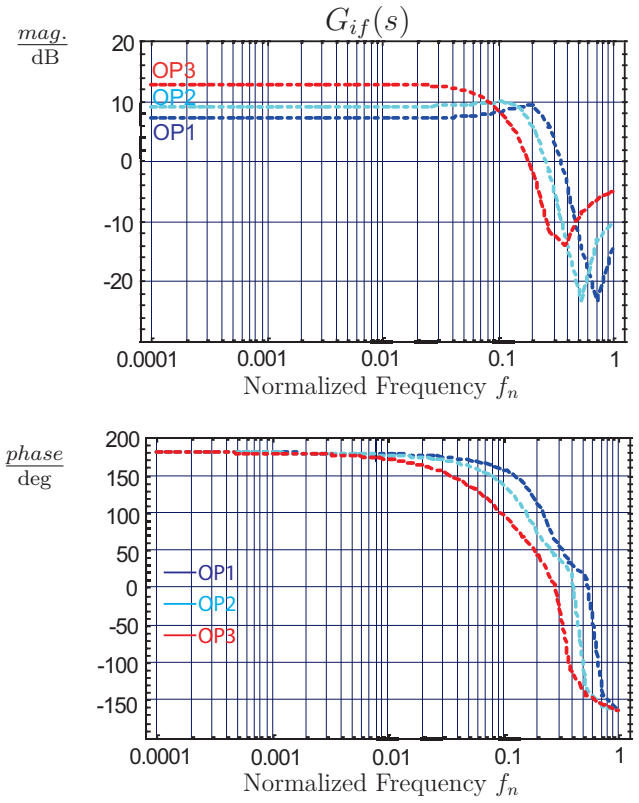

Figure 5.1: Bode diagrams of f_{sn}-to-i_{cwn} transfer function about OP1-OP3 with LCC resonant converter parameters: $C_s = 250$ nF, $C_p = 260$ nF, $L_s = 136$ μH, $R_s = 0.2$ Ω, $C_L = 3.4$ nF.

Based on the derived small-signal model, the Bode diagrams of the control-to-output-current at OP1-OP8 regarding f_{sn} and d can be obtained, as shown in

Fig. 5.1 and Fig. 5.2, respectively.

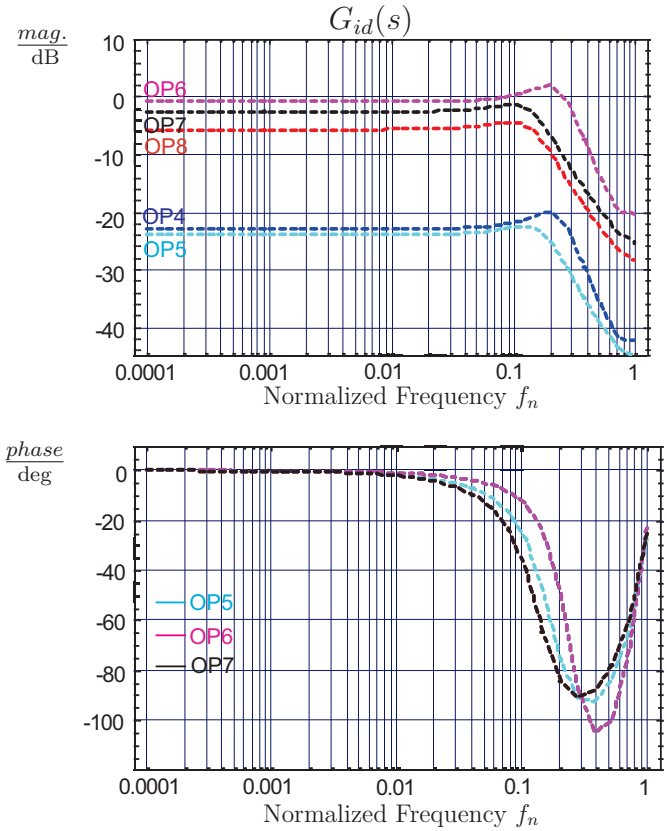

Figure 5.2: Bode diagrams of d-to-i_{cwn} transfer function about OP4-OP8 with LCC resonant converter parameters: $C_s = 250$ nF, $C_p = 260$ nF, $L_s = 136$ μH, $R_s = 0.2$ Ω, $C_L = 3.4$ nF.

From Fig. 5.2, it can be seen that the dynamics of OP4 and OP8 are among the transient characteristics of OP5-OP7, it is reasonable to neglect them in the future dynamics analysis and controller design.

Based on the control-to-output-current transfer functions: Eq. 5.2 and Eq. 5.3, the detailed parameters for OP1-OP3 and OP5-OP7 can be calculated, as represented in Table 5.2, which including the low frequency gain: G_{f0} or G_{d0}, the zeros: ω_{fzi} or ω_{dzj}, and the poles: ω_{fpi} or ω_{dpi} (i=1-5, j=1-4).

From Table 5.2, it can be seen that in the studied frequency region, $G_{if}(s)$ has two right half-plane (RHP) zeros ($\omega_{fz2,3}$), three left half-plane (LHP) zeros (ω_{fz1}, $\omega_{fz4,5}$), and five left half-plane (LHP) poles (ω_{fp1}, $\omega_{fp2,3}$, $\omega_{fp4,5}$); while $G_{id}(s)$

Control Variable	Operating Point	G_{f0} or G_{d0}	ω_{fz1} or ω_{dz1} $1/s$	ω_{dz2} $1/s$	$\omega_{fz2,3}$ or $\omega_{dz3,4}$ $1/s$	$\omega_{fz4,5}$ $1/s$
f_s	OP1	-2.285	3.49×10^6	n/a	1.57×10^5	4.33×10^5
	OP2	-2.85	1.55×10^6	n/a	1.16×10^5	4.13×10^5
	OP3	-4.374	3.49×10^6	n/a	7.88×10^4	3.74×10^5
d	OP5	0.063	1.12×10^5	1.55×10^6	2.64×10^5	n/a
	OP6	0.899	3.49×10^6	3.29×10^5	2.06×10^5	n/a
	OP7	0.733	1.01×10^6	7.79×10^4	2.78×10^5	n/a

⋮

		ω_{fp1} or ω_{dp1} $1/s$	$\omega_{fp2,3}$ or $\omega_{dp2,3}$ $1/s$	$\omega_{fp4,5}$ or $\omega_{dp4,5}$ $1/s$	$\xi_{fp2,3}$ or $\xi_{dp2,3}$	$\xi_{fz2,3}$ or $\xi_{dz3,4}$	$\xi_{fp4,5}$ or $\xi_{dp4,5}$	$\xi_{fz4,5}$
f_s	OP1	6.54×10^6	3.98×10^5	5.72×10^4	0.042	0.042	0.376	0.019
	OP2	4.64×10^6	3.87×10^5	4.16×10^4	0.037	0.034	0.5	0.013
	OP3	6.09×10^6	3.6×10^5	2.9×10^4	0.052	0.129	0.852	0.031
d	OP5	4.64×10^6	3.87×10^5	4.16×10^4	0.037	0.386	0.497	n/a
	OP6	6.54×10^6	3.98×10^5	5.72×10^4	0.042	0.37	0.376	n/a
	OP7	4.12×10^6	3.82×10^5	3.39×10^4	0.032	0.355	0.528	n/a

Table 5.2: Parameters of Control-to-Output-Current Transfer Functions. Notes: with LCC resonant converter parameters: $C_s = 250$ nF, $C_p = 260$ nF, $L_s = 136$ μH, $R_s = 0.2$ Ω, $C_L = 3.4$ nF.

has four LHP zeros (ω_{dz1}, ω_{dz2}, $\omega_{dz3,4}$) and five LHP poles (ω_{dp1}, $\omega_{dp2,3}$, $\omega_{dp4,5}$). Among them, $\omega_{fp4,5}$ or $\omega_{dp4,5}$ are beat frequency poles, which determine system beat frequency dynamics. Since the interested frequency region is much less than the resonant frequency ω_0, some zeros (ω_{fz1}, $\omega_{fz4,5}$, $\omega_{dz3,4}$) and poles (ω_{fp1}, $\omega_{fp2,3}$, ω_{dp1}, $\omega_{dp2,3}$), which are larger than or almost the same as the resonant frequency ($\omega_0 \approx 2.4 \times 10^5$ /s), would have less effect on system dynamics or controller design, and will be ignored.

The resulting reduced-order transfer functions are obtained and represented in Eq. 5.4 and Eq. 5.5. Among which, $G_{if}{}'(s)$ and $G_{id}{}'(s)$ denote the reduced-order

control-to-output-current transfer function regarding f_{sn} and d, respectively.

$$G_{if}{}'(s) = \frac{G_{f0}\left[1 - 2\xi_{fz2,3}(\frac{s}{\omega_{fz2,3}}) + (\frac{s}{\omega_{fz2,3}})^2\right]}{\left[1 + 2\xi_{fp4,5}(\frac{s}{\omega_{fp4,5}}) + (\frac{s}{\omega_{fp4,5}})^2\right]} \tag{5.4}$$

$$G_{id}{}'(s) = \frac{G_{d0}\left(1 + \frac{s}{\omega_{dz1}}\right)\left(1 + \frac{s}{\omega_{dz2}}\right)}{\left[1 + 2\xi_{dp4,5}(\frac{s}{\omega_{dp4,5}}) + (\frac{s}{\omega_{dp4,5}})^2\right]} \tag{5.5}$$

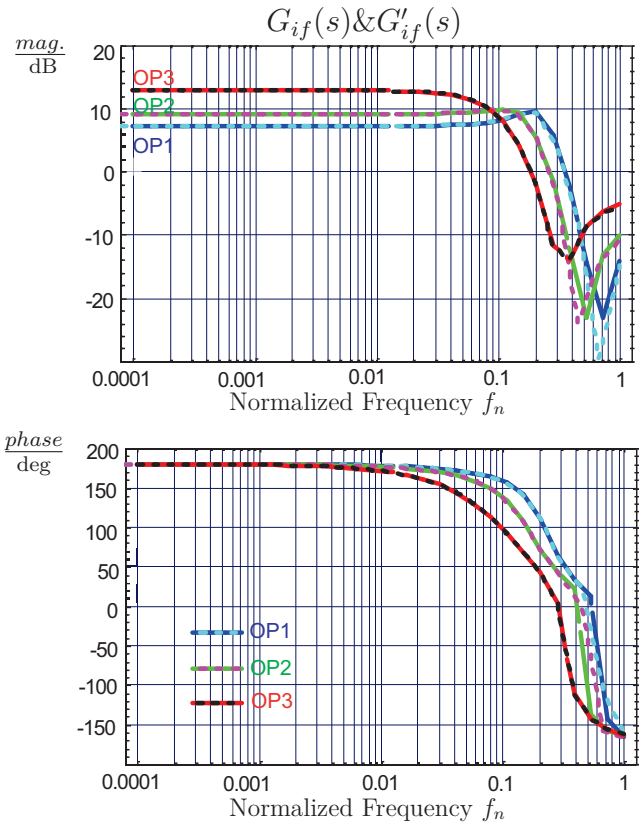

Figure 5.3: Comparison between original and reduced-order f_{sn}-to-i_{cwn} transfer functions at OP1-OP3. Solid: original transfer functions. Dotted line: reduced-order transfer functions.

In order to verify the correctness of the reduced-order transfer functions, the following comparison between the original and reduced-order control-to-output-current transfer functions is implemented. Fig. 5.3 shows the comparison results of the original and reduced-order f_{sn}-to-i_{cwn} transfer functions at OP1-OP3; while

Fig. 5.4 shows the comparison results of the original and reduced-order d-to-i_{cwn} transfer functions at OP5-OP7. The solid lines denote the original transfer functions Bode diagrams; while the dashed lines denote the reduced-order transfer functions Bode diagrams.

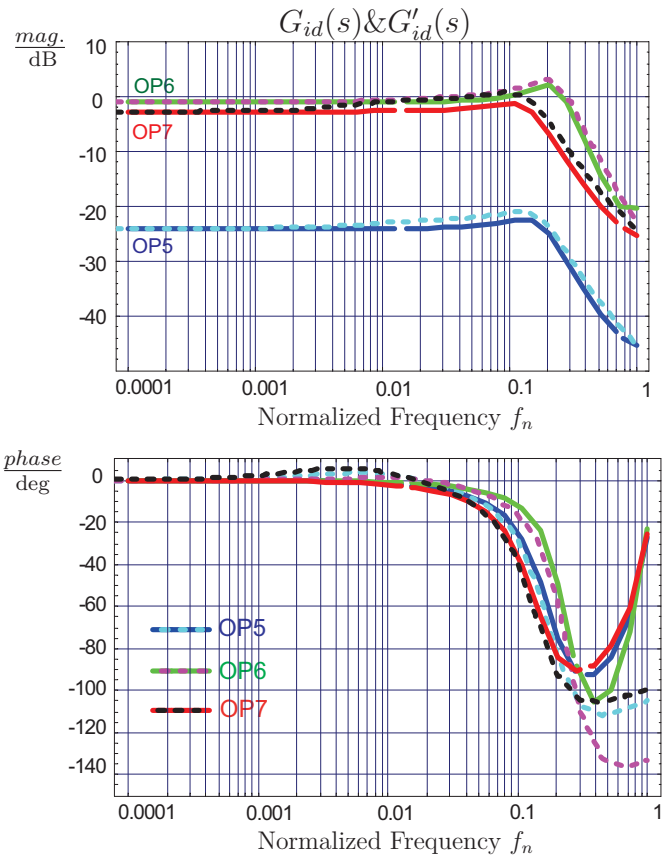

Figure 5.4: Comparison between original and reduced-order d-to-i_{cwn} transfer functions at OP5-OP7. Solid: original transfer functions. Dotted line: reduced-order transfer functions.

Conclusions can be drawn from above comparison: in the studied frequency region, there is almost no deviation between the original and the reduced-order transfer functions with frequency control mode. With the duty cycle control mode, both magnitude bode plots are nearly the same in the whole studied region; there exists some deviation in the phase comparison at high-frequency region, but they have negligible effect on the closed-loop design. From these conclusions, it can

be ensured that a controller design on the basis of the reduced-order transfer function is feasible and reasonable.

5.3 Current Mode Linear Control Design

Current programmed mode (CPM) control scheme is widely adopted as a useful technique for easing the design and improving the performance of the switched-mode converter systems. The basic principle and the advantages of the CPM have been discussed in numerous literatures [EM00] [Deird] [CFOW78], the chief advantage is its simpler dynamics.

The loop gain method [YCL+92] [RCL98] is used for the linear proportional-integral (PI) current mode controller design. Since the LCC resonant converter has two control variables: f_s and d, the reduced-order transfer function $G_{if}{}'(s)$ and $G_{id}{}'(s)$ are the corresponding open-loop transfer functions. The loop gains for the both control modes are denoted as $L_f(s)$ and $L_d(s)$, respectively (refer to Fig. 5.5):

$$L_f(s) = G_{cf}(s)G_{if}{}'(s)H(s), \tag{5.6}$$

$$L_d(s) = G_{cd}(s)G_{id}{}'(s)H(s). \tag{5.7}$$

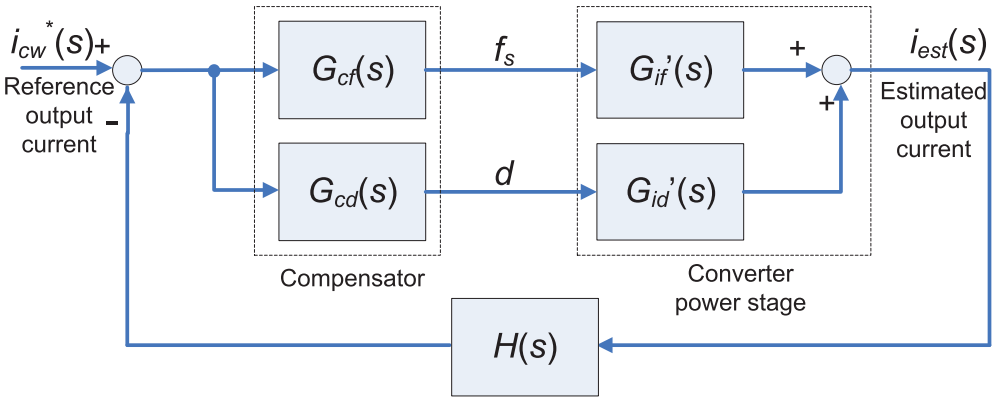

Figure 5.5: Current mode control block diagram

In Eq. 5.6 and Eq. 5.7, $G_{cf}(s)$ and $G_{cd}(s)$ are the respective compensators for the frequency control mode and the duty cycle control mode; $H(s)$ denotes the

feedback transfer function in the closed-loop. Based on $G_{if}{}'(s)$ and $G_{id}{}'(s)$, two simple and commonly used linear PI compensators can be designed as follows:

$$G_{cf}(s) = \frac{K_{cf}(1 + s/\omega_{cf})}{s}, \tag{5.8}$$

$$G_{cd}(s) = \frac{K_{cd}(1 + s/\omega_{cd})}{s}. \tag{5.9}$$

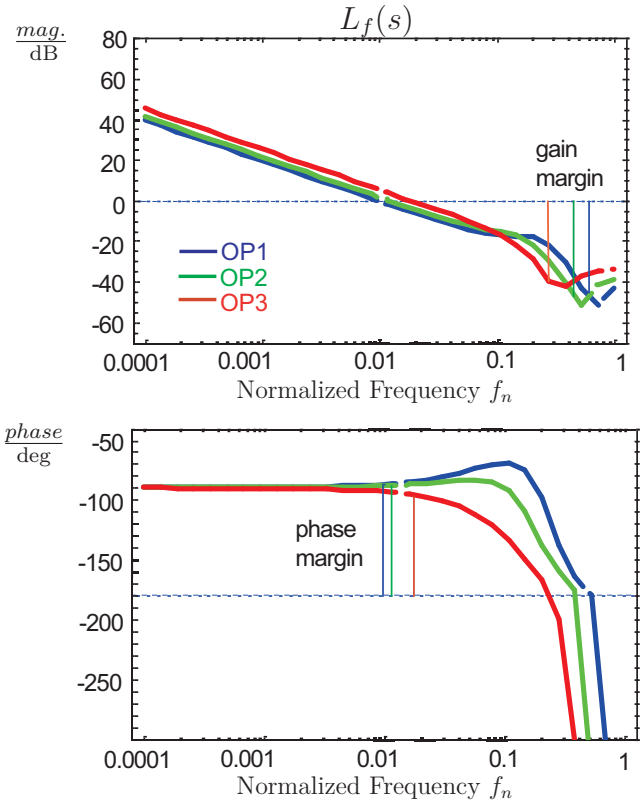

Figure 5.6: The loop gains of boundary operating points at OP1-OP3 with frequency control

By adjusting the compensator parameters, we can maximize the control bandwidth and maintain sufficient phase margins and gain margins. Attention should be paid to the adjustment of the two zeros: ω_{cf} and ω_{cd}, which are equal in this application: $\omega_{cf} = \omega_{cd} = \omega_c$, because both the switching frequency f_s and the

duty cycle d are generated from the same PWM generator of the LCC resonant converter.

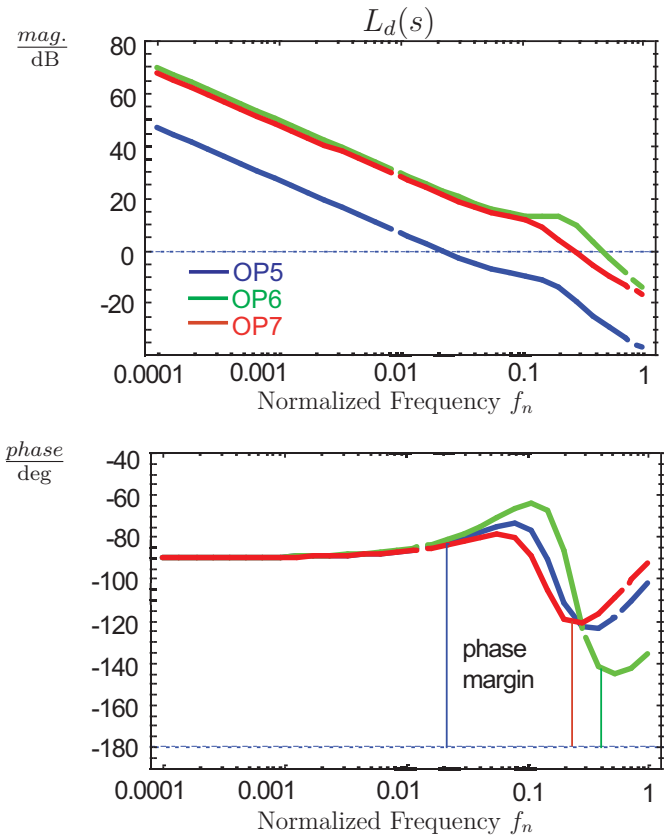

Figure 5.7: The loop gains of boundary operating points at OP5-OP7 with duty cycle control

After assuming $H(s) = 1$, $L_f(s)$ and $L_d(s)$ at the boundary operating points: OP1-OP3, OP5-OP7, can be obtained. The equations are shown in Eq. 5.10 and Eq. 5.11, and the Bode diagrams are represented in Fig. 5.6 and Fig. 5.7, respectively.

$$L_f(s) = \frac{G_{f0}K_{cf}(1 + s/\omega_c)\left[1 - 2\xi_{fz2,3}(\frac{s}{\omega_{fz2,3}}) + (\frac{s}{\omega_{fz2,3}})^2\right]}{s\left[1 + 2\xi_{fp4,5}(\frac{s}{\omega_{fp4,5}}) + (\frac{s}{\omega_{fp4,5}})^2\right]} \tag{5.10}$$

$$L_d(s) = \frac{G_{d0}K_{cd}(1 + s/\omega_c)\left(1 + \frac{s}{\omega_{dz1}}\right)\left(1 + \frac{s}{\omega_{dz2}}\right)}{s\left[1 + 2\xi_{dp4,5}(\frac{s}{\omega_{dp4,5}}) + (\frac{s}{\omega_{dp4,5}})^2\right]} \tag{5.11}$$

From the Bode diagrams, it can be seen that both the phase margins and gain margins of $L_f(s)$ and $L_d(s)$ are adequate. For the designed simple type PI compensator, it can be said that the system with separate frequency control or with the separate duty cycle control is respectively stable. There is an apparent shortcoming in the duty cycle control mode, as illustrated in Fig. 5.7: the control bandwidth drops significantly at different operating points. This phenomenon can be explained by the fact that the low-frequency gains G_{d0} of the d-to-i_{cwn} transfer function, is much different at various operating points. For example, the low-frequency gain difference is about 23 dB between operating points OP5 and OP6 (refer to Fig. 5.4). Hence, it is desirable to adopt some nonlinear control schemes to schedule the compensator gain for performance improvement.

5.4 Simulated Results of Linear PI Controller

Before the launch of prototype, simulation of the current mode linear PI controller is implemented. In order to compare with the corresponding simulation results in Chapter 6 and Chapter 7, the reference and simulated signals of i_{cw} are transferred to the corresponding reference and simulated signals of the effective resonant current i_{Leff}, respectively. The simulated results are represented in Fig. 5.8 and Fig. 5.9. Among which, Fig. 5.8 provides the blue pulsing reference signal i^*_{Leff}, whose amplitude changes between 0.4 A and 2.0 A with 50 % duty cycle, and the period is 20 ms. The simulated red i_{Leff} tracks i^*_{Leff} and arrives the maximal amplitude in 3 ms with a little spike; i_{Leff} tracks i^*_{Leff} and arrives the minimal amplitude in about 3 ms perfectly. Fig. 5.9 represents the blue sinusoidal reference signal i^*_{Leff}, which has the amplitude from 0.3 A to 1.9 A with increasing frequency from 10 Hz to 100 Hz in 0.1 s. The simulated red i_{Leff} agrees well with the sinusoidal reference signal i^*_{Leff} except a little deviation at the initial stage. Generally speaking, the closed loop controller has good performance under various given conditions, which verifies the correctness of the current mode linear PI controller design.

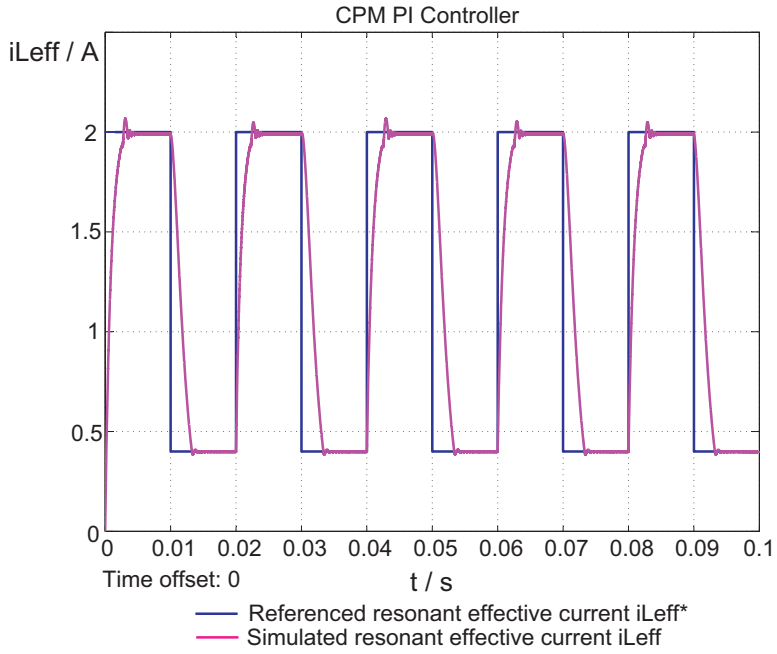

Figure 5.8: Simulated i_{Leff} under pulsing reference signal i^*_{Leff} with amplitude changes between 0.4 A and 2.0 A with 50 % duty cycle and 20 ms period. Refer to Fig. 6.6 and Fig. 7.7 for comparison.

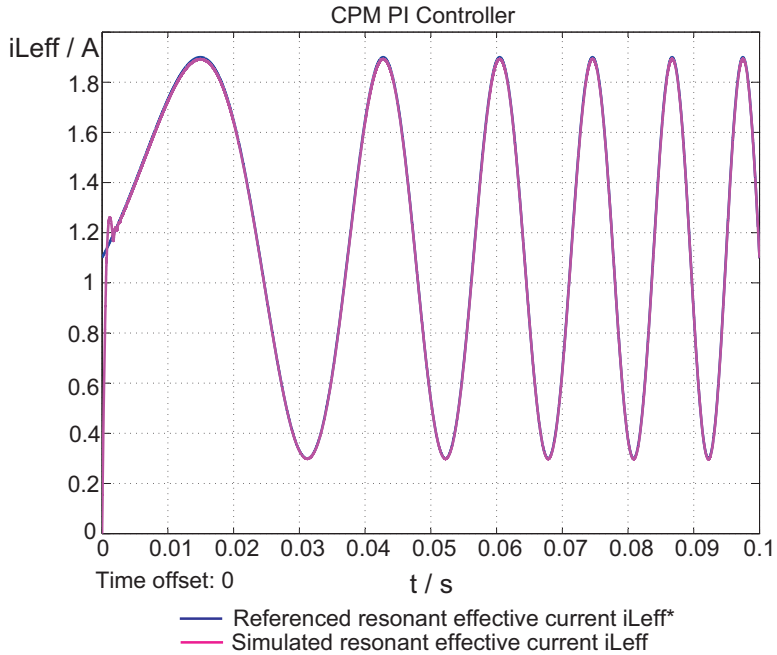

Figure 5.9: Simulated i_{Leff} under sinusoidal reference signal i^*_{Leff} with magnitudes change from 0.3 A to 1.9 A, and frequency changes from 10 Hz to 100 Hz in 100 ms. Refer to Fig. 6.7 and Fig. 7.8 for comparison.

5.5 Real-Time Implementation Issues of Linear PI Controller

A. Compensator's combination

In Fig. 5.5, there are two PI compensators: $G_{cf}(s)$ and $G_{cd}(s)$, which are adopted for separate frequency mode control and duty cycle mode control, the respective closed loop stability is already verified based on Bode diagramm results. In practice, they should be combined as one compensator $G_{iu}(s)$ to avoid probable closed loop instability.

Since the two zeros: ω_{cf} and ω_{cd} in $G_{cf}(s)$ and $G_{cd}(s)$ are equal and are replaced by ω_c, the combined compensator $G_{iu}(s)$ can be represented as:

$$G_{iu}(s) = \frac{K_{iu}(1 + s/\omega_c)}{s}. \tag{5.12}$$

The primary compensator gains: K_{cf}, K_{cd}, can be expressed by K_{iu} and two newly introduced parameters: K_f and K_d.

$$K_{cf} = K_{iu}K_f \tag{5.13}$$

$$K_{cd} = K_{iu}K_d \tag{5.14}$$

An auxiliary control parameter μ is introduced to combine both frequency control mode and duty cycle control mode. f_s and d are denoted as the linear functions of μ, their slopes are depending on K_f or K_d, respectively, as shown in Fig. 5.10.

When $\mu \leq 0$, $f_s = f_{s\_max}$, $d = d_{\_min}$.
When $0 \leq \mu \leq \mu 1$, $f_s = f_{s\_max}$, $d = k_d \cdot \mu$.
When $\mu 1 \leq \mu \leq \mu 2$, $f_s = k_f \cdot \mu$, $d = d_{\_max}$.
When $\mu \geq \mu 2$, $f_s = f_{s\_min}$, $d = d_{\_max}$.

Through such combination, separate frequency control and duty cycle control are integrated together, which realizes the system control in a relative wide operating region and ensures the stability.

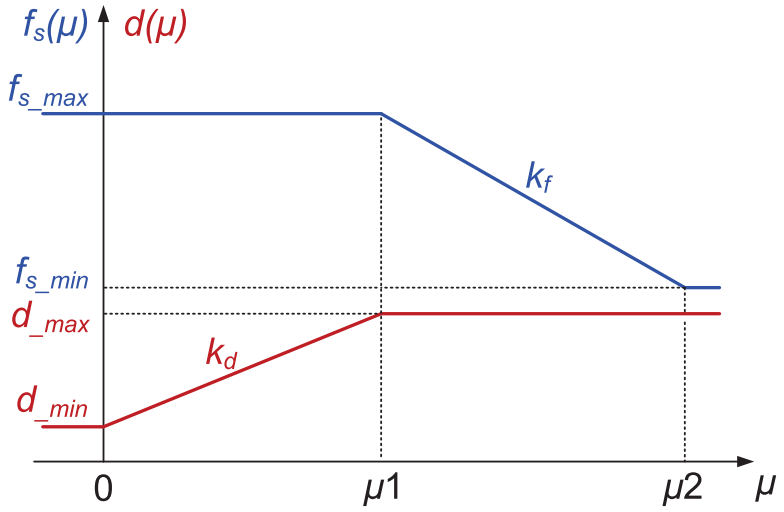

Figure 5.10: Transition from auxiliary variable μ to control variables: f_s and d

B. Estimator

Since it is difficult and very costly to directly measure the output current i_{cw} due to high voltage application, an estimator is adopted in the actual CPM closed-loop control. The estimated output current $i_{est}(t)$ is relevant to the output voltage $u_o(t)$, amplitude of the resonant current $i_{Lp}(t)$, parallel capacitor C_p and the switching frequency $f_s(t)$, as shown below [HFB09b] [HFB09a].

$$i_{est}(t) = \frac{i_{Lp}(t) - \pi f_s(t) C_p u_o(t)}{\pi} \tag{5.15}$$

Fig. 5.11 represents the two-loop control block diagram with estimator. A conventional linear PI compensator $G_{uc}(s)$ is applied in the voltage control loop, with the integrated inner current control loop, such $G_{uc}(s)$ design becomes easy and can be directly derived from the output load characteristics [CHFB10]. The referenced current i_c is generated from the voltage loop, after comparing with the estimated output current i_{est}, an error signal is input into the compensator $G_{iu}(s)$, which further generates the auxiliary control variable μ. After simple transition from μ, the actual control variables: f_s and d are derived and send to the LCC resonant converter. u_o and i_L are measured from the plant, set to the estimator and compose the feed-back loop.

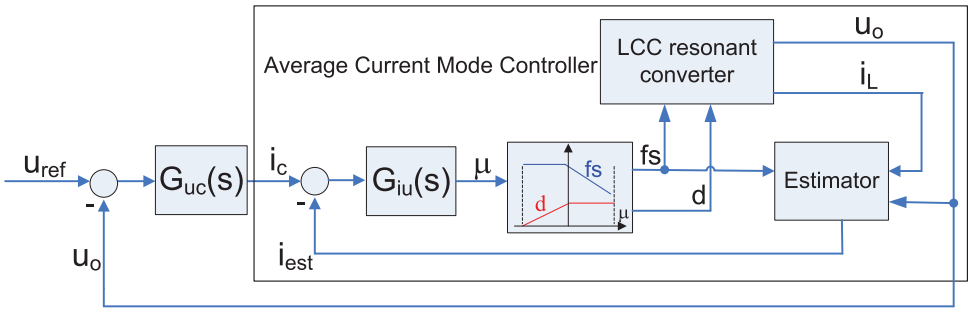

Figure 5.11: Two-loop control block diagram with estimator

5.6 Experimental Results of CPM Linear Controller

Two prototypes are built before the implementation of the VLF high voltage generator.

One is a simplified prototype with equivalent output power, which consists of LCC resonant inverter, 1:2 transformer, one-stage symmetrical CW multiplier and a corresponding resistive load, Fig. 5.12 shows each part separately. This scaled-down prototype was built and measured in order to validate the system structure and the current mode controller design.

Fig. 5.13 provide the experimental results based on the scaled-down prototype. The resonant current amplitude i_Lp, the estimated output current i_{est}, and the control variables: f_s, d, are measured under the step change conditions from initial states to the given referenced steady-states. In Fig. 5.13(a), i_c is set to 2 A at constant referenced output voltage (440 V) condition; while in Fig. 5.13(b), the expected output current is 4 A with constant referenced output voltage (880 V) condition. It can be seen from the measurements that the estimated output currents $i_{est}(t)$ agree the expected reference signal i_c without overshoot and the settling time is less than 1 ms, which confirms the conclusions of above analyses and validates the current mode linear PI controller design.

The other prototype is a real VLF high voltage generator, which consists of LCC resonant inverter, 1:15 HV-transformer, three-stage symmetrical CW multiplier, a resistive discharge circuit [CHFB10] [CFB09a] [CFB09b] and a capacitive

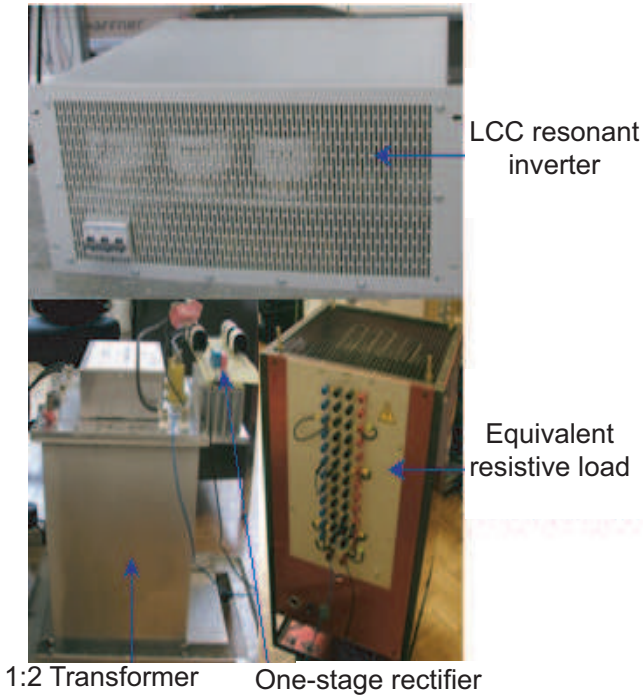

Figure 5.12: A scaled-down prototype with 1:2 transformer and one-stage CW multiplier

load, as shown in Fig. 5.14. This prototype is used to validate all the design specifications, including the control performance of the cascaded two closed loops and the sinusoidal high voltage output voltage.

Fig. 5.15 provides the experimental result of the output voltage from the real VLF high voltage prototype. With cascaded two closed-loop design, the actual output voltage of the VLF high voltage generator has perfect sinusoidal waveform with a peak value of nearly 120 kV and a period of 10 s, the total harmonic distortion (THD) is about 1 %, which is far better than the 5 % design specifications.

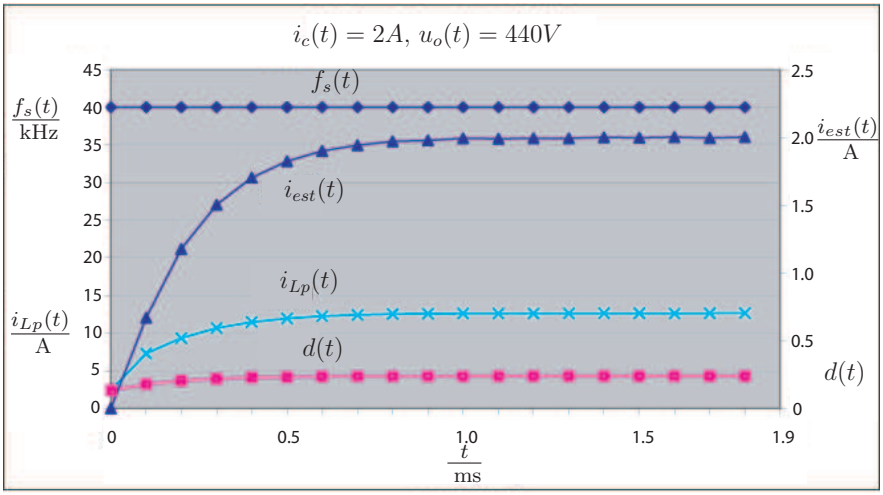

(a)

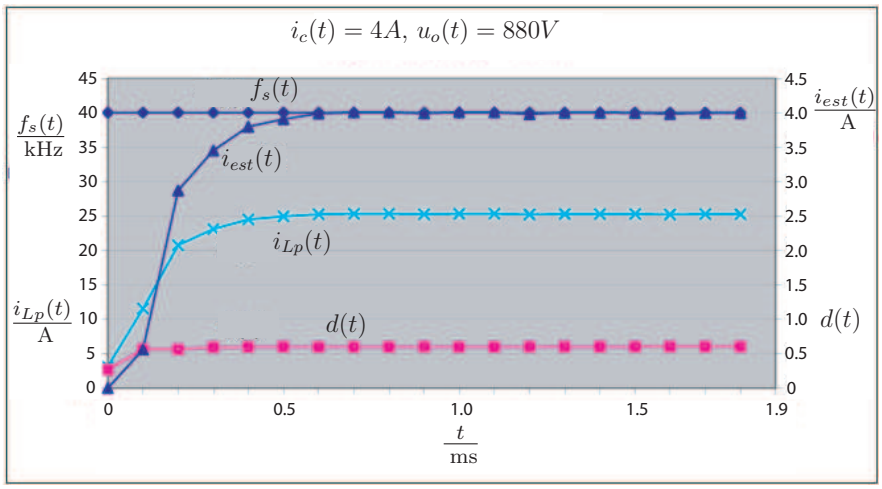

(b)

Figure 5.13: Closed-loop CPM controller verification through measurements of step change response on scaled-down prototype

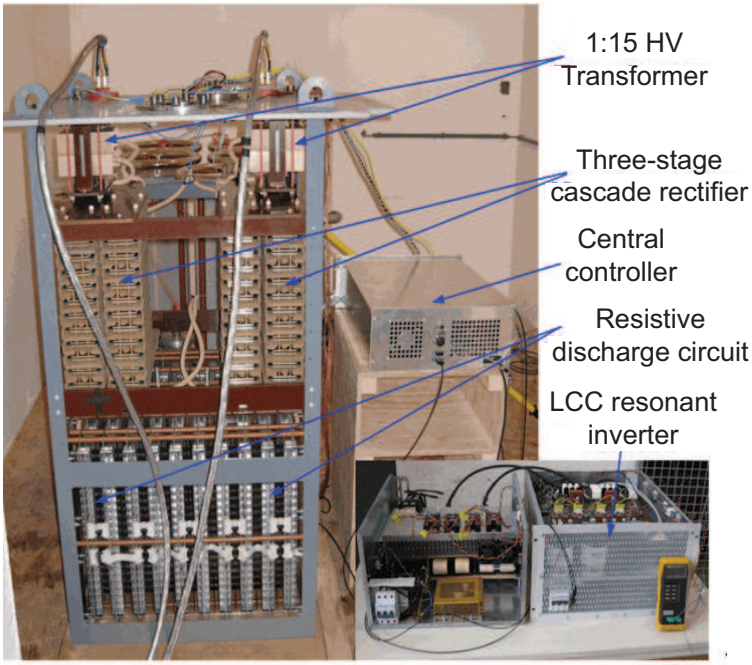

Figure 5.14: Real prototype with LCC resonant inverter, 1:15 HV-transformer and three-stage CW multiplier

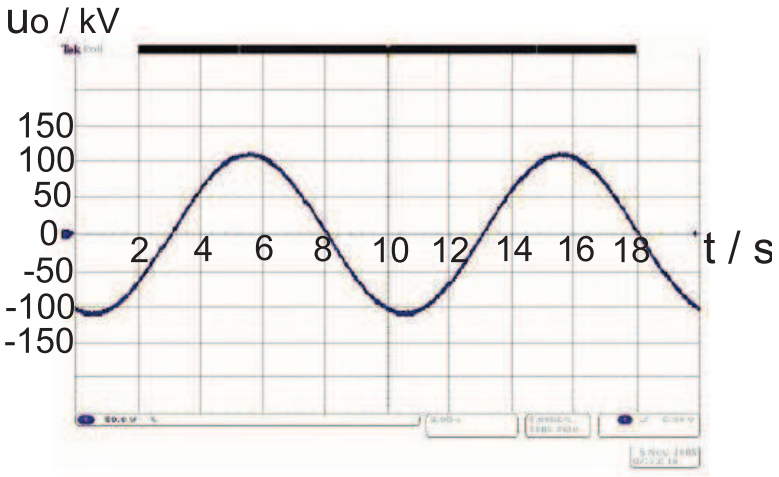

Figure 5.15: Measured output voltage of a real VLF high voltage generator prototype

5.7 Summary

A current mode linear PI controller is primarily developed for the LCC resonant converter in this Chapter due to its simple structure, ease of design and low cost in implementation. Reduced-order control-to-output-current transfer functions are derived for a more effective control design. Loop gain method is adopted, which realizes the balance between gain margin, phase margin and control bandwidth. A creative method is used to combine separate frequency control mode and duty cycle control mode. In practice, the simulated controller parameters should be accommodated to realize the closed loop stability and control performance. An output current estimator is implemented to avoid difficult and costly measurement.

The provided simulated and experimental results verify and validate the correctness of the developed PI controller. But the shortage of the linear PI controller is also obvious: It has poor dynamic characteristics and narrow control bandwidth. Under a given step-change reference signal, its settling time is about several ms and the control bandwidth is only several hundred Hz. With the simple linear control structure, a satisfying control performance in the whole wide operating region is not guaranteed, its closed loop control performance is highly dependent on the operating point. The other linear controllers, such as linear PD controller, linear PID controller, are not investigated here. But due to their similar linear control structure, their closed loop control performance is probably also dependent on the operating point.

An investigation about a nonlinear control scheme is expected.

Chapter 6

Fuzzy PD Control Design

6.1 Introduction

As represented in Chapter 5, the closed-loop performance of a conventional linear controller is not so satisfactory for a nonlinear system with a wide operating region. Some nonlinear control schemes are expected for the performance improvement.

Fuzzy sets and systems have gone through substantial development since the introduction of fuzzy set theory by Zadeh [Zad65] [Zad75] about four decades ago. The fuzzy logic control (FLC) was well known for its ability to handle nonlinearities and uncertainties through use of fuzzy set theory. In fact, FLC has been proven to be a successful control approach to many complex nonlinear systems or even non-analytic systems. It has been suggested as an alternative approach to conventional control techniques on many cases [Fen06].

The basic structure of a fuzzy control system consists of four conceptual components: knowledge base, inference engine, fuzzification interface and defuzzification interface. The block diagram of the fuzzy control system is shown in Fig. 6.1. The knowledge base contains all the controller knowledge and it is comprised of a fuzzy control rule base and a data base. The fuzzy control rule base is the procedural part of the knowledge base which contains information on how these objects can be used to infer new control actions. The data base is the declarative part of the knowledge base which describes definition of objects and definition of membership functions used in the fuzzy control rules. The inference engine is

a reasoning mechanism which performs inference procedure upon the fuzzy control rules and gives conditions to derive reasonable control actions, which is the central part of a fuzzy control system. The fuzzification interface (or fuzzifier) defines a mapping from a real-valued space to a fuzzy space, which converts a crisp value to a fuzzy number; while the defuzzification interface (or defuzzifier) defines a mapping from a fuzzy space over an output universe of discourse to a real-valued space, which converts the inferred fuzzy conclusion to a crisp value [Fen06].

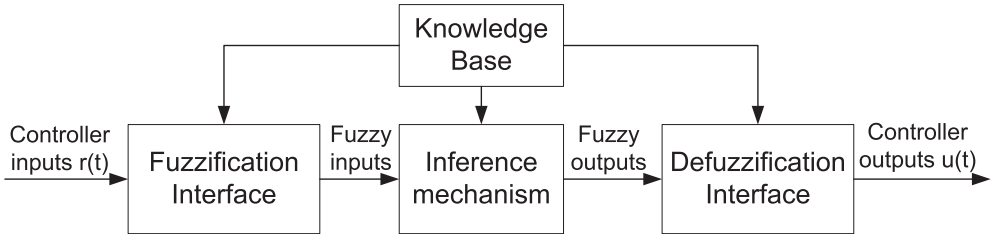

Figure 6.1: Basic structure of a fuzzy control system

Based on the differences of fuzzy control rules and their generation methods, approaches to fuzzy logic control can be roughly classified into the following categories: 1) conventional fuzzy control; 2) fuzzy proportional-integral-derivative (PID) control; 3) neuro-fuzzy control; 4) fuzzy-sliding mode control; 5) adaptive fuzzy control; and 6) Takagi-Sugeno (T-S) model-based fuzzy control. However, it should be noted that the overlapping among these categories is inevitable.

Two types of above fuzzy logic control are implemented for the LCC resonant converter. One is the conventional fuzzy control, which is realized in this Chapter; the other is the Takagi-Sugeno (T-S) model-based fuzzy control, which is represented in Chapter 7.

6.2 Conventional Fuzzy PD Controller Development

Since the current mode control is advantegeous and it is sequentially adopted in this chapter. In order to more conveniently realize the current control with-

out additional estimator, a directly resonant current control is implemented, the effective resonant current i_{Leff} is selected as the control objective.

As a model-free control, the knowledge base of the conventional fuzzy control is mostly dependent on a good understanding of the behaviour of the LCC resonant converter. From Fig. 3.3, the steady-state characteristics of the LCC resonant converter are known. In the expected operating region, the low frequency gain of the control-to-output transfer functions G_{f0}, G_{d0}, can be obtained, which is proportional to the respective slope of the DC conversion ratio curve at the specified operating point, respectively. Among which, G_{f0} is proportional to the slope of f_{sn}-to-M conversion ratio curve at the specified operating point in Fig. 3.3(a); while G_{d0} is proportional to the slope of d-to-M conversion ratio curve at the specified operating point in Fig. 3.3(b). It is obvious that in preferable operating region, G_{f0} is negative and G_{d0} is positive. Also, due to the similar change pattern of the gain of control-to-resonant-current transfer function and that of control-to-output-voltage transfer function (refer to Fig. 3.4(a) and Fig. 3.4(b)), the following formulas can be obtained:

$$G_{f0} \propto \frac{\partial M}{\partial f_{sn}} \propto \frac{\partial i_{Lp}}{\partial f_{sn}} < 0 \tag{6.1}$$

$$G_{d0} \propto \frac{\partial M}{\partial d} \propto \frac{\partial i_{Lp}}{\partial d} > 0 \tag{6.2}$$

A. Rule base

Based on above steady-state characteristics and practical experiences, the corresponding rule base for current-mode fuzzy PD control can be derived, as represented in Table 6.1. The error signal $e(t)$ is the difference between the reference resonant effective current i^*_{Leff} and the real resonant effective current i_{Leff}; its derivative $de(t)/dt$ denotes the change-in-error. Both of them are selected as the inputs of the fuzzy PD controller. According to given $e(t)$ and $de(t)/dt$, the corresponding fuzzy logic control actions $u(t)$ can be generated, which is the output of the fuzzy PD controller.

In order to conveniently apply the fuzzy PD controller in digital processing and control, all of the linguistic statements are transferred to corresponding numeric-linguistic values. As shown in Table 6.1, the ranges of $e(t)$ and $de(t)/dt$ are

divided into nine subsections and indicated as rule number from "0" to "8", respectively. Among which, "0" corresponds to negative maximal error or negative maximal error derivative; "4" corresponds to zero error or zero error derivative; "8" corresponds to positive maximal error or positive maximal error derivative. Correspondingly, the range of fuzzy logic control actions $u(t)$ has also specified as nine parts, which is denoted as rule number from "0" to "8": as "0" indicates zero control output, "4" means the middle control output, and "8" represents the maximal control output [BKS95] [HBF11].

output $u(t)$		error $e(t)$								
		0	1	2	3	4	5	6	7	8
error derivative $de(t)/dt$	0	0	0	0	0	1	2	2	3	8
	1	0	0	1	1	2	2	3	4	8
	2	0	1	2	2	2	3	4	5	8
	3	0	1	2	2	3	4	5	6	8
	4	0	2	2	3	4	5	6	6	8
	5	0	2	3	4	5	6	6	7	8
	6	0	3	4	5	6	6	6	7	8
	7	0	4	5	6	6	7	7	8	8
	8	0	5	6	6	7	8	8	8	8

Table 6.1: Rule base of fuzzy PD controller

The details and the mapping relationship between $e(t)$, $de(t)/dt$ and $u(t)$ can also be obtained from Table 6.1. For example, negative maximal (0) $e(t)$ and negative maximal (0) $de(t)/dt$ will generate minimal (0) $u(t)$, as shown in the left-upper-corner of Table 6.1; and positive maximal (8) $e(t)$ and positive maximal (8) $de(t)/dt$ will generate maximal (8) $u(t)$, as denoted in the right-lower-corner of Table 6.1.

B. Membership function

Membership function is used to quantify the meaning of each numeric-linguistic value, which is a μ function versus $e(t)$, $de(t)/dt$ or $u(t)$. As shown in Fig. 6.2, the membership functions of $e(t)$, $de(t)/dt$ and $u(t)$ are represented, according to the rule base is also demonstrated.

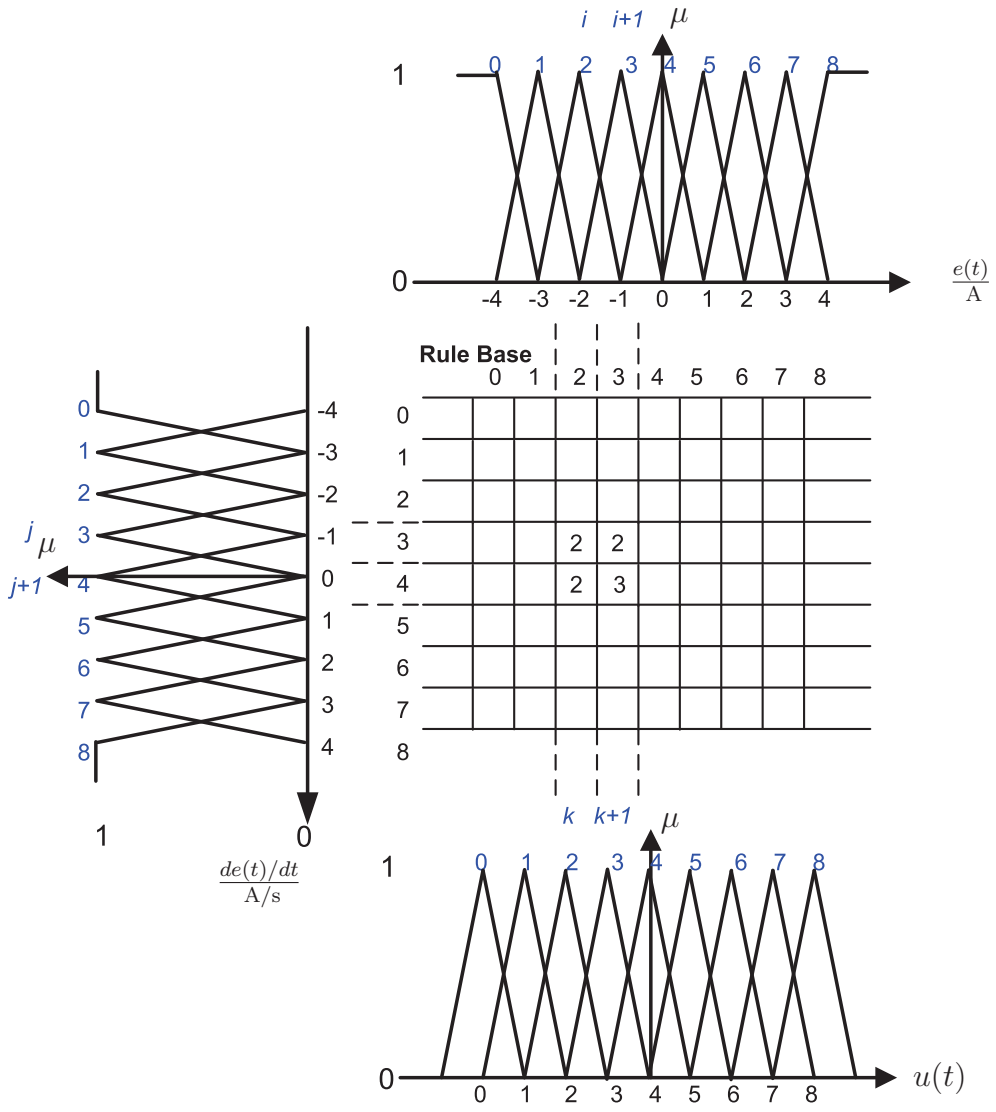

Figure 6.2: Membership functions and the matching of inputs and output of the fuzzy PD controller

It can be seen that the axes of $e(t)$, $de(t)/dt$ and $u(t)$ are denoted with respective marker, which corresponds to their real value. For example, $e(t)$ has the real value range from -4 A to 4 A, while the real value range of $de(t)/dt$ is from -4 A/s to 4 A/s, and the value range of $u(t)$ is appointed from 0 to 8.

Each membership function has a symmetrical triangle form, which is denoted with number from "0" to "8", each of them corresponds to the rule number in

Table 6.1.

The axis of μ gives the certainty value of each membership function, which has the range from 0 to 1. Each summit of the triangle has the certainty 1, while the hemline of each triangle has the certainty 0.

Considering the symmetrical triangle $e(t)$ membership function "2", the function $\mu_2(e(t))$ quantifies the certainty, which can be classified numerically as "rule(2)" of $e(t)$ membership function for an arbitrary $e(t)$. The following interpretation is helpful for understanding.

1. if $e(t) = -2$ A, then $\mu_2(e(t)) = 1$;
2. if -3 A $\leq e(t) \leq -2$ A, then $\mu_2(e(t)) = e(t) + 3$;
3. if -2 A $\leq e(t) \leq -1$ A, then $\mu_2(e(t)) = -e(t) - 1$;
4. if $e(t) \geq -3$ A or $e(t) \leq -1$ A, then $\mu_2(e(t)) = 0$.

Similar definitions for the other membership functions of $e(t)$, $de(t)/dt$ or $u(t)$ can be derived based on above example.

The mapping between $e(t)$, $de(t)/dt$ and $u(t)$ are also represented in Fig. 6.2 with an example. If the control inputs are given as: -2 A $< e(t) < -1$ A and -1 A/s $< de(t)/dt < 0$ A/s, according to Fig. 6.2, two of $e(t)$ membership functions: $\mu_2(e(t))$ and $\mu_3(e(t))$, and two of $de(t)/dt$ membership functions: $\mu_3(de(t)/dt)$ and $\mu_4(de(t)/dt)$, are activated, which corresponds to the overlapping area of row 2, 3 and column 3, 4 in rule base Table 6.1. The corresponding fuzzy control action $u(t)$ can then be derived based on the activated $u(t)$ membership functions: $\mu_2(u(t))$ and $\mu_3(u(t))$.

C. Inference engine

The generation details of the fuzzy control action $u(t)$ are depicted in Fig. 6.3. In which, the minimum method is adopted to ensure the certainty of the combined membership functions. As an example, the control inputs are assumed as the same as the former: -2 A $< e(t) < -1$ A and -1 A/s $< de(t)/dt < 0$ A/s. As aforementioned, $\mu_2(u(t))$ and $\mu_3(u(t))$ are activated. Since $\mu_2(u(t))$ is activated more than once, the superscript is used for distinction.

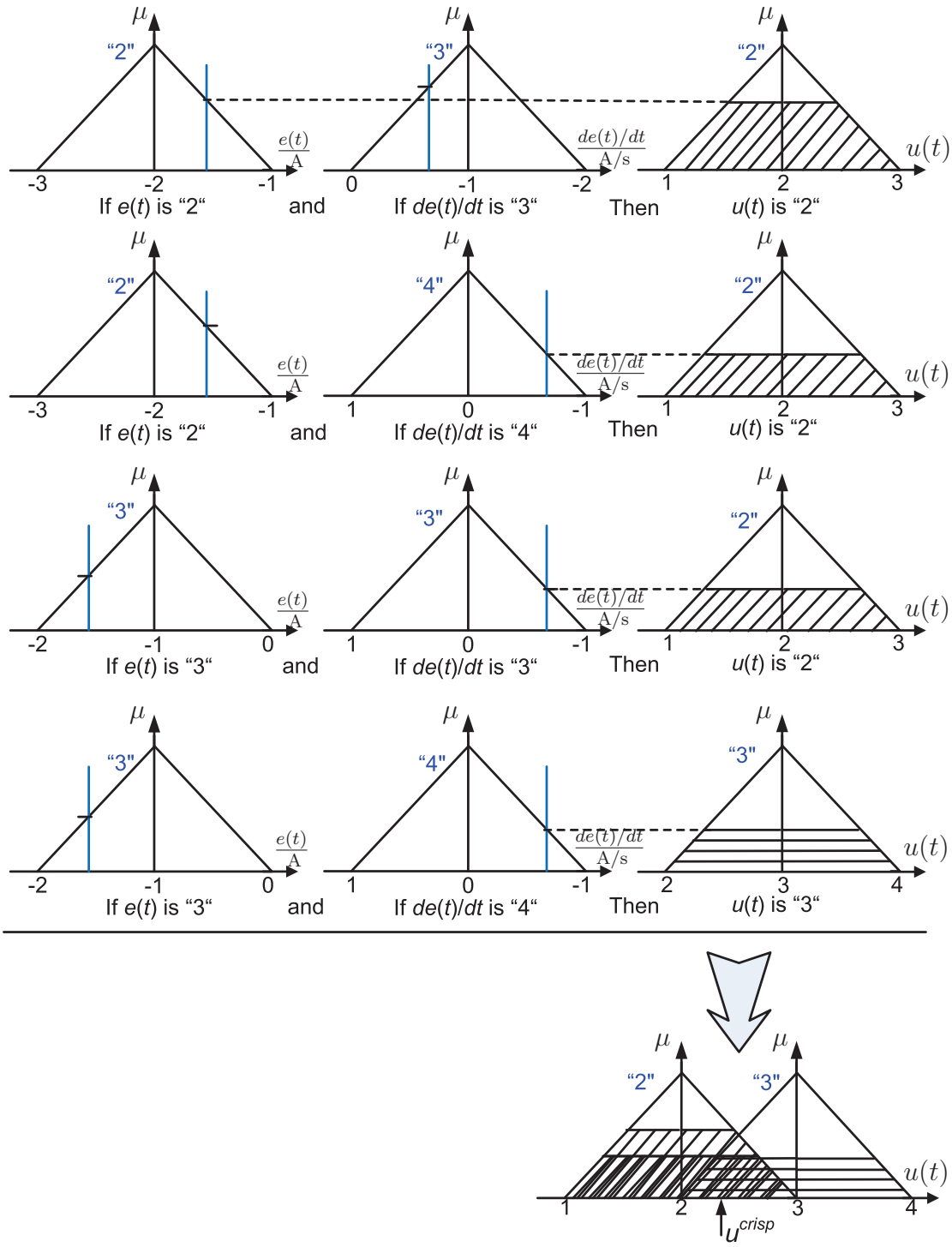

Figure 6.3: Graphical representation of fuzzy controller operations

1. If $e(t)$ is "rule(2)", and $de(t)/dt$ is "rule(3)", Then $u(t)$ is "rule(2)^1". As shown in the first row of Fig. 6.3: $\mu_2(u(t))^1 = min\{\mu_2(e(t)), \mu_3(de(t)/dt)\}$

2. If $e(t)$ is "rule(2)", and $de(t)/dt$ is "rule(4)", Then $u(t)$ is "rule(2)^2". As shown in the second row of Fig. 6.3: $\mu_2(u(t))^2 = min\{\mu_2(e(t)), \mu_4(de(t)/dt)\}$

3. If $e(t)$ is "rule(3)", and $de(t)/dt$ is "rule(3)", Then $u(t)$ is "rule(2)^3". As shown in the third row of Fig. 6.3: $\mu_2(u(t))^3 = min\{\mu_3(e(t)), \mu_3(de(t)/dt)\}$

4. If $e(t)$ is "rule(3)", and $de(t)/dt$ is "rule(4)", Then $u(t)$ is "rule(3)". As shown in the fourth row of Fig. 6.3: $\mu_3(u(t)) = min\{\mu_3(e(t)), \mu_4(de(t)/dt)\}$

As represented in the bottom of Fig. 6.3, the resulting fuzzy control action u^{crisp} is calculated with the center of gravity (COG) method, the formula is shown below [PY97]:

$$u^{crisp} = \frac{\sum\limits_k b_k S(\mu_k(u(t)))}{\sum\limits_k S(\mu_k(u(t)))} \tag{6.3}$$

$$= \frac{b_2 S(\mu_2(u(t))^1) + b_2 S(\mu_2(u(t))^2) + b_2 S(\mu_2(u(t))^3) + b_3 S(\mu_3(u(t)))}{S(\mu_2(u(t))^1) + S(\mu_2(u(t))^2) + S(\mu_2(u(t))^3) + S(\mu_3(u(t)))} \tag{6.4}$$

among which, b_k denotes the center real value of the membership function $\mu_k(u(t))$; and $S(\mu_k(u(t)))$ denotes the area under the membership function $\mu_k(u(t))$.

D. Transition from u to f_s and d

Since the fuzzy control action u is an intermediate fuzzified control output, it should be further transferred to the real LCC resonant converter control variables: f_s and d. As denoted in Fig. 6.4, with a specified modulation limit, f_s is negative proportional to u with a positive offset, while d has a positive proportional relationship with u without offset. The transferred f_s and d are sent to a pulse width modulator (PWM) generator in the digital signal processor (DSP), which drives the transistors of the full-bridge inverter.

Investigations show that the fuzzy PD controller with constant scaling gain for e has poor control performance, such as large steady-state error with small reference resonant effective current i^*_{Leff}, or obvious ripple for large i^*_{Leff}. In

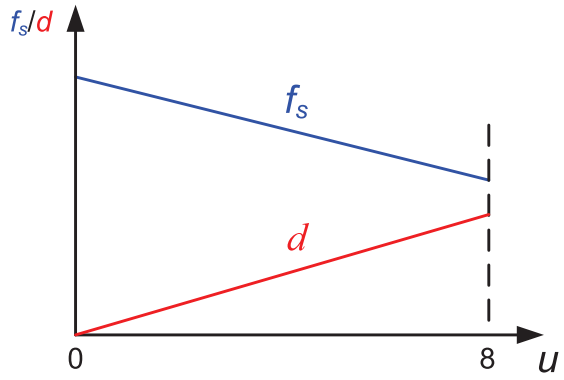

Figure 6.4: Transition diagram between u and f_s, d

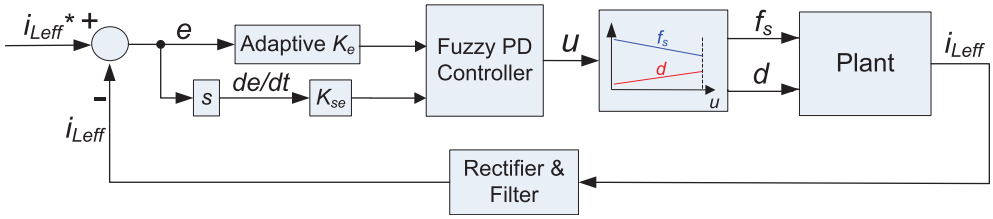

Figure 6.5: Current mode fuzzy control block diagram of LCC resonant converter

order to improve the control performance, an adaptive gain k_e is developed for e based on the given i^*_{Leff}.

The resulting CPM fuzzy PD control block diagram is shown in Fig. 6.5. An adaptive scaling gain k_e and a constant scaling gain k_{se} are developed for e and de/dt, respectively. It should be mentioned that de/dt can be easily derived in simulation, but in practice, an approximate sampling result depending on sampling rate is usually adopted. After regulated by k_e and k_{se}, the processed e and de/dt are fed into the fuzzy controller. The fuzzification procedure is then executed based on the membership functions, both inputs in real-valued space are transferred to a fuzzy space. Next, referring to the rule base and adopting the COG method, the control action is derived with inference mechanism. Through the defuzzification interface, the control action is transformed from a fuzzy space to a real-valued space and generates u, which is further transferred to the actual control variables: f_s and d. Measured i_{Leff} is feedback via appropriate filter and compared with i^*_{Leff} to complete the CPM fuzzy closed-loop [HBF11].

6.3 Simulated Results of Fuzzy PD Controller

Before the launch of the VLF high voltage generator prototype, simulated study about the fuzzy PD controller is implemented.

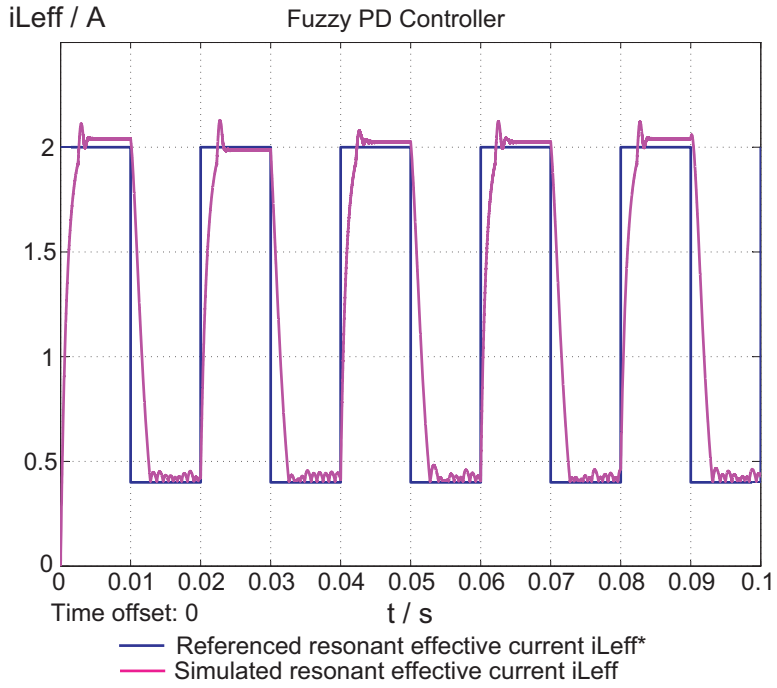

Figure 6.6: Simulated i_{Leff} under pulsing reference signal i^*_{Leff} with amplitude changes between 0.4 A and 2.0 A with 50 % duty cycle and 20 ms period. Refer to Fig. 5.8 and Fig. 7.7 for comparison.

Fig. 6.6 represents one of the results: the blue pulsing form i^*_{Leff} is provided, which has a changed amplitude between 0.4 A and 2.0 A with 50 % duty cycle, the pulsing period is 20 ms. The simulated red i_{Leff} tracks i^*_{Leff} and arrives the maximal amplitude in 3 ms with a spike and a little steady-state error; i_{Leff} tracks i^*_{Leff} and arrives the minimal amplitude in 3 ms with a little steady-state error and ripple. Generally speaking, the control performance is acceptable but not so satisfying.

Fig. 6.7 represents the other simulation results: the blue sinusoidal reference signal i^*_{Leff} is given, which has the amplitude from 0.3 A to 1.9 A with increasing frequency from 10 Hz to 100 Hz in 0.1 s. The simulated red i_{Leff} agrees well with

the sinusoidal reference signal i^*_{Leff} except a little deviation at the initial stage. The fuzzy PD controller has a good performance under the sinusoidal reference signal.

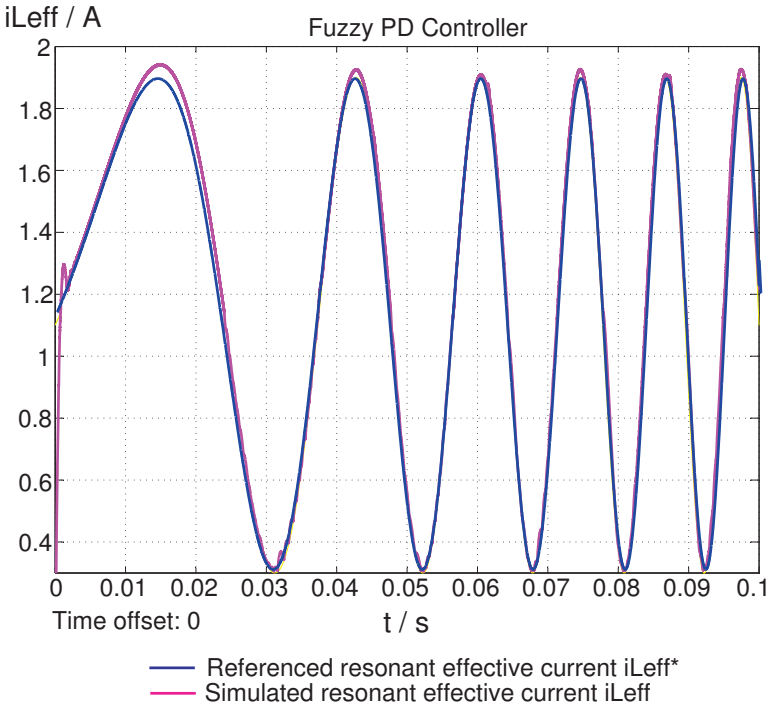

Figure 6.7: Simulated i_{Leff} under sinusoidal reference signal i^*_{Leff} with magnitudes change from 0.3 A to 1.9 A, and frequency changes from 10 Hz to 100 Hz in 100 ms. Refer to Fig. 5.9 and Fig. 7.8 for comparison.

6.4 Prototype Setup and Safety Issues of VLF HV Generator Prototype

A scaled-down VLF high voltage generator prototype is built for experimental validation, Fig. 6.8 represents the photo. Such equipment consists of an input DC power supply, a full-bridge power module, a central control card, a scaled-down VLF high voltage generator with a LCC tank and a two-stage asymmetrical CW multiplier, and a resistive high voltage output load.

The output voltage of the high voltage generator u_o has a theoretical maximal DC value of 10 kV, its highest transient value may be 20 kV; the output current

of the high voltage generator i_{cw} has the maximal average value of 40 mA; and the effective resonant current i_{Leff} in power module is about 3 A, its maximal peak value is about 5 A.

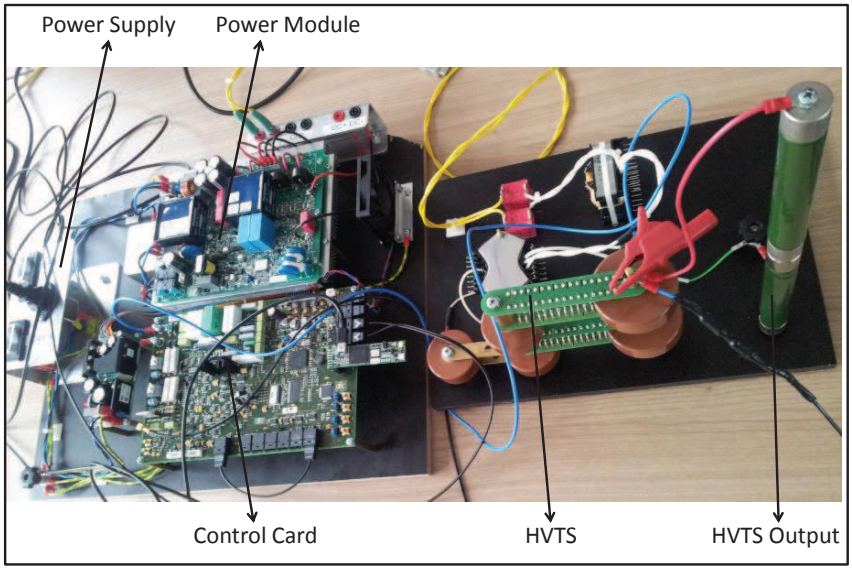

Figure 6.8: Scaled-down VLF HV generator prototype without protection cage

With above specifications, a potential shock danger could occur in case of incorrect connection, missing grounding, or improper manipulation of the control card. In order to prevent accidents, two grounded protection cages are installed to house the low voltage part and the high voltage part, respectively. The schematic diagram of the installation is provided in Fig. 6.9. As shown in which, each component of the prototype is marked with blue, the connections between them are denoted with black solid lines. The green, red and yellow areas indicate that the voltage in the region has the various voltage level, respectively. For example, the green area denotes the voltage around the control card is up to DC $\pm$15 V, and the red area indicates the voltage around the power module is up to 365 V, both of them are circled with the low voltage protection cage; while the yellow area denotes the voltage around the LCC tank, CW multiplier, output load and the voltage divider for measurement is up to DC 10 kV, which are circled with the

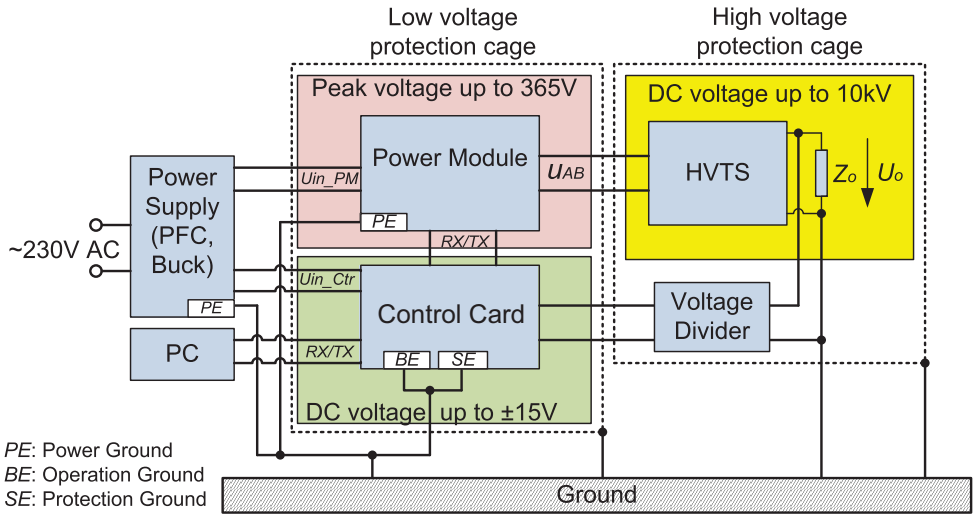

Figure 6.9: High voltage test equipment block diagram

high voltage protection cage. PE, BE, SE are defined as the power ground, the operation ground and the protection ground, respectively. Obviously, all kinds of grounds and protection cages are connected with earth.

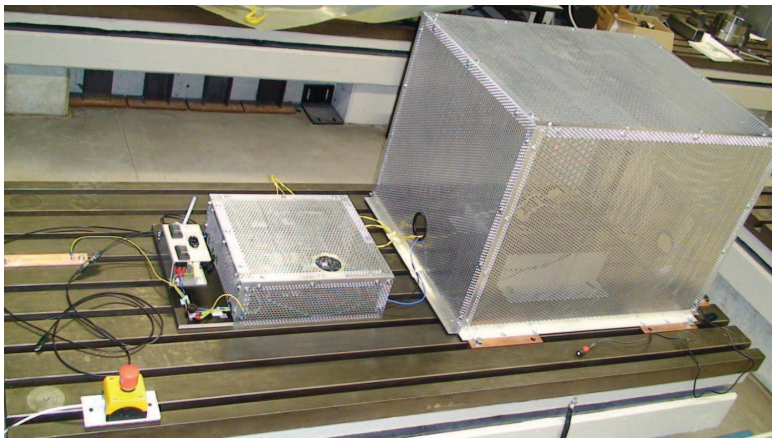

Figure 6.10: Scaled-down VLF HV generator prototype with mounted protection cages

Fig. 6.10 represents the photo of the scaled-down VLF HV generator prototype with two protection cages. It should be ensured that before contacting the high voltage parts, the power supply is shut down and the high voltage parts are

discharged and grounded.

6.5 Real-Time Implementation Issues of Fuzzy PD Controller

A. Controller Code Optimization

In order to reduce the computation time of the fuzzy control output under given inputs, the fuzzy controller code is optimized. Originally, in order to obtain the fuzzy PD controller output $u(t)$, according to the given $e(t)$ and $de(t)/dt$ inputs, the following steps would be followed based on the representation of Fig. 6.3:

1. Compute the certainty value of each membership function of $e(t)$ and $de(t)/dt$, such as $\mu_i(e(t))$ and $\mu_j(de(t)/dt)$ for all i, j, $0 \leq i \leq 8$, $0 \leq j \leq 8$;

2. Compute $\min(\mu_i(e(t)), \mu_j(de(t)/dt))$ for all i, j to obtain the certainty value of the corresponding membership function of $u(t)$: $\mu_k(u(t))$, $0 \leq k \leq 8$,;

3. According to the membership functions of $u(t)$ and the obtained $\mu_k(u(t))$, get the center real value of $\mu_k(u(t))$: b_k, and derive the area under the membership function $\mu_k(u(t))$: $S(\mu_k(u(t)))$;

4. Based on known b_k and $S(\mu_k(u(t)))$, calculate the ultimate fuzzy controller output $u(t)$ with COG method: u^{crisp}.

From above procedure, it can be seen that such computation needs to sweep each membership functions of $e(t)$, $de(t)/dt$ and $u(t)$ to obtain corresponding $\mu_i(e(t))$, $\mu_j(de(t)/dt)$ and $\mu_k(u(t))$ for all i, j, k. The ultimate control action u^{crisp} is based on obtained b_k and $S(\mu_k(u(t)))$ for all k. During such process, i, j, k is swept from 0 to 8, respectively.

In order to optimize the controller code, let's look into Fig. 6.2 again: since the membership functions of $e(t)$, $de(t)/dt$ and $u(t)$ are all adopt symmetrical triangle form, with arbitrary $e(t)$ or $de(t)/dt$ fuzzy inputs, there are never more than two membership functions of $e(t)$ or $de(t)/dt$ activating, the resulting activated $u(t)$ membership functions should not exceed than four. Since the inactivated $u(t)$ membership functions certainty have zero values and would have no impact

on the ultimate computation of the fuzzy control output, it is possible to optimize the controller code with only considering the activated $\mu_i(e(t))$, $\mu_j(de(t)/dt)$ and nonzero $\mu_k(u(t))$. That is to say, there has at most four values of b_k and $S(\mu_k(u(t)))$ are calculated and adopted for the final COG computation in the optimized code. This action can minimize the computational complexity and reduce the computation time dominantly [PY97].

B. Membership Functions and Rule Base Reduction

It is important to note that the problem with the efficiency of the code highlighted above become particularly acute when the fuzzy controller has more inputs and each input has many membership functions, since the number of rules increases exponentially with an increase of the number of inputs or an increase of the number of membership functions.

output $u(t)$		error $e(t)$				
		0	1	2	3	4
error derivative $de(t)/dt$	0	0	0	1	2	8
	1	0	2	2	4	8
	2	0	2	4	6	8
	3	0	4	6	6	8
	4	0	6	7	8	8

Table 6.2: Reduced rule base of fuzzy PD controller

As shown in Table 6.1 and Fig. 6.2, the two-input fuzzy PD controller with 9 membership functions for each input, has totally $9^2 = 81$ rules. During the execution of the controller code, such 81 rules need to be loaded in the DSP memory in each operation cycle, which increases the computation time and demands large memory size. Since the number of the fuzzy inputs cannot be decreased again, it is reasonable to decrease the number of the membership functions for each input.

As shown in Table 6.2 and Fig. 6.11, the original 9×9 rule base is reduced to 5×5 rule base, the corresponding number of membership functions for $e(t)$, $de(t)/dt$ and $u(t)$ are all reduced to 5. With such reduction, the two-input fuzzy PD controller has presently $5^2 = 25$ rules, which is less than a third of the original 81 rule numbers and needs less than a third of the original memory size.

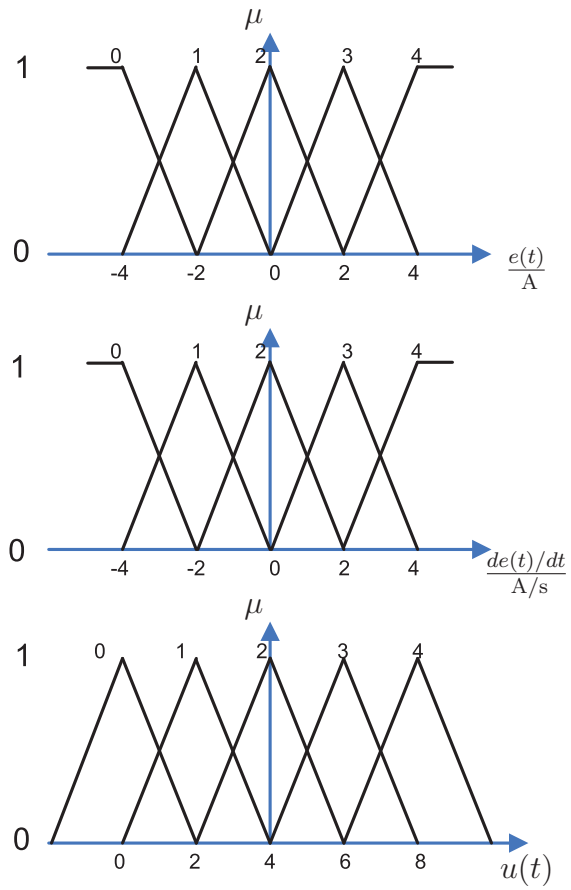

Figure 6.11: Reduced membership functions of the fuzzy PD controller

Experiments show that above actions are effective to solve the real-time implementation issues of the fuzzy PD controller on the prototype with an economic DSP. The optimized controller code with reduced membership functions and rule base are doing well to verify the theoretical controller design.

6.6 Experimental Results of CPM Fuzzy PD Controller

In order to verify both the duty-cycle control mode and the frequency control mode, and also considering the safety issue, a scaled-down input DC voltage: $u_{in} = 30V$, is adopted for the measurement. Fig. 6.12 provides the experimental

results with specified i^*_{Leff} at 0.2 A. The corresponding main waveforms of the LCC resonant converter, such as $i_L(t)$ in Ch1 channel, $u_o(t)$ in Ch2 channel, $u_s(t)$ in Ch3 channel and $u_{AB}(t)$ in Ch4 channel are represented.

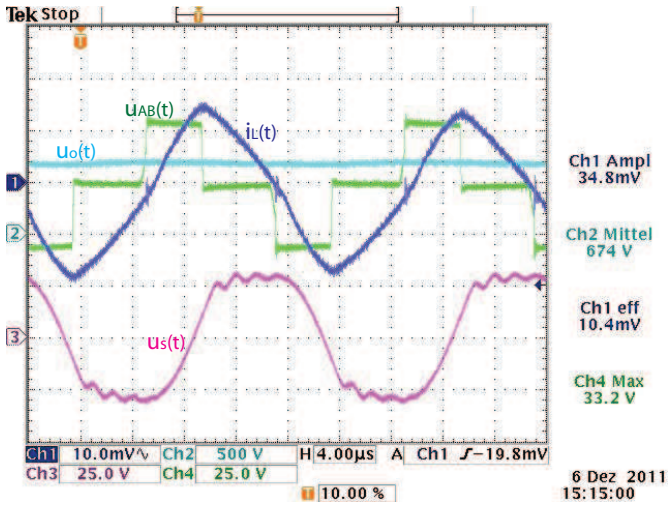

Figure 6.12: Experimental results of fuzzy PD controller with reference effective resonant current $i^*_{Leff} = 0.2$ A, $U_{in} = 30$ V; current probe is set as 200 mA/div; Ch1 (blue) is $i_L(t)$; Ch2 (light blue) is $u_o(t)$; Ch3 (purple) is $u_s(t)$; Ch4 (green) is $u_{AB}(t)$.

The actual resonant effective current i_{Leff} can be derived from the measured $i_L(t)$ with consideration of oscilloscope setup: 10.0 mV/div and current probe setup: 200 mA/div.

$$i_{Leff} = \frac{10.4 \text{ mV}}{10 \text{ mV/div}} \times 200 \text{ mA/div} = 208 \text{ mA} \approx 0.208 \text{ A} \tag{6.5}$$

$$e_{iLeff} = \frac{0.208 \text{ A} - 0.2 \text{ A}}{0.2 \text{ A}} \times 100 \text{ \%} = 4 \text{ \%} \tag{6.6}$$

It can be seen that the experimental resonant effective current $i_{Leff}(0.208 \text{ A})$ agrees with the given reference resonant effective current $i^*_{Leff}(0.2 \text{ A})$ except a little deviation. The average steady-state deviation is about 4 %. Such experimental results validate the correctness of the fuzzy PD control design.

6.7 Summary

Based on the simulated and experimental results, the conclusions can be drawn that the development of the conventional fuzzy PD controller is successful: the simulated closed loop results verify its correctness, the experimental results further validate its feasibility and robustness.

But when comparing above results (Fig. 6.6, Fig. 6.7) with those of the linear PI controller (Fig. 5.8, Fig. 5.9), the model-free fuzzy controller has no dominant advantages regarding the settling time, the static error or the control bandwidth. Actually, the conventional fuzzy controller suffers always from the criticism due to the lack of the systematic stability analysis and controller design. A further research and development of a nonlinear model-based controller is expected.

Chapter 7

Model-Based Fuzzy Control Design

7.1 Introduction

In the past ten years or so, prevailing research efforts on fuzzy logic control have been devoted to model-based fuzzy control systems, that guarantee not only stability but also the performance of the closed-loop fuzzy control systems.

Takagi-Sugeno (T-S) model-based fuzzy control is developed based on the Takagi-Sugeno fuzzy model [TS85], also called the Type-III fuzzy model by Sugeno [Sug99], is in fact a fuzzy dynamic model [N.N95] [N.N97a] [N.N97b]. This model is based on using a set of fuzzy rules to describe a global nonlinear system in terms of a set of local linear models which are smoothly connected by fuzzy membership functions. This fuzzy modeling method offers an alternative approach to describing complex nonlinear systems [N.N97a] [FR96] [JSMS00] [TW01] [N.N98] [ZZX00], and drastically reduces the number of rules in modeling higher order nonlinear systems [Sug99]. Consequently, Takagi-Sugeno fuzzy models are less prone to the curse of dimensionality than other fuzzy models. More importantly, Takagi-Sugeno fuzzy models provide a basis for development of systematic approaches to stability analysis and controller design of fuzzy control systems in view of powerful conventional control theory and techniques [Fen06].

A great number of theoretical results on function approximation, stability analysis, and controller synthesis have been developed for Takagi-Sugeno fuzzy models during the last ten years or so. T-S fuzzy models are shown to be univer-

sal function approximators in the sense that they are able to approximate any smooth nonlinear functions to any degree of accuracy in any convex compact region [N.N97a] [FR96] [JSMS00] [TW01] [N.N98] [ZZX00].

The basic idea of the T-S model-based fuzzy control design is to design a feedback controller for each local model and to construct a global controller from the local controllers in such a way that global stability of the closed-loop fuzzy control system is guaranteed. The major techniques that have been used include quadratic stabilization, linear matrix inequalities (LMIs), Lyapunov stability theory, bilinear matrix inequalities, and so on [Fen06].

7.2 Takagi-Sugeno (T-S) Fuzzy Model and Parallel Distributed Compensation (PDC)

A. Takagi-Sugeno (T-S) Fuzzy Model

Takagi-Sugeno (T-S) fuzzy model adopts a set of fuzzy rules to describe a global nonlinear system in terms of a set of local linear models which are smoothly connected by fuzzy membership functions.

For example, selecting M operating points $(\mathbf{x}_i(t), \mathbf{u}_i(t))$, $i = 1, \ldots, M$ for a nonlinear system: $\dot{\mathbf{x}}(t) = f(\mathbf{x}(t), \mathbf{u}(t))$, based on the general control design process represented in Appendix F, the M Lyapunov-linearized open-loop small-signal models are shown in Eq. 7.1.

$$\delta\dot{\mathbf{x}} = \mathbf{A}_i \cdot \delta\mathbf{x} + \mathbf{B}_i \cdot \delta\mathbf{u}, i = 1, \ldots, M. \tag{7.1}$$

The small-signal model around an intermediate operating point can then be derived based on the known M linear small-signal models. Based on such concept, the fuzzy model proposed by Takagi and Sugeno is described by fuzzy IF-THEN rules, which represent local linear input-output relations of a nonlinear system. The main feature of a Takagi-Sugeno fuzzy model is to express the local dynamics of each fuzzy implication (rule) by a linear system model. The overall fuzzy model of the system is achieved by fuzzy "blending" of the linear system models [TW01]. The ith rule of the fuzzy system is of the following form:

Model rule i:

IF $z_1(t)$ is N_{i1}, ..., and $z_p(t)$ is N_{ip},

THEN $\dot{\mathbf{x}} = \mathbf{A}_i \cdot \mathbf{x}(t) + \mathbf{B}_i \cdot \mathbf{u}(t), i = 1, \ldots, M$.

Here, N_{ij} is the fuzzy set, and M is the number of model rules; $\mathbf{x}(t)$ is the state vector and $\mathbf{u}(t)$ is the input vector; $z_1(t)$, . . . , $z_p(t)$ are known premise variables that may be functions of the state variables, external disturbances, and/or time. We will use $\mathbf{z}(t)$ to denote the vector containing all the individual elements: $z_1(t)$, . . . , $z_p(t)$. Each linear consequent equation represented by $\mathbf{A}_i \cdot \mathbf{x}(t) + \mathbf{B}_i \cdot \mathbf{u}(t)$ is called a "subsystem" [TW01].

Given a pair of $(\mathbf{x}(t), \mathbf{u}(t))$, the final output of a continous-time fuzzy system is inferred as follows:

$$\dot{\mathbf{x}} = \frac{\sum_{i=1}^{M} w_i(\mathbf{z}(t)) \cdot [\mathbf{A}_i \cdot \mathbf{x}(t) + \mathbf{B}_i \cdot \mathbf{u}(t)]}{\sum_{i=1}^{M} w_i(\mathbf{z}(t))}. \tag{7.2}$$

where $\mathbf{z}(t) = [z_1(t), z_2(t), ..., z_p(t)]$, $w_i(\mathbf{z}(t)) = \prod_{j=1}^{p} N_{ij}(z_j(t))$, for all t. The term $N_{ij}(z_j(t))$ is the grade of membership of $z_j(t)$ in N_{ij}.

Since $\sum_{i=1}^{M} w_i(\mathbf{z}(t)) > 0$, $w_i(\mathbf{z}(t)) \geq 0, i = 1, \ldots, M$,

we have $\sum_{i=1}^{M} \frac{w_i(\mathbf{z}(t))}{\sum_{i=1}^{M} w_i(\mathbf{z}(t))} = 1$, $\frac{w_i(\mathbf{z}(t))}{\sum_{i=1}^{M} w_i(\mathbf{z}(t))} \geq 0, i = 1, \ldots, M$, for all t.

B. Parallel Distributed Compensation (PDC)

The concept of parallel distributed compensation (PDC) [TS92b] [TS92a] [TS93] is utilized to design fuzzy controllers for stabilizing the fuzzy system Eq. 7.2. The history of the so-called PDC began with a model-based design procedure proposed by Kang and Sugeno [SK86]. The design procedure was improved and the stability of the control systems was analyzed in [TS92c]. The PDC [TS92c] [WTG95b] [WTG95a] offers a procedure to design a fuzzy controller from a given T-S fuzzy model. The idea is to design a compensator for each rule of the T-S fuzzy model, and realize a multiple control with automatic switching via fuzzy logic rules. The designed fuzzy controller shares the same fuzzy sets with the fuzzy model in the premise parts. With PDC scheme, the design procedure is conceptually simple and natural. The stability analysis and control design problems can be reduced to linear matrix inequality (LMI) problems, where powerful

numerical algorithms [ea94] can be applied. Fig. 7.1 shows the concept of PDC design.

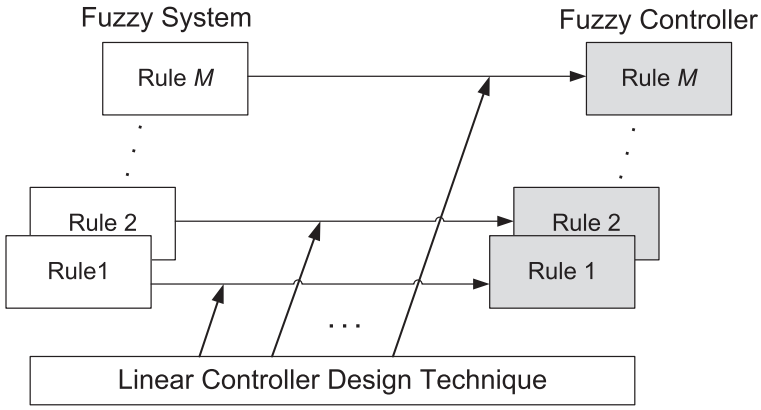

Figure 7.1: Parallel Distributed Compensation (PDC)

For the fuzzy model Eq. 7.2, the following fuzzy controller via the PDC is constructed:

Control rule i:

IF $z_1(t)$ is N_{i1}, ..., and $z_p(t)$ is N_{ip},

THEN $\mathbf{u}(t) = \text{-}\mathbf{K}_i \cdot \mathbf{x}(t), i = 1, \ldots, M.$

The overall fuzzy controller is represented in Eq. 7.3, the fuzzy controller design is to determine the local feedback gains K_i, $i = 1, \ldots, M$.

$$\mathbf{u} = -\frac{\sum_{i=1}^{M} w_i(\mathbf{z}(t)) \cdot [\mathbf{K}_i \cdot \mathbf{x}(t)]}{\sum_{i=1}^{M} w_i(\mathbf{z}(t))}. \tag{7.3}$$

By inserting Eq. 7.3 into Eq. 7.2, the closed-loop fuzzy control system can be inferred, as shown in Eq. 7.4.

$$\dot{\mathbf{x}} = \frac{\sum_{i=1}^{M} \sum_{j=1}^{M} w_i(\mathbf{z}(t)) w_j(\mathbf{z}(t)) \cdot [\mathbf{A}_i - \mathbf{B}_i \cdot \mathbf{K}_j] \cdot \mathbf{x}(t)}{\sum_{i=1}^{M} \sum_{j=1}^{M} w_i(\mathbf{z}(t)) w_j(\mathbf{z}(t))} \tag{7.4}$$

where

$$\sum_{i=1}^{M} \sum_{j=1}^{M} w_i(\mathbf{z}(t)) w_j(\mathbf{z}(t)) = \sum_{i=1}^{M} w_i(\mathbf{z}(t)) = 1 \tag{7.5}$$

7.3 Stability Analysis via Lyapunov Approach

A sufficient stability condition for the closed-loop fuzzy control system Eq. 7.4, which is derived by Tanaka and Sugeno [TS92c], is expressed in the form of linear matrix inequalities (LMIs) [ea94]. The equilibrium of a continuous-time fuzzy control system Eq. 7.4 is asymptotically stable in the large if there has a common positive definite matrix $\mathbf{P}$, such that the following two conditions are satisfied:

$$(\mathbf{A}_i - \mathbf{B}_i\mathbf{K}_i)^T \cdot \mathbf{P} + \mathbf{P} \cdot (\mathbf{A}_i - \mathbf{B}_i\mathbf{K}_i) < 0, i = 1, \ldots, M \tag{7.6}$$

$$(\mathbf{G}_{ij})^T \cdot \mathbf{P} + \mathbf{P} \cdot \mathbf{G}_{ij} < 0, i < j \leq M \tag{7.7}$$

where

$$\mathbf{G}_{ij} = \frac{(\mathbf{A}_i - \mathbf{B}_i\mathbf{K}_j) + (\mathbf{A}_j - \mathbf{B}_j\mathbf{K}_i)}{2}, i < j \leq M$$

The control problem is to select a common positive definite matrix $\mathbf{P}$, such that conditions Eq. 7.6 and Eq. 7.7 are satisfied. It has long been considered difficult, a controller for each rule has to be designed and checked whether the stability conditions are satisfied, most of the time a trial-and-error type of procedure is used [TS92c]. Nowadays, the convex programming techniques are usually adopted to solve this feasibility problem [NN94].

7.4 Model Reduction of LCC Resonant Converter

In order to simplify the model-based T-S fuzzy controller design process, a further model reduction based on the linear forth-order small-signal model: Eq. 3.56 and Eq. 3.57, are considered.

The symbolic model reduction for a nonlinear model is difficult and impossible, but the multitude of numerical model reduction techniques can be performed with the linearized models. The balanced truncation method is one of the most common model reduction schemes, which is first introduced by Mullis and Roberts in 1976 and later proposed by Moore in the systems and control literature in 1981 [Moo81]. This method provides a good approximation to the original system at

high frequencies, i.e. the transient response of the reduced-order model matches better [DJCW08].

As an introduction, let the following linear time invariant dynamical system be the to-be-reduced model [GA04]:

$$\begin{aligned} \begin{bmatrix} \dot{\mathbf{x}} \\ \dot{\mathbf{z}} \end{bmatrix} &= \mathbf{A} \begin{bmatrix} \mathbf{x} \\ \mathbf{z} \end{bmatrix} + \mathbf{B}\mathbf{u}, \\ \mathbf{y} &= \mathbf{C} \begin{bmatrix} \mathbf{x} \\ \mathbf{z} \end{bmatrix} + \mathbf{E}\mathbf{u}, \end{aligned} \tag{7.8}$$

$$\Longleftrightarrow$$

$$\mathbf{G(s)} = \left[\begin{array}{c:c} \mathbf{A} & \mathbf{B} \\ \hdashline \mathbf{C} & \mathbf{E} \end{array}\right] \in \Re^{(n+p)(n+m)}, \tag{7.9}$$

where $\mathbf{x} \in \Re^r$, $\mathbf{z} \in \Re^{n-r}$, $r < n$. Closely related to this system are two continuous-time Lyapunov equations:

$$\mathbf{A} \cdot \mathbf{P} + \mathbf{P} \cdot \mathbf{A}^T + \mathbf{B} \cdot \mathbf{B}^T = 0, \tag{7.10}$$

$$\mathbf{A}^T \cdot \mathbf{Q} + \mathbf{Q} \cdot \mathbf{A} + \mathbf{C}^T \cdot \mathbf{C} = 0. \tag{7.11}$$

Under the assumptions that the system $\mathbf{G(s)}$ is asymptotically stable and minimal, the above equations have unique symmetric positive definite solutions $\mathbf{P}$ and $\mathbf{Q}$, called the reachability and observability gramians, respectively. The square roots of the eigenvalues of the product $\mathbf{PQ}$ are the so-called Hankel singular values $\sigma_i(\mathbf{G(s)}) = \sqrt{\lambda_i(\mathbf{PQ})}$.

Let the system $\mathbf{G(s)}$ has the Lyapunov balanced realization:

$$\mathbf{G(s)} = \left[\begin{array}{c:c} \mathbf{A} & \mathbf{B} \\ \hdashline \mathbf{C} & \mathbf{E} \end{array}\right] = \left[\begin{array}{cc:c} \mathbf{A}_{11} & \mathbf{A}_{12} & \mathbf{B}_1 \\ \mathbf{A}_{21} & \mathbf{A}_{22} & \mathbf{B}_2 \\ \hdashline \mathbf{C}_1 & \mathbf{C}_2 & \mathbf{E} \end{array}\right] \tag{7.12}$$

with $\mathbf{P} = \mathbf{Q} = diag(\Sigma_1, \Sigma_2)$, where $\Sigma_1 = diag(\sigma_1, ...\sigma_r)$, $\Sigma_2 = diag(\sigma_{r+1}, ...\sigma_n)$, and $\sigma_1 > \sigma_2 > ... > \sigma_n > 0$, $\sigma_r \gg \sigma_{r+1}$. Then the reduced order model

$$\mathbf{G}_r(s) = \left[\begin{array}{c:c} \mathbf{A}_{11} & \mathbf{B}_1 \\ \hdashline \mathbf{C}_1 & \mathbf{E} \end{array}\right] \tag{7.13}$$

obtained by truncation is asymptotically stable, minimal and satisfies: $\|\mathbf{G}(s) - \mathbf{G}_r(s)\|_\infty \leq 2(\sigma_{r+1} + \cdots + \sigma_n)$ [DJCW08][GA04].

Based on Eq. 3.56 and Eq. 3.57, the linearized forth-order small-signal model can be rewritten as the following form:

$$\delta\dot{\mathbf{x}_n} = \mathbf{A}_{un} \cdot \delta\mathbf{x}_n + \mathbf{B}_{un} \cdot \delta\mathbf{u}_n \tag{7.14}$$

$$\delta\mathbf{y}_n = \mathbf{C}_{un} \cdot \delta\mathbf{x}_n \tag{7.15}$$

where

$$\mathbf{A}_{un} = \left[\begin{array}{cc:cc} a_{11n} & a_{12n} & a_{13n} & 0 \\ a_{21n} & a_{22n} & 0 & a_{24n} \\ \hdashline a_{31n} & 0 & 0 & a_{34n} \\ 0 & a_{42n} & a_{43n} & 0 \end{array}\right] = \left[\begin{array}{c:c} \mathbf{A}_r & \mathbf{A}_{12} \\ \hdashline \mathbf{A}_{21} & \mathbf{A}_{22} \end{array}\right] \tag{7.16}$$

$$\mathbf{B}_{un} = \left[\begin{array}{cc} b_{12n} & b_{13n} \\ 0 & b_{23n} \\ \hdashline 0 & b_{33n} \\ 0 & b_{43n} \end{array}\right] = \left[\begin{array}{c} \mathbf{B}_r \\ \hdashline \mathbf{B}_2 \end{array}\right] \tag{7.17}$$

$$\mathbf{C}_{un} = \left[\begin{array}{cc:cc} c_{31n} & c_{32n} & 0 & 0 \end{array}\right] = \left[\begin{array}{c:c} \mathbf{C}_r & \mathbf{C}_2 \end{array}\right] \tag{7.18}$$

$$\delta\mathbf{x}_n = \left[\delta i_{Lsn}, \delta i_{Lcn}, \delta u_{ssn}, \delta u_{scn}\right] \tag{7.19}$$

$$\delta\mathbf{u}_n = \left[\delta d, \delta f_{sn}\right] \tag{7.20}$$

$$\delta\mathbf{y}_n = \left[\delta i_{Lpn}\right] \tag{7.21}$$

Among which, δu_{in} is not included in $\delta\mathbf{u}_n$ since it is regarded as a constant; δi_{cwn} is not considered as an output variable. By adopting above Lyapunov balanced truncation method, the resulting reduced-order dynamic model is obtained, as shown in Eq. 7.22. Refer to Appendix G for the continuous Lyapunov equation solutions and the eignvalues.

$$\delta\dot{\mathbf{x}}_r = \mathbf{A}_r \cdot \delta\mathbf{x}_r + \mathbf{B}_r \cdot \delta\mathbf{u}_r, \tag{7.22}$$

$$\delta\mathbf{y}_r = \mathbf{C}_r \cdot \delta\mathbf{x}_r \tag{7.23}$$

where

$$\mathbf{A}_r = \begin{bmatrix} a_{11n} & a_{12n} \\ a_{21n} & a_{22n} \end{bmatrix}, \tag{7.24}$$

$$\mathbf{B}_r = \begin{bmatrix} b_{12n} & b_{13n} \\ 0 & b_{23n} \end{bmatrix}, \tag{7.25}$$

$$\mathbf{C}_r = \begin{bmatrix} c_{31n} & c_{32n} \end{bmatrix}, \tag{7.26}$$

$$\delta\mathbf{x}_r = \begin{bmatrix} \delta i_{Lsn} & \delta i_{Lcn} \end{bmatrix}, \tag{7.27}$$

$$\delta\mathbf{u}_r = \begin{bmatrix} \delta d & \delta f_{sn} \end{bmatrix}. \tag{7.28}$$

$$\delta\mathbf{y}_r = \begin{bmatrix} \delta i_{Lpn} \end{bmatrix}. \tag{7.29}$$

In order to verify such model reduction, a dynamic characteristics comparison between the LCC resonant converter model with a voltage source load (Eq. 3.56, Eq. 3.57) and the reduced model (Eq. 7.22, Eq. 7.23) is implemented. The corresponding control-to-resonant-current transfer functions are represented in Fig. 7.2 and Fig. 7.3. Among which, Fig. 7.2 shows the d-to-i_{Lpn} transfer functions, while Fig. 7.3 shows the f_{sn}-to-i_{Lpn} transfer functions. The blue lines present the transfer functions of the LCC resonant converter with a voltage source load, and the red lines represent the transfer functions of the second-order model.

From above d-to-i_{Lpn} transfer function and f_{sn}-to-i_{Lpn} transfer function comparisons, it can be seen that there exists a constant small deviation between their magnitudes (about 3 dB), their phases are nearly the same in most of the low frequency region, but has some deviation in high frequency region. Since the dynamic deviations between both models are in an acceptable tolerance range, the approximation of the forth-order LCC resonant converter dynamic model by the second-order model is thought to be reasonable, which enables a simpler and more effective model-based fuzzy control design.

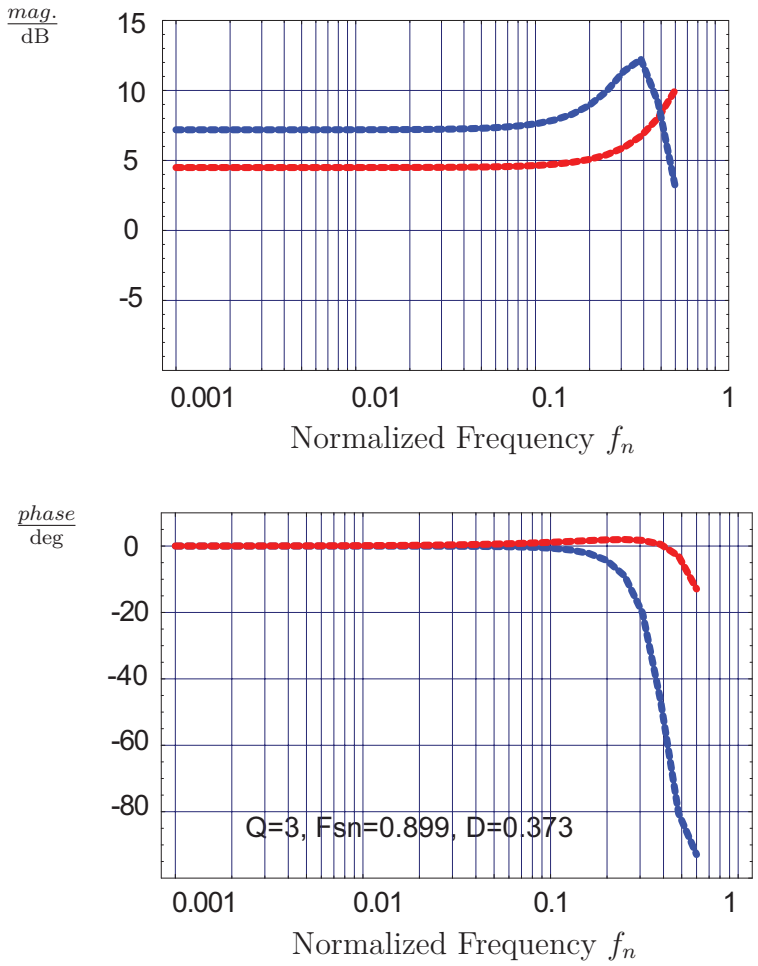

Figure 7.2: Comparison of d-to-i_{Lpn} transfer functions with voltage source load (blue) and the second-order model (red) with LCC resonant converter parameters: C_s=200 nF, C_p=50 nF, L_s=500 μH, R_s=1 Ω, C_L=10 nF

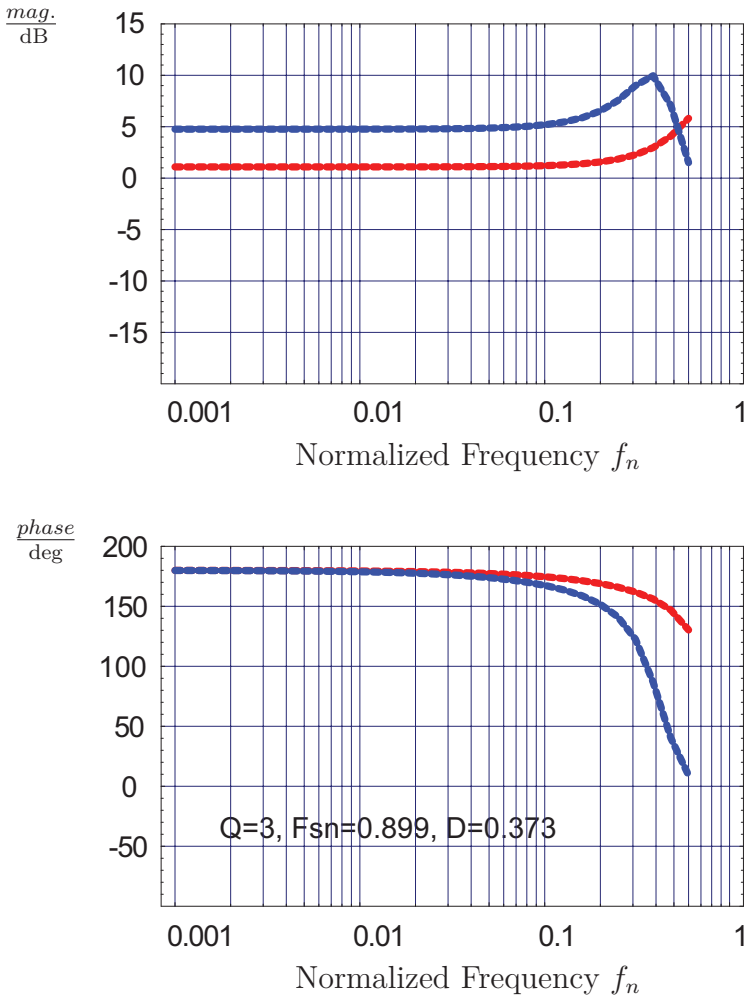

Figure 7.3: Comparison of f_{sn}-to-i_{Lpn} transfer functions with voltage source load (blue) and the second-order model (red) with LCC resonant converter parameters: C_s=200 nF, C_p=50 nF, L_s=500 μH, R_s=1 Ω, C_L=10 nF

7.5 T-S Fuzzy Control Design

Based on the second-order dynamic model, a model-based T-S fuzzy controller is developed for the LCC resonant converter.

As an example, a prototype with maximal resonant effective current 12 A is considered. In the complete operation region, four operating points are selected, Table 7.1 represents the corresponding steady-state parameters, such as the normalized load Q, normalized switching frequency F_{sn}, duty cycle D, and the corresponding I_{Lp} and I_{Leff}.

$Q = R_0/(Z * n^2 * k^2)$	$F_{sn} = F_s/f_0$	$D = Duty$	I_{LP}/A	I_{Leff}/A
3	0.899	0.373	4.63	3.27
10	1	0.5015	8.6	6.08
20	1.019	0.536	13.6	9.62
283	1.036	0.21	17	12

Table 7.1: Selected steady-state operating points

The membership function of i_{Leff} is shown in Fig. 7.4, which consists of four symmetrical triangles. Each center real value corresponds to the respective I_{Leff} of the operating point in Table 7.1. In this case, $a = 3$.

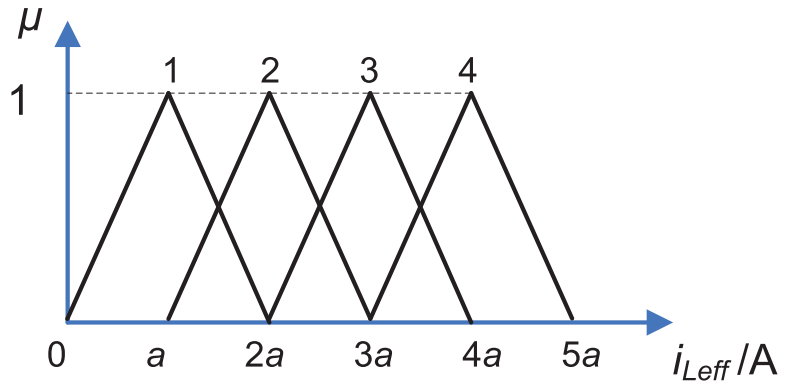

Figure 7.4: Membership functions of four-rule model

The model rules are represented below. The system matrices $\mathbf{A}_{ri}$ and $\mathbf{B}_{ri}$, i = 1,...,4, are obtained from the derived small-signal model in Chapter 3 and the selected operating points.

- Rule 1: IF $i_{Leff}(t)$ is "about a", THEN $\dot{\mathbf{x}}_r = \mathbf{A}_{r1} \cdot \mathbf{x}_r + \mathbf{B}_{r1} \cdot \mathbf{u}_r$;
- Rule 2: IF $i_{Leff}(t)$ is "about $2a$", THEN $\dot{\mathbf{x}}_r = \mathbf{A}_{r2} \cdot \mathbf{x}_r + \mathbf{B}_{r2} \cdot \mathbf{u}_r$;
- Rule 3: IF $i_{Leff}(t)$ is "about $3a$", THEN $\dot{\mathbf{x}}_r = \mathbf{A}_{r3} \cdot \mathbf{x}_r + \mathbf{B}_{r3} \cdot \mathbf{u}_r$;
- Rule 4: IF $i_{Leff}(t)$ is "about $4a$", THEN $\dot{\mathbf{x}}_r = \mathbf{A}_{r4} \cdot \mathbf{x}_r + \mathbf{B}_{r4} \cdot \mathbf{u}_r$.

where

$$\mathbf{A}_{r1} = \begin{bmatrix} -0.4038 & 0.8285 \\ -0.7934 & -0.0097 \end{bmatrix}$$

$$\mathbf{A}_{r2} = \begin{bmatrix} -0.6682 & 0.8650 \\ -0.6438 & -0.0275 \end{bmatrix}$$

$$\mathbf{A}_{r3} = \begin{bmatrix} -0.7572 & 0.8636 \\ -0.4632 & -0.0625 \end{bmatrix}$$

$$\mathbf{A}_{r4} = \begin{bmatrix} -0.1999 & 0.7759 \\ -0.0063 & -0.7847 \end{bmatrix}$$

$$\mathbf{B}_{r1} = \begin{bmatrix} 1.666 & -0.9582 \\ 0 & -0.9091 \end{bmatrix}$$

$$\mathbf{B}_{r2} = \begin{bmatrix} 1.4109 & -0.9045 \\ 0 & -2.6444 \end{bmatrix}$$

$$\mathbf{B}_{r3} = \begin{bmatrix} 1.332 & -0.8978 \\ 0 & -5.0773 \end{bmatrix}$$

$$\mathbf{B}_{r4} = \begin{bmatrix} 1.892 & -5.956 \\ 0 & -0.7182 \end{bmatrix}$$

The four-rule T-S fuzzy model is inferred as follows

$$\dot{\mathbf{x}}_r = \frac{\sum_{i=1}^{4} w_i(i_{Leff}) \cdot [\mathbf{A}_{ri} \cdot \mathbf{x}_r + \mathbf{B}_{ri} \cdot \mathbf{u}_r]}{\sum_{i=1}^{4} w_i(i_{Leff})}, \tag{7.30}$$

where $w_i(i_{Leff})$ is the certainty of each membership function.

Based on the four-rule T-S fuzzy model Eq. 7.30, the corresponding four-rule PDC fuzzy controller can be obtained:

- Rule 1: IF $i_{Leff}(t)$ is "about a", THEN $\mathbf{u}_r = -K_1 \cdot \mathbf{x}_r$,

- Rule 2: IF $i_{Leff}(t)$ is "about $2a$" THEN $\mathbf{u}_r = -K_2 \cdot \mathbf{x}_r$,
- Rule 3: IF $i_{Leff}(t)$ is "about $3a$", THEN $\mathbf{u}_r = -K_3 \cdot \mathbf{x}_r$,
- Rule 4: IF $i_{Leff}(t)$ is "about $4a$", THEN $\mathbf{u}_r = -K_4 \cdot \mathbf{x}_r$,

that is

$$\mathbf{u}_r = -\frac{\sum_{i=1}^{4} w_i(i_{Leff})[\mathbf{K}_i \mathbf{x}_r]}{\sum_{i=1}^{4} w_i(i_{Leff})}. \tag{7.31}$$

By combining the T-S fuzzy model: Eq. 7.30 and the PDC controller: Eq. 7.31, the model-based closed-loop fuzzy control system can be obtained:

$$\dot{\mathbf{x}}_r = \frac{\sum_{i=1}^{4}\sum_{j=1}^{4} w_i(i_{Leff}) w_j(i_{Leff})[\mathbf{A}_{ri} - \mathbf{B}_{ri}\mathbf{K}_j]\mathbf{x}_r}{\sum_{i=1}^{4}\sum_{j=1}^{4} w_i(i_{Leff}) w_j(i_{Leff})} \tag{7.32}$$

where

$$\sum_{i=1}^{4}\sum_{j=1}^{4} w_i(i_{Leff}) w_j(i_{Leff}) = \sum_{i=1}^{4} w_i(i_{Leff}) = 1 \tag{7.33}$$

Sufficient stability condition for the continuous-time fuzzy control system Eq. 7.32 is given below [TTW97] [THW03]: The equilibrium of a fuzzy control system Eq. 7.32 is asymptotically stable in the large if there exists a common positive definite matrix $\mathbf{P}$ such that the following two conditions are satisfied:

$$(\mathbf{A}_{ri} - \mathbf{B}_{ri}\ \mathbf{K}_i)^T\ \mathbf{P} + \mathbf{P}\ (\mathbf{A}_{ri} - \mathbf{B}_{ri}\ \mathbf{K}_i) < 0 \text{ for } i = 1, 2, 3, 4. \tag{7.34}$$

$$\mathbf{G}_{ij}^T\ \mathbf{P} + \mathbf{P}\ \mathbf{G}_{ij} < 0 \text{ for } i < j \leq 4 \tag{7.35}$$

where

$$\mathbf{G}_{ij} = \frac{(\mathbf{A}_{ri} - \mathbf{B}_{ri}\ \mathbf{K}_j) + (\mathbf{A}_{rj} - \mathbf{B}_{rj}\ \mathbf{K}_i)}{2} \tag{7.36}$$

The control problem is to select the common positive definite matrix $\mathbf{P}$, such that conditions Eq. 7.34 and Eq. 7.35 are satisfied. Based on the second-order dynamic model Eq. 7.22, a simple approach introduced in [KTIT92] is adopted for finding the common positive definite matrix $\mathbf{P}$.

For given closed loop eigenvalues [-2, -1], the feedback matrix $\mathbf{K}_i$ can be obtained according to given $\mathbf{A}_{ri}$ and $\mathbf{B}_{ri}$ $(i = 1, 2, 3, 4)$, as shown below:

$$\mathbf{K}_1 = \begin{bmatrix} 1.55211 & -0.9936 \\ 0 & 0 \end{bmatrix},$$

$$\mathbf{K}_2 = \begin{bmatrix} 0 & 0 \\ -0.2057 & -0.8010 \end{bmatrix},$$

$$\mathbf{K}_3 = \begin{bmatrix} 0 & 0 \\ -0.02094 & -0.4257 \end{bmatrix},$$

$$\mathbf{K}_4 = \begin{bmatrix} 0 & 0 \\ -0.1591 & -0.1487 \end{bmatrix},$$

and the matrices $\mathbf{G}_{ij}$ can also be derived, which are all Hurwitz matrices.

$$\mathbf{G}_{12} = \begin{bmatrix} -1.7295 & 1.16394 \\ -0.81207 & -0.3827 \end{bmatrix},$$

$$\mathbf{G}_{23} = \begin{bmatrix} -0.8145 & 0.312258 \\ -1.10341 & -2.64134 \end{bmatrix},$$

$$\mathbf{G}_{34} = \begin{bmatrix} -0.612316 & -0.514689 \\ -0.7139 & -2.32977 \end{bmatrix}.$$

Since the condition Eq. 7.34 and Eq. 7.35 can be equalized as the following matrix inequalities:

$$(\mathbf{A}_{r1} - \mathbf{B}_{r1}\ \mathbf{K}_1)^T\ \mathbf{P} + \mathbf{P}\ (\mathbf{A}_{r1} - \mathbf{B}_{r1}\ \mathbf{K}_1) < 0, \tag{7.37}$$

$$(\mathbf{A}_{r2} - \mathbf{B}_{r2}\ \mathbf{K}_2)^T\ \mathbf{P} + \mathbf{P}\ (\mathbf{A}_{r2} - \mathbf{B}_{r2}\ \mathbf{K}_2) < 0, \tag{7.38}$$

$$(\mathbf{A}_{r3} - \mathbf{B}_{r3}\ \mathbf{K}_3)^T\ \mathbf{P} + \mathbf{P}\ (\mathbf{A}_{r3} - \mathbf{B}_{r3}\ \mathbf{K}_3) < 0, \tag{7.39}$$

$$(\mathbf{A}_{r4} - \mathbf{B}_{r4}\ \mathbf{K}_4)^T\ \mathbf{P} + \mathbf{P}\ (\mathbf{A}_{r4} - \mathbf{B}_{r4}\ \mathbf{K}_4) < 0, \tag{7.40}$$

$$\mathbf{G}_{12}^T\ \mathbf{P} + \mathbf{P}\ \mathbf{G}_{12} < 0, \tag{7.41}$$

$$\mathbf{G}_{23}^T\ \mathbf{P} + \mathbf{P}\ \mathbf{G}_{23} < 0, \tag{7.42}$$

$$\mathbf{G}_{34}^T\ \mathbf{P} + \mathbf{P}\ \mathbf{G}_{34} < 0, \tag{7.43}$$

by assuming the common positive definite matrix $\mathbf{P}$ has the following form [KTIT92]:

$$\mathbf{P} = \begin{bmatrix} p_1 & 1 \\ 1 & p_2 \end{bmatrix} \text{ with } p1 > 0, p_1 p_2 > 1 \tag{7.44}$$

and substituting the **P** matrix in Eq. 7.37 - Eq. 7.43 with the assigned **P** matrix form in Eq. 7.44, the range of the elements in **P** matrix can be obtained, as shown in Fig. 7.5. Each different colour line draws the outline of the elements' range in **P** matrix, which satisfies one matrix inequality in Eq. 7.37 - Eq. 7.43. The satisfying elements of **P** matrix, which meet the demands of all the conditions of Eq. 7.37 - Eq. 7.43, should be selected in the common area of above seven outlines, as shown in the shaded area in Fig. 7.5 [KTIT92].

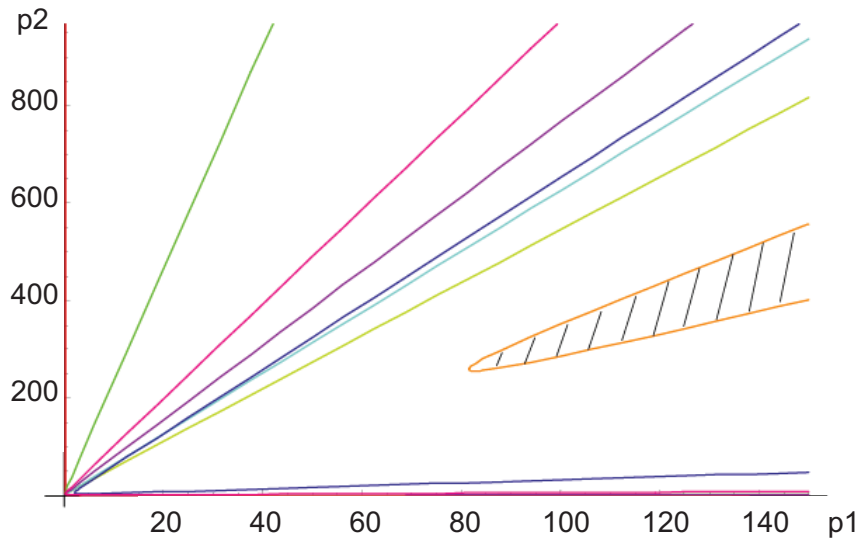

Figure 7.5: Range of the elements in **P** matrix

Here, the positive definite matrix **P** is chosen to be:

$$\mathbf{P} = \begin{bmatrix} 130 & 1 \\ 1 & 400 \end{bmatrix}$$

The stability conditions Eq. 7.34 and Eq. 7.35 or equally Eq. 7.37 - Eq. 7.43 are easily verified to be satisfied with the selected **P** matrix. In other words, the fuzzy control system Eq. 7.32, which consists of the four-rule fuzzy model Eq. 7.30 and the PDC controller Eq. 7.31 is globally asymptotically stable.

According to Eq. 7.31, the resulting PDC fuzzy controller regarding the real control variables: d and f_{sn}, can be represented below:

If $0 \leq i_{Leff} \leq a$, then

$$\begin{cases} d = w_1(i_{Leff})(-1.55211\ \delta i_{Lsn} + 0.9936\ \delta i_{Lcn}) \\ f_{sn} = \text{const.} \end{cases} \tag{7.45}$$

If $a \leq i_{Leff} \leq 2a$, then

$$\begin{cases} d = w_1(i_{Leff})(-1.55211\ \delta i_{Lsn} + 0.9936\ \delta i_{Lcn}) \\ f_{sn} = w_2(i_{Leff})(0.2057\ \delta i_{Lsn} + 0.8010\ \delta i_{Lcn}) \end{cases} \tag{7.46}$$

If $2a \leq i_{Leff} \leq 3a$, then

$$\begin{cases} d = \text{const.} \\ f_{sn} = w_2(i_{Leff})(0.2057\ \delta i_{Lsn} + 0.8010\ \delta i_{Lcn}) + w_3(i_{Leff})(0.02094\ \delta i_{Lsn} + 0.4257\ \delta i_{Lcn}) \end{cases} \tag{7.47}$$

If $3a \leq i_{Leff} \leq 4a$, then

$$\begin{cases} d = \text{const.} \\ f_{sn} = w_3(i_{Leff})(0.02094\ \delta i_{Lsn} + 0.4257\ \delta i_{Lcn}) + w_4(i_{Leff})(0.1591\ \delta i_{Lsn} + 0.1487\ \delta i_{Lcn}) \end{cases} \tag{7.48}$$

7.6 Simulated Results of T-S Fuzzy Controller

Before the launch of the VLF HV generator prototype, a simulated study about the model-based fuzzy control is implemented. Fig. 7.6 represents the simulated control block diagram. From which, it can be seen that the effective resonant current i_{Leff} is selected as the control object. Based on the reference signal i^*_{Leff} and the actual i_{Leff}, the error signal δi_{Leff} is produced, which is one of the control inputs, the other two are the Fourier coefficients of the actual resonant current: i_{Ls} and i_{Lc}. There are two control outputs: δf_s and δd. Based on which, the real control variables: f_s and d are further derived with consideration of the respective steady-state bias: F_s and D. The actual i_{Leff} and the corresponding Fourier coefficients: i_{Ls} and i_{Lc}, are measured from the plant and send back to comprise the feedback loop.

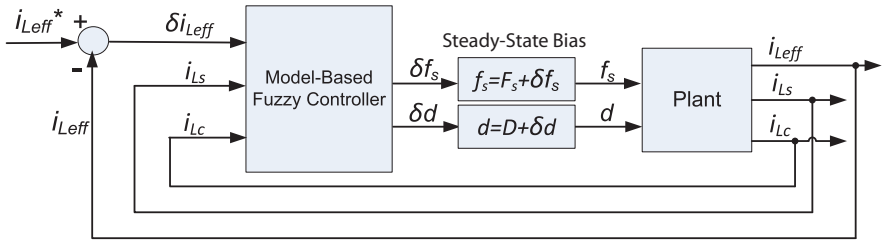

Figure 7.6: Simulated control block diagram of model-based fuzzy controller

In order to verify the performance of the model-based fuzzy controller, various reference signals are provided, and the corresponding simulation results are presented below, respectively. Fig. 7.7 represents the simulated effective resonant current i_{Leff} (pink) under given pulsing reference signal i^*_{Leff} (blue). The amplitude of i^*_{Leff} alternates between 0.4 A and 3.0 A with 50 % duty cycle, the pulsing period is 1 ms. The simulated effective resonant current i_{Leff} tracks i^*_{Leff} in about 0.1 ms with a little spike, the control performance is satisfying.

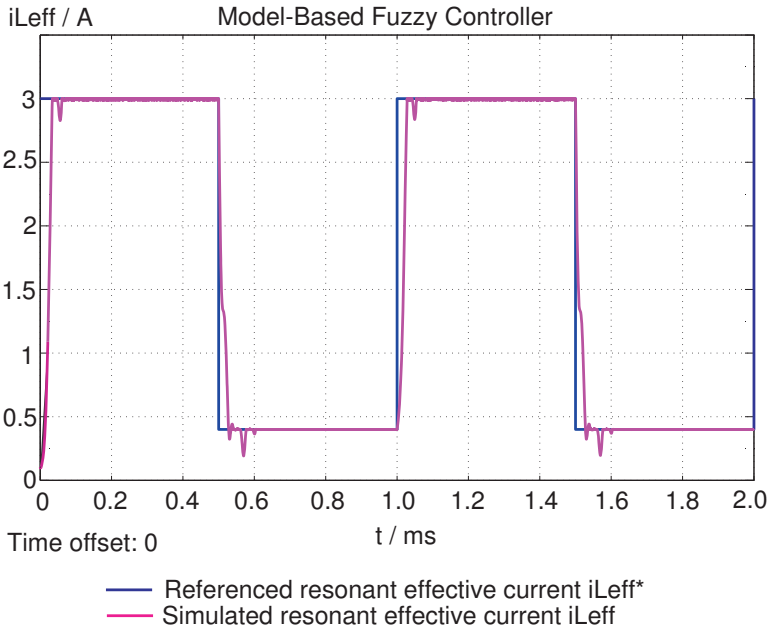

Figure 7.7: Simulated i_{Leff} under pulsing reference signal i^*_{Leff} with amplitude alternating between 0.4 A and 3.0 A with 50 % duty cycle and 1 ms period. Refer to Fig. 5.8 and Fig. 6.6 for comparison.

Fig. 7.8 shows the simulated effective resonant current i_{Leff} (pink) under given

sinusoidal reference signal i^*_{Leff} (blue) with the changing magnitude from 0.0 A and 3.0 A, and with the increasing frequency from 100 Hz to 2000 Hz in 4 ms. With the model-based fuzzy controller, the simulated effective resonant current i_{Leff} agrees with the sinusoidal reference signal i^*_{Leff} perfectly.

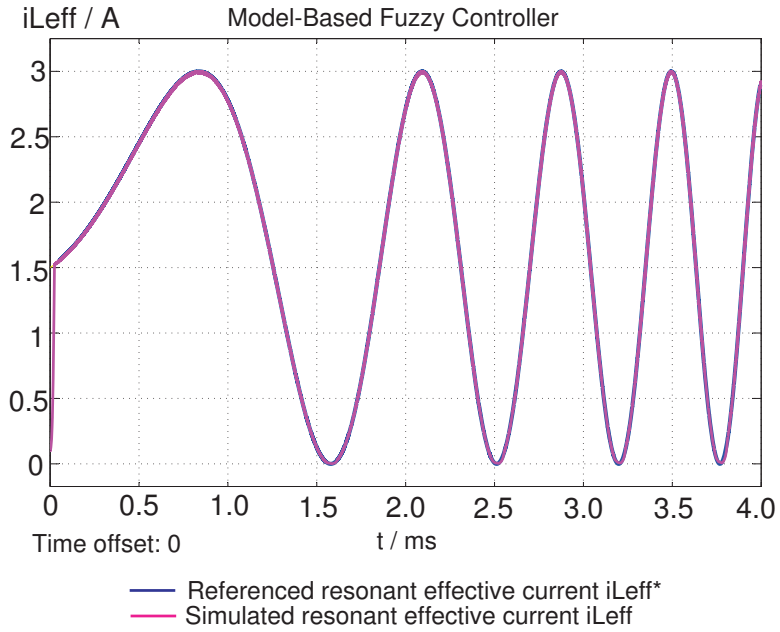

Figure 7.8: Simulated i_{Leff} under sinusoidal reference signal i^*_{Leff} with magnitudes change from 0.0 A and 3.0 A, and frequency changes from 100 Hz to 2000 Hz in 4 ms. Refer to Fig. 5.9 and Fig. 6.7 for comparison.

Fig. 7.9 provides not only the simulated effective resonant current i_{Leff} (pink) under given step changed reference signal i^*_{Leff} (blue), but also gives the corresponding Fourier coefficients of the resonant current: i_{Ls} and i_{Lc}. It is obvious that the simulated effective resonant current i_{Leff} tracks the step changed reference signal i^*_{Leff} in about 20 μs without overshoot or steady-state error. i_{Leff}, i_{Ls} and i_{Lc} arrive their respective equilibrium after the transient step change, which verifies that the LCC resonant converter with the designed model-based fuzzy controller is asymptotically stable in the large.

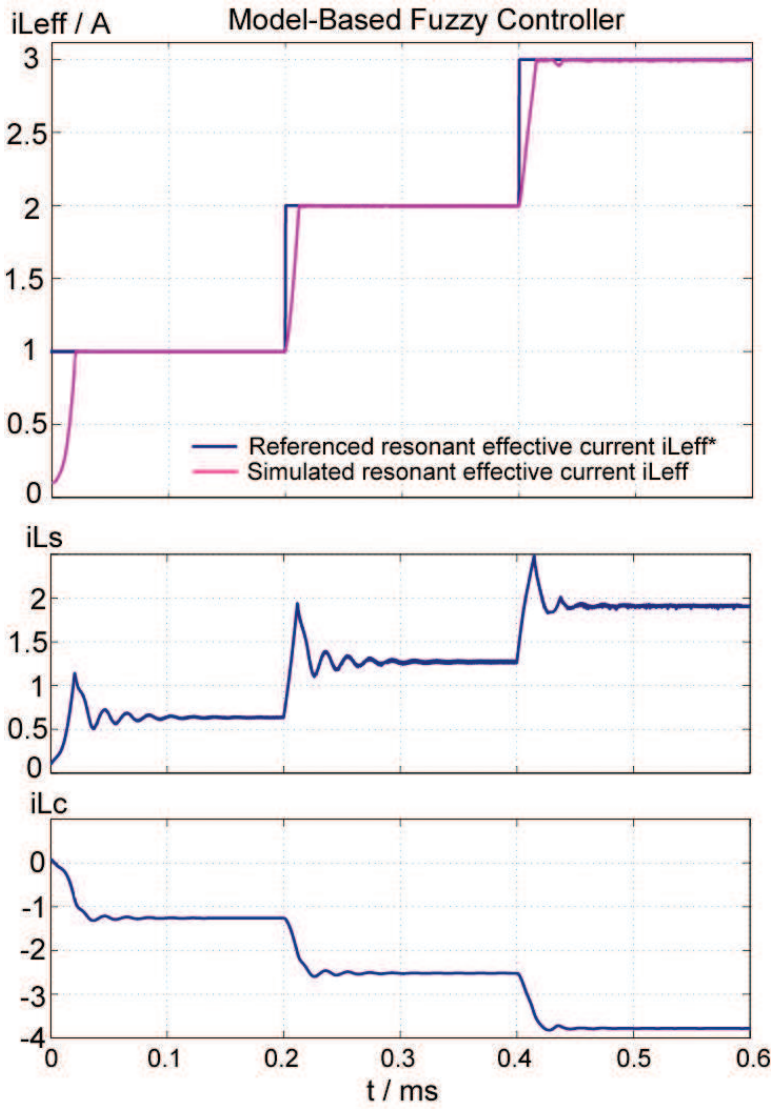

Figure 7.9: Simulated i_{Leff} and corresponding Fourier coefficients: i_{Ls}, i_{Lc} under step changed reference signal i^*_{Leff}

From above simulations, the control performance of the model-based fuzzy controller is verified through various amplitude and frequency reference signals. The simulated results agree well with the expected reference signals: the settling time is extraordinary short with nearly no overshoot or steady-state error. The intermediate variables, such as the Fourier coefficients of the resonant current: i_{Ls} and i_{Lc}, are also supervised during the simulation, which further ensures the

correctness of the model-based fuzzy control design.

7.7 Real-Time Implementation Issues and Experimental Verification

A. Estimator

The present scaled-down prototype adopts an economic DSP and a spare Analog-to-Digital converter, which is subject to a limited computing capacity and a low sampling rate. Based on such hardware, it is difficult to directly measure or real-time compute the Fourier coefficients of the resonant current: i_{Ls} and i_{Lc}. An appropriate estimator is expected to approximate them without additional complex hardware or software modification.

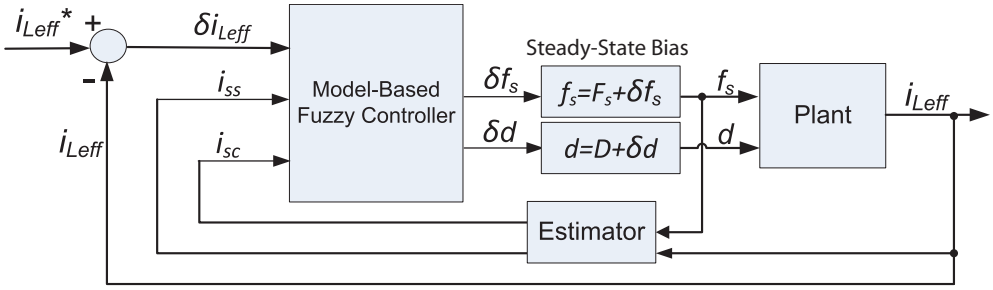

Figure 7.10: Actual experimental control block diagram with estimator

The actual control block diagram with an estimator is shown in Fig. 7.10. Compared with the simulated control block diagram Fig. 7.6, the actual one has a little deviation: i_{Ls} and i_{Lc} are not derived or measured from the plant, but replaced with i_{ss} and i_{sc}, which are estimated from the measured i_{Leff} and the corresponding f_s.

The design principle of the estimator is derived based on the LCC resonant converter large-signal model (refer to Chapter 3.2). Since the Fourier coefficients of the resonant current can be represented as:

$$\begin{array}{rcl} i_{ss} & \approx & \sqrt{2}\, i_{Leff} \cos(\varphi) \\ i_{sc} & \approx & -\sqrt{2}\, i_{Leff} \sin(\varphi) \end{array} ,$$

also the formula for φ is:

$$\varphi = \arctan\left[\frac{\pi + \frac{C_p}{C_s}\pi - C_p L_s \pi \omega_s^2 - \theta_{ss} + \frac{1}{2}\sin(2\theta_{ss})}{C_p \pi R_s \omega_s + \sin^2(\theta_{ss})}\right],$$

among which, $\theta_{ss} = 2\arctan\left[\sqrt{\frac{2\pi}{R_o \Omega_s C_p}}\right]$ and $\Omega_s = 2\pi f_s$. For a specified LCC resonant converter, L_s, C_s, C_p, R_o, R_s are constant, that is to say, θ_{ss} is only dependent on the switching frequency f_s. Summarizing above results, the Fourier coefficients of the resonant current: i_{ss} and i_{sc}, are functions of i_{Leff} and f_s:

$$\begin{array}{rcl} i_{ss} & \approx & \sqrt{2}\, i_{Leff}\cos(\varphi) \propto f_1(i_{Leff}, f_s) \\ i_{sc} & \approx & -\sqrt{2}\, i_{Leff}\sin(\varphi) \propto f_2(i_{Leff}, f_s) \end{array}.$$

It is then possible and reasonable to obtain i_{ss} and i_{sc} according to the measured i_{Leff} and corresponding f_s.

For instance, when i_{Leff} is between 0.0 A and 3.0 A, according to the PDC controller (Eq. 7.45), the estimator is only dependent on i_{Leff} due to the constant f_s in this operating region. If f_s is kept on 55 kHz, i_{ss} and i_{sc} can be approximated as below.

$$\begin{array}{rcl} i_{ss} & \approx & i_{Leff}/1.5625 \\ i_{sc} & \approx & i_{Leff} * (-1.26) \end{array}$$

With above simple estimator, it is easy to implement the model-based fuzzy controller on the prototype.

First, the estimator is verified through simulation, Fig. 7.11 shows the simulated results with step-changed reference signal. It can be seen that the estimator works well and the model-based fuzzy controller has excellent control performance even compared with the aforementioned simulation results in Fig. 7.9, which measures i_{Ls} and i_{Lc} directly from the plant.

Based on the scaled-down prototype (Fig. 6.8), experimental results of the model-based T-S fuzzy controller with the estimator can be obtained. As shown in Fig. 7.12, with 0.1 A reference resonant effective current signal, Ch1 shows the measured transient resonant current $i_L(t)$, Ch2 represents the output voltage $u_o(t)$, Ch3 is the measured voltage $u_s(t)$, and Ch4 shows the voltage $u_{AB}(t)$.

The actual resonant effective current i_{Leff} can be derived from the measured resonant current $i_L(t)$, with consideration of the oscilloscope setup: 10.0 mV/div,

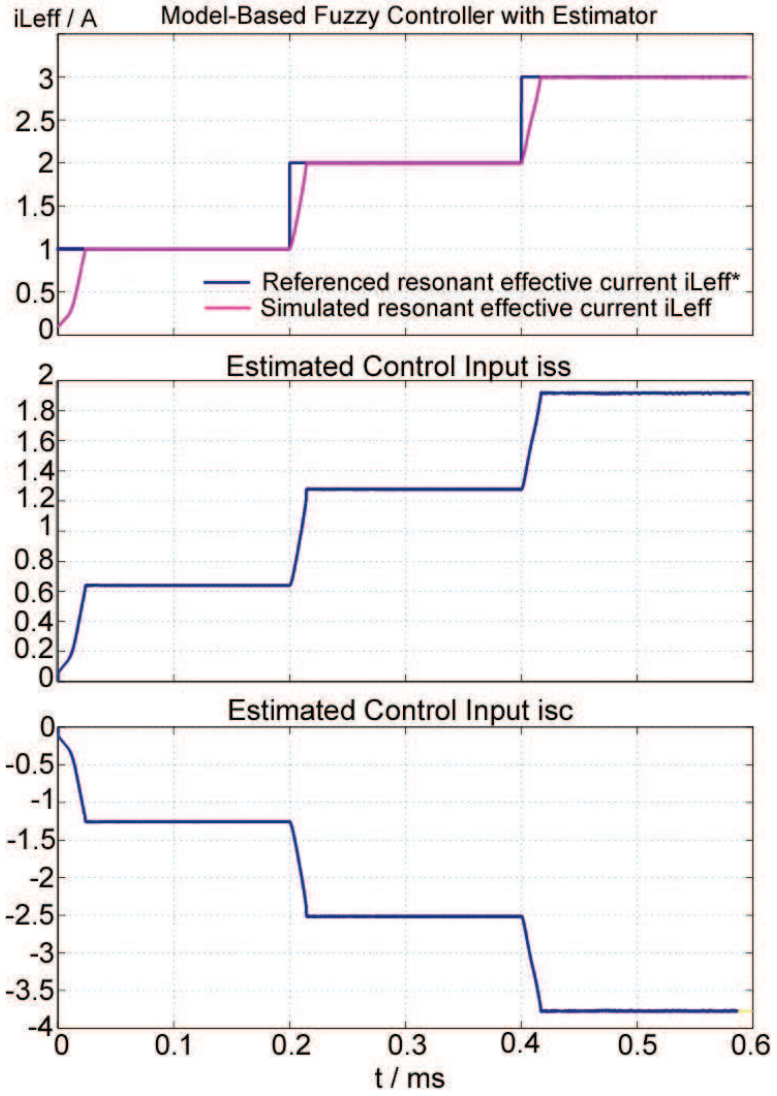

Figure 7.11: Simulated results of model-based fuzzy controller with Fourier coefficients estimator

and the current probe setup: 200 mA/div.

$$i_{Leff} = \frac{5.06 \text{ mV}}{10 \text{ mV/div}} * 200 \text{ mA/div} = 101.2 \text{ mA} = 0.1012 \text{ A}$$

$$e_{iLeff} = \frac{0.1012\ \text{A} - 0.1\ \text{A}}{0.1\ \text{A}} * 100\ \% = 1.2\ \%$$

The experimental resonant effective current $i_{Leff} = 0.1012$ A agrees well with the reference resonant effective current $i^*_{Leff} = 0.1$ A. The average steady-state deviation is about 1.2 %.

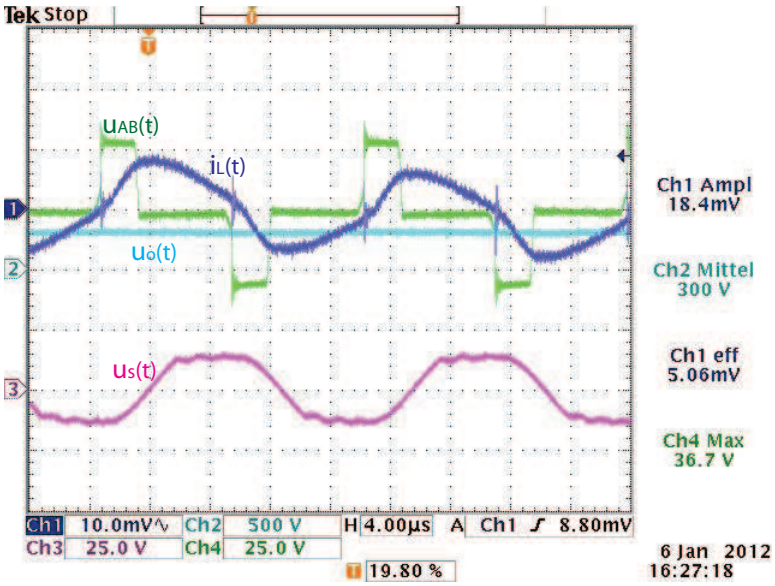

Figure 7.12: Experimental results of model-based fuzzy controller with reference effective resonant current $i^*_{Leff} = 0.1$ A, $U_{in} = 30$ V; current probe is set as 200 mA/div; Ch1 (blue) is $i_L(t)$; Ch2 (light blue) is $u_o(t)$; Ch3 (purple) is $u_s(t)$; Ch4 (green) is $u_{AB}(t)$.

7.8 Summary

A model-based T-S fuzzy controller is investigated and developed in this Chapter. Some complex theory and knowledge, such as T-S fuzzy model, PDC scheme, stability analysis via LMIs, and reduced-model techniques are adopted for the controller design. Some actions are taken for real-time implementation, such as Fourier coefficients estimator. From the simulated results, it can be seen that the model-based T-S fuzzy controller has outstanding control performance compared with those of the linear PI controller and model-free fuzzy PD controller in both dynamic and static aspects: the settling time is about some μs and the control

bandwidth is up to several thousand Hz without static error or overshoot. The provided experimental results further validate the success of the developed CPM T-S fuzzy controller.

Due to the limited hardware of the scaled-down laboratory prototype, for example, the inner current-mode closed-loop has just 1 ms sampling rate, most of the simulation results and the excellent performance of the T-S fuzzy controller are not presented in the experimental results. Furthermore, considering the safety issues and due to some technical limitation, only some operating points in a small operation region of the inner CPM control loop are measured, the outer voltage control loop is not included in the measurement.

Chapter 8

Conclusion

Based on the investigations and achievements in this dissertation, the following conclusions can be drawn.

1. Based on the state-of-the-art investigation, the LCC resonant converter with step-up high voltage transformer, symmetrical CW multiplier and a controllable discharge circuit is thought to be the preferable topology for the VLF HV generator application with consideration of feasibility, portability, controllability and extendibility.

2. Through the research of the steady-state characteristics of a more-stage symmetrical CW multiplier, conclusions can be drawn that the voltage drop of a CW multiplier is predicable, which has a proportional relationship with the output current, the CW multiplier capacitor, the switching frequency; and has the exponential relationship with the stage number.

   The output voltage of a k-stage symmetrical CW multiplier can be approximated as k-times of that of the one-stage CW multiplier with consideration of the predicable increasing voltage drop. If the steady-state difference due to the different stage-number can be neglected, the control-to-output dynamic characteristics of the more-stage and the corresponding one-stage CW multipliers are almost the same under the specified conditions. Based on such results, adopting a simplified one-stage symmetrical CW multiplier to replace the more-stage one in modeling is regarded to be feasible.

3. Based on the control-to-output transfer functions comparison of the LCC resonant converter with a capactive load and a voltage source load, conclusions can be drawn that adopting an equivalent voltage source load to replace the original capacitive load in the LCC resonant converter can simplify the modeling process with almost the same steady-state and dynamic characteristics.

4. Based on the developed computer aided design (CAD) and optimization (CAO) environment, it is feasible for industry to realize the large-signal simulation, computer aided design, and multi-objective optimization. Using the derived Pareto front, it is easy for industry to make the final decision with consideration of multi-objectives. Those achievements would promote automated system development and enhance the market competence. The resulting computer aided design (CAD) and optimization (CAO) environment make a long term positive impact on industry.

5. A novel control strategy, which combines separate switching frequency control mode and duty cycle control mode together, is adopted in the LCC resonant converter. The simulated and experimental results verify and validate its correctness, which realizes the wide operation region and closed-loop control stability. Such method is appropriate not only in linear control scheme, but also in nonlinear control scheme, for combining multiple control variables together.

6. Conventional linear PI controller has been primarily designed for the LCC resonant converter because this classic technique is still the most popular and widely adopted method due to its simple structure, ease of design, and low cost in implementation. The provided simulation and experimental results verified and validated its correctness. But its shortage is also obvious: it cannot perform satisfactorily for the nonlinear system with a wide operating region, its control performance is highly dependent on the operating points.

7. Conventional fuzzy control is well-known for its ability to handle nonlinearities and uncertainties through use of fuzzy set theory. The fuzzy control

is based on expert knowledge and intuitive experience without complex modeling, it has been proven to be a successful approach to many complex nonlinear systems. The provided simulation and experimental results verified its effectiveness.

But as a model-free control approach, it always suffers from criticism of lacking of systematic stability analysis and controller design. The control performance of the developed fuzzy PD controller has no predominance compared with that of the linear PI controller. The fuzzy controller needs additional adaptive gaining parameter for control performance improvement; the real-time implementation also needs more effort for the code optimization and memory size reduction.

8. The modern model-based Takagi-Sugeno fuzzy controller is investigated to get more satisfactory control performance. Although more complicated techniques need to be used, and the real-time implementation is relatively complex, the model-based Takagi-Sugeno fuzzy control is still thought to be a promising candidate: it utilizes the conventional linear control techniques, which guarantees the stability and the closed-loop control performance based on a systematic approach; it adopts the modern nonlinear fuzzy theory, which fuzzy "blends" each local linear system and the corresponding linear controller together. It realizes direct, simple control design and gets excellent control performance.

   From the simulated results, it can be seen that the developed model-based Takagi-Sugeno fuzzy controller has outstanding control performance compared with those of the linear PI controller and the fuzzy PD controller, especially in the aspect of dynamics and control bandwidth: the settling time is about some μs, and the control bandwidth is up to several thousand Hz. The provided experimental results validate the correctness of the model-based Takagi-Sugeno fuzzy controller.

   Regretfully, due to the hardware constraints of the scaled-down laboratory prototype, most of the simulation results and the advantages of the developed Takagi-Sugeno fuzzy controller cannot be completely demonstrated,

the superiority of the Takagi-Sugeno fuzzy controller are not explicitly represented. A comprehensive measurement is expected for further validation of the model-based Takagi-Sugeno fuzzy controller.

Accomplishments in this dissertation, such as modeling, multi-objective optimization, developed CAD-CAO environment, conventional and modern controller development, are not only suitable for the LCC resonant converter applied in VLF high voltage generator, but also appropriate for other similar applications using resonant converters, such as high voltage X-Ray generator, DC power supply with wide output voltage range, and so on.

It should be especially highlighted that the model-based Takagi-Sugeno fuzzy control development in this dissertation is an original contribution to adopt a nonlinear model-based fuzzy control scheme in power supply field with realized prototype measurements.

Bibliography

[Bal59] E. Baldinger. *"Kaskadengeneratoren", Handbuch der Physik, Instrumentelle Hilfsmittel der Kernphysik I.* Springer-Verlag, 1959.

[BBK09] Juergen Biela, Uwe Badstuebner, and Johann W. Kolar. Design of a 5 kW, 1 U, 10 kW/dm^3 resonant dc-dc converter for telecom applications. *IEEE Transactions on Power Electronics*, VOL. 24, NO. 7, JULY 2009.

[BKS95] Piero P. Bonissone, Pratap S. Khedkar, and Michael J. Schutten. Fuzzy logic control of resonant converters for power supplies. *Control Applications, Proceedings of the 4th IEEE Conference*, 1995.

[Bru71] J. S. Brugler. Theoretical performance of voltage multiplier circuits. *IEEE Journal of Solid-State Circuits*, June 1971.

[BWM92] Maria D. Bellar, Edson H. Watonabe, and Antonio C. Mesquita. Analysis of the dynamic and steady-state performance of cockcroft-walton cascade rectifier. *IEEE Transactions on Power Electronics*, Vol.7, No.3, July 1992.

[Ce08] Edwin K. P. Chong and etc. *An Introduction to Optimization, Third Edition.* A John Wiley&Sons, Inc., Publication, 2008.

[CFB09a] Z. Cao, N. Fröhleke, and J. Böcker. Control design for a very low-frequency high-voltage test system. *Proc. EPE*, 2009.

[CFB09b] Z. Cao, N. Fröhleke, and J. Böcker. Converter and control design for very low-frequency high-voltage test systems. *Proc. ECCE*, 2009.

BIBLIOGRAPHY

[CFOW78] A. Capel, G. Ferrante, D. O'Sullivan, and A. Weinberg. Application of the injected current model for the dynamic analysis of switching regulators with the new concept of LC^3 modulator. *IEEE Power Electronics Specialists Conference*, pp. 135-147, 1978.

[CHFB10] Z. Cao, M. Hu, N. Fröhleke, and J. Böcker. Modeling and control design for a very low-frequency high-voltage test system. *IEEE Transactions on Power Electronics 25(2)*, pp. 1068-1077, 2010.

[Deird] C. Deisch. Simple switching control method changes power converter into a current source. *IEEE Power Electronics Specialists Conference*, pp. 300-306, 1978 Record.

[DJCW08] Xudong Ding, Lei Jia, Wenjian Cai, and Changyun Wen. Dynamic modeling and model order reduction for vapor compression cycle. *2008 Chinese Control and Decision Conference (CCDC 2008), IEEE*, 2008.

[DK01] Kind Dieter and Feser Kurt. High-voltage test techniques, translator y. narayana rao, newses. *ISBN 0-7506-5183-0*, 2001.

[ea94] S. Boyd et. al. Linear matrix inequalities in systems and control theory. *SIAM, Philadelphia, PA*, 1994.

[ECM82] R. W. Erickson, S. Cuk, and R. D. Middlebrook. Large-scale modelling and analysis of switching regulators. *IEEE PESC Rec.*, pp. 240-250, 1982.

[EM00] R.-W. Erickson and D. Maksimovic. *Fundamentals of Power Electronics 2nd Edition*. Kluwer Academic Publishers, 2000.

[Fen06] Gang Feng. A survey on analysis and design of model-based fuzzy control systems. *IEEE Transactions on Fuzzy systems*, Vol.14, No. 5, October 2006.

[FJ05] Cavalcante F.S. and Kolar J.W. Small-signal model of a 5kw high-output voltage capacitive-loaded series-parallel resonant dc-dc converter. *Power Electronics Specialists Conference, PESC'05, IEEE 36th.*, 2005.

[FR96] C. Fantuzzi and R. Rovatti. On the approximation capabilities of the homogeneous takagi-sugeno model. *in Proc. 5th IEEE Int. Conf. Fuzzy Systems, New Orleans, LA*, pp. 1067-1072, 1996.

[GA04] SERKAN GUGERCIN and ATHANASIOS C. ANTOULAS. A survey of model reduction by balanced truncation and some new results. *Taylor - Francis*, INT. J. CONTROL, VOL. 77, NO. 8, 748-766, 20 MAY 2004.

[Gan07] Pablo Gandara. The role of energy for regional integration in the emp: Strengthening institutions. *Jean Monnet Centre of Excellence, Freie Universität Berlin, Germany*, Dec. 2007.

[GBL11] Juergen Gausemeier, Oliver Buschjost, and Markus Lehner. The future of cable testing ensuring a secure global power grid. *International Association for Management of Technology, IAMOT 2011 Proceedings*, 2011.

[Gre14] H. Greinacher. The lonometer and its application to the measurement of radium and roetgen rays. *Physikal. Zeitsch.*, vol 15, 1914.

[HBF11] M. Hu, J. Böcker, and N. Fröhleke. Frequency / duty cycle current-mode fuzzy control for lcc resonant converter. *IEEE European Conference on Power Electronics and Applications, EPE*, 2011.

[HFB09a] M. Hu, N. Fröhleke, and J. Böcker. Frequency / duty cycle control of lcc resonant converter supplying high voltage very low frequency test systems. *IEEE European Conference on Power Electronics and Applications (EPE)*, 2009.

[HFB09b] M. Hu, N. Fröhleke, and J. Böcker. Small-signal model and control design of lcc resonant converter with a capacitive load applied in very low frequency high voltage test system. *IEEE Energy Conversion Congress and Expo (ECCE)*, 2009.

[HFB11] M. Hu, N. Fröhleke, and J. Böcker. Multi-objective optimization of lcc resonant converter applied in vlf hv generator. *Conference of the IEEE Industrial Electronics Society (IECON)*, 2011.

[HGB00] William Gerard Hurley, Eugene Gath, and John G. Breslin. Optimizing the ac resistance of multilayer transformer windings with arbitrary current waveforms. *IEEE Transactions on Power Electronics*, VOL.15, NO. 2, MARCH 2000.

[Je08] J JMesserly and etc. "Blank map of Europe.svg" by maix, which is based on "Europe countries.svg" by tintazul. *Licensed under the Creative Commons Attribution-Share Alike 3.0 Unported license*, 20 Dec. 2008.

[JPGT] Albert Jenni, Michael Pasquier, Roger Gleyvod, and Peter Thommen. Testing of high voltage power cables with series resonant systems and water terminations.

[JSMS00] T. A. Johansen, R. Shorten, and R. Murray-Smith. On the interpretation and identification of dynamic takagi-sugeno models. *IEEE Trans. Fuzzy Syst.*, vol. 8, no. 3, pp. 297-313, Juni 2000.

[KBW+10] J. W. Kolar, J. Biela, S. Waffler, T. Friedli, and U. Badstuebner. Performance trends and limitations of power electronic systems. *2010 6th International Conference on Integrated Power Electronics Systems (CIPS)*, 16-18 March 2010.

[KTIT92] Shunji Kawamoto, Kensho Tada, Atsushi Ishigama, and Tsuneo Taniguchi. An approach to stability analysis of second order fuzzy systems. *IEEE*, 1992.

[LMR94] Antonio Lamantia, Piero G. Maranesi, and Luca Radrizzani. Small-signal model of the cockcroft-walton voltage multiplier. *IEEE Transations on Power Electronics*, VOL. 9, NO. I, January 1994.

[MC76] R. D. Middlebrook and S. Cuk. A general unified approach to modeling switching power converter stages. *IEEE PESC Rec.*, pp. 18-34, 1976.

[Moh08] Peter Mohaupt. Neues verfahren zur erzeugung einer vlf prüfspannung für anwendungen im hoch- und höchstspannungsbereich. *TF 05 HV Test and Measuring Technique on Site, Mallorca*, March 2008.

[Moo81] B. C. Moore. Principal component analysis in linear systems: controllability, observability, and model reduction. *IEEE trans. Automat. Contr.*, Vol. AC-26, pp. 17-32, 1981.

[MRDP+07] Juan A. Martin-Ramos, Juan Diaz, Alberto M. Pernia, Juan Manuel Lopera, and Fernando Nuno. Dynamic and steady-state models for the prc-lcc resonant topology with a capacitor as output filter. *IEEE Transactions on Industrial Electronics*, Vol.54, No.4, pp.2262-2275, August 2007.

[N.Na] N.N. Ac resonant test systems for on-site testing of extruded hv cables. HIGHVOLT Prüftechnik Dresden GmbH, Dresden, Gemany.

[N.Nb] N.N. Vlf related standards: Vde din 0276-620, ieee p400.2, vde din 0276-621, cenelec hd 620 and cenelec hd 621.

[NN94] Yu. Nesterov and A. Nemirovsky. Interior-point polynomial methods in convex programming. *SIAM, Philadelphia, PA*, 1994.

[N.N95] N.N. Analysis and design of fuzzy control systems using dynamic fuzzy global models. *Fuzzy Sets Syst.*, vol. 75, pp. 47-62, 1995.

[N.N97a] N.N. Analysis and design for a class of complex control systems - part i: Fuzzy modeling and identification. *Automatica*, vol. 33, pp. 1017-1028, 1997.

[N.N97b] N.N. Analysis and design for a class of complex control systems - part ii: Fuzzy controller design. *Automatica*, vol. 33, pp. 1029-1039, 1997.

[N.N98] N.N. General siso takagi-sugeno fuzzy systems with linear rule consequent are universal approximators. *IEEE Trans. Fuzzy Syst.*, vol. 6, no. 4, pp. 582-587, November 1998.

[OL85] R. Oruganti and F. C. Lee. State plane analysis of parallel resonant converters. *IEEE PESC Rec.*, pp. 56-73, 1985.

[OPS01] Heiko Osterbolz, Cornelius Paul, and Philips Medical Systems. Study of resonant high-voltage cascaded circuits with different numbers of stages. *Simulation in Drive Technology, Power Electronics and Automotive Engineering. SIMPLORER Workshop*, 2001.

[OYL87] R. Oruganti, J.ames J. Yang, and Fred C. Lee. Implementation of optimal trajectory control of series resonant converter. *IEEE PESC Rec.*, pp. 451-459, 1987.

[PDH96] Rainer Palm, Dimiter Driankov, and Hans Hellendoorn. Model based fuzzy control - fuzzy gain schedulers and sliding mode fuzzy controllers. *Springer*, 1996.

[PY97] Kevin M. Passino and Stephen Yurkovich. Fuzzy control. *ADDISON-WESLEY*, 1997.

[RCL98] R. B. Ridley, B. H. Cho, and F. C. Lee. Analysis and interpretation of loop gains of multi-loop-controlled switching regulator. *IEEE Transactions on Power Electronics*, pp.489-497, 1998.

[Rei] Richard Reid. High voltage vlf test equipment with sinusoidal waveform.

[RS98] Leopoldo Rossetto and Giorgio Spiazzi. Seris resonant converter with wide load range. *Industry Applications Conference. Thirty-Third IAS Annual Meeting. The 1998 IEEE*, 1998.

[Sie08] Siemens. Challenges and solutions for high voltage transmission. *Sector Energy*, Oct. 2008.

[SK86] M. Sugeno and G. T. Kang. Fuzzy modeling and control of multilayer incinera-tor. *Fuzzy Sets Syst.*, No. 18, pp. 329-346, 1986.

[SKSC08] S. Seesanga, W. Kongnun, A. Sangswang, and S. Chotigo. A new type oft he vlf high voltage generator. *King Mongkut's University of Technology Thonburi, Thailand. Proceedings of ECTI-CON*, 2008.

[SNL+91] S. R. Sanders, J. M. Noworolski, X. Z. Liu, , and G. Verghese. Generalized averaging method for power conversion circuits. *IEEE Transactions on Power Electronics*, vol. 6, no.2, pp.251-259, April 1991.

[Ste88] Robert L. Steigerwald. A comparison of half-bridge resonant converter topologies. *IEEE Transactions on Power Electronics*, Vol. 3, No. 2, April 1988.

[Sug99] M. Sugeno. On stability of fuzzy systems expressed by fuzzy rules with singleton consequents. *IEEE Trans. Fuzzy Syst.*, vol. 7, no. 2, pp.201-224, April 1999.

[THW03] Kazuo Tanaka, Tsuyoshi Hori, and Hua O. Wang. A multiple lyapunov function appraoch to stabilization of fuzzy control systems. *IEEE Transactions on Fuzzy Systems*, VOl.11, No.4, August 2003.

[TS85] T. Takagi and M. Sugeno. Fuzzy identification of systems and its pplications to modeling and control. *IEEE Trans. Syst., Man, Cybern.*, vol. SMC-15, no. 1, pp. 116-132, Jan./Feb. 1985.

[TS92a] K. Tanaka and M. Sano. 4 design method of fuzzy servo systems. *Proc. of 8th Fuzzy System Symposium*, pp. 501-504, 1992.

[TS92b] K. Tanaka and M. Sugeno. Stability analysis and design of fuzzy control systems. *FUZZY SETS AND SYSTEMS*, 45, 110.2, pp. 135-156, 1992.

[TS92c] K. Tanaka and M. Sugeno. Stability analysis and design of fuzzy control systems. *Fuzzy Sets Syst.*, Vol. 45, No. 2, pp. 135-156, 1992.

[TS93] K. Tanaka and M. Sano. Concept of stability margin for fuzzy systems and design of robust fuzzy controllers. *Proc. of 2nd IEEE Int. Con. on Fuzzy Systems*, 1993.

[TTW97] Kazuo TANAKA, Tadanari TANIGUCHI, and Hua O. WANG. Model-based fuzzy control for two trailers problem: Stability analyiss and design via linear matrix inequalities. *IEEE*, 1997.

[TW01] KAZUO TANAKA and HUA O. WANG. Fuzzy control systems design and analysis - a linear matrix inequality approach. *A Wiley-Interscience Publication, John Wiley&Sons, INC.*, 2001.

[uMG07] BAUR Prüf und Messtechnik GmbH. Schaltungsanordnung zur erzeugung einer prüfspannung für die prüfung elektrischer betriebsmittel. *German Patent DE 19513441*, 03.07.2007.

[VC83] V. Vorperian and S. Cuk. Small signal analysis of resonant converters. *IEEE PESC Rec.*, pp. 269-282, 1983.

[VEK86] G. C. Verghese, M. E. Elbuluk, and J. G. Kassakian. A general approach to sampled-data modeling for power electronic circuits. *IEEE Transactions on Power Electronics*, pp. 76-89, April 1986.

[WTG95a] H. O. Wang, K. Tanaka, and M. F. Griffin. An analytical framework of fuzzy modeling and control of nonlinear systems: Stability and design issues. *Proc.1995 American Control Conference, Seattle*, pp. 2272-2276, 1995.

[WTG95b] H. O. Wang, K. Tanaka, and M. F. Griffin. Parallel distributed compensation of nonlinear systems by takagi-sugeno fuzzy model. *Proc. FUZZ-IEEE/IFES'95*, pp. 531-538, 1995.

[YCL+92] Eric X. Yang, Byungcho Choi, Fred C. Lee, , and Bo H. Cho. Dynamic analysis and control design of lcc resonant converter. *Power Electronics Specialists Conference, PESC'92, 23rd Annual IEEE*, Vol.1, pp.362-369, 1992.

[YLJ91] Eric X. Yang, Fred C. Lee, and M.M. Jovanovic. Extended describing function technique applied to the modelling of resonant converters. *Proc. VPEC*, pp.179-191, 1991.

[YLJ92] Eric Yang, Fred C. Lee, and Milan M. Jovanovic. Small-signal modeling of lcc resonant converter. *Virginia Power Electronics Center*, 1992.

[Zad65] L. A. Zadeh. Fuzzy sets. *Inform. Control*, vol. 8, pp. 338-353, 1965.

[Zad75] L. A. Zadeh. The concept of a linguistic variable and its application to approximate reasoning: I, ii, iii. *Inform. Sci.*, vol. 8, pp. 199-251, 1975.

[ZZX00] K. Zeng, N. Y. Zhang, and W. L. Xu. A comparative study on sufficient conditions for takagi-sugeno fuzzy systems as universal approximators. *IEEE Trans. Fuzzy Syst.*, vol. 8, no. 6, pp. 773-780, December 2000.

Appendix A

Quasi-Steady-State Solutions

Based on the large-signal model in Section 3.2, the quasi-steady-state solutions are as follows:

$$I_{Ls} = \frac{8U_e K_2}{4K_1^2 + K_2^2} \tag{A.1}$$

$$I_{Lc} = \frac{16U_e K_1}{4K_1^2 + K_2^2} \tag{A.2}$$

$$I_{Lp} = \sqrt{I_{Ls}^2 + I_{Lc}^2} \tag{A.3}$$

$$U_{ss} = \frac{I_{Lc}}{C_s\,\Omega_s} \tag{A.4}$$

$$U_{sc} = -\frac{I_{Ls}}{C_s\,\Omega_s} \tag{A.5}$$

$$U_o = \frac{I_{Lp} R_o\,(1 - \cos\theta_{ss})}{2\pi} \tag{A.6}$$

$$I_{cw} = \frac{I_{Lp} - \frac{1}{2} C_p \Omega_s U_o}{\pi} \tag{A.7}$$

$$U_e = \Omega_s C_p U_{in} \sin\left(\frac{\pi D}{2}\right) \tag{A.8}$$

$$K_1 = \pi\alpha + \gamma_{ss} - \pi\alpha C_s L_s \Omega_s^2 \tag{A.9}$$

$$K_2 = -2\left(\sin^2\theta_{ss} + \pi\alpha C_s R_s \Omega_s\right) \tag{A.10}$$

$$\gamma_{ss} = \pi - \theta_{ss} + \frac{\sin(2\theta_{ss})}{2} \tag{A.11}$$

$$\theta_{ss} = 2tg^{-1}\sqrt{\frac{2\pi}{R_o C_p \Omega_s}} \tag{A.12}$$

$$\alpha = \frac{C_p}{C_s} \tag{A.13}$$

Appendix B

Non-zero Element in System Matrices: $\mathbf{A}_c$, $\mathbf{B}_c$, $\mathbf{C}_c$

Referring to Eq. 3.37, the non-zero elements in system matrices: $\mathbf{A}_c$, $\mathbf{B}_c$, $\mathbf{C}_c$, are represented below.

$$a_{11} = \frac{\frac{2I_{Ls}U_o(-I_{Ls}\cos[\theta_{ss}]+I_{Lc}\sin[\theta_{ss}])}{I_{Lp}^3} - \frac{C_p\pi R_s\Omega_s+\sin[\theta_{ss}]^2}{C_p\Omega_s}}{L_s\pi} \tag{B.1}$$

$$a_{12} = \Omega_s + \frac{2I_{Lc}U_o(-I_{Ls}\cos[\theta_{ss}] + I_{Lc}\sin[\theta_{ss}])}{I_{Lp}^3 L_s\pi} - \frac{\pi - \theta_{ss} + \cos[\theta_{ss}]\sin[\theta_{ss}]}{C_p L_s\pi\Omega_s} \tag{B.2}$$

$$a_{13} = -\frac{1}{L_s} \tag{B.3}$$

$$a_{15} = \frac{2I_{Ls}\cos[\theta_{ss}] - 2I_{Lc}\sin[\theta_{ss}]}{I_{Lp}L_s\pi} \tag{B.4}$$

$$a_{21} = -\Omega_s - \frac{2I_{Ls}U_o(I_{Lc}\cos[\theta_{ss}] + I_{Ls}\sin[\theta_{ss}])}{I_{Lp}^3 L_s\pi} + \frac{\pi - \theta_{ss} + \cos[\theta_{ss}]\sin[\theta_{ss}]}{C_p L_s\pi\Omega_s} \tag{B.5}$$

$$a_{22} = -\frac{\pi R_s + \frac{\sin[\theta_{ss}]^2}{C_p\Omega_s} + \frac{2I_{Lc}U_o(I_{Lc}\cos[\theta_{ss}]+I_{Ls}\sin[\theta_{ss}])}{I_{Lp}^3}}{L_s\pi} \tag{B.6}$$

$$a_{24} = -\frac{1}{L_s} \tag{B.7}$$

$$a_{25} = \frac{2(I_{Lc}\cos[\theta_{ss}] + I_{Ls}\sin[\theta_{ss}])}{I_{Lp}L_s\pi} \tag{B.8}$$

$$a_{31} = \frac{1}{C_s} \tag{B.9}$$

$$a_{34} = \Omega_s \tag{B.10}$$

$$a_{42} = \frac{1}{C_s} \tag{B.11}$$

$$a_{43} = -\Omega_s \tag{B.12}$$

$$a_{51} = \frac{I_{Ls}(I_{Lp} + C_p U_o \Omega_s - I_{Lp}\cos[\theta_{ss}])}{2C_L I_{Lp}^2 \pi} \tag{B.13}$$

$$a_{52} = \frac{I_{Lc}(I_{Lp} + C_p U_o \Omega_s - I_{Lp}\cos[\theta_{ss}])}{2C_L I_{Lp}^2 \pi} \tag{B.14}$$

$$a_{55} = -\frac{\frac{2}{R_o} + \frac{C_p \Omega_s}{\pi}}{2C_L} \tag{B.15}$$

$$b_{11} = \frac{4\sin\left[\frac{D\pi}{2}\right]}{L_s \pi} \tag{B.16}$$

$$b_{12} = \frac{2U_{in}\cos\left[\frac{D\pi}{2}\right]}{L_s} \tag{B.17}$$

$$\begin{aligned} b_{13} = {} & \frac{I_{Lp}I_{Lc}\left(\pi + C_p L_s \pi \Omega_s^2 - \theta_{ss}\right) - 2C_p I_{Lc} U_o \Omega_s \sin[\theta_{ss}] + I_{Lp} I_{Ls} \sin[\theta_{ss}]^2}{C_p I_{Lp} L_s \pi \Omega_s^2} \\ & + \frac{\cos[\theta_{ss}](2C_p I_{Ls} U_o \Omega_s + I_{Lp} I_{Lc}\sin[\theta_{ss}])}{C_p I_{Lp} L_s \pi \Omega_s^2} \end{aligned} \tag{B.18}$$

$$\begin{aligned} b_{23} = {} & \frac{4C_p I_{Lc} U_o \Omega_s \cos[\theta_{ss}] + 4C_p I_{Ls} U_o \Omega_s \sin[\theta_{ss}] + 2I_{Lp} I_{Lc} \sin[\theta_{ss}]^2}{2C_p I_{Lp} L_s \pi \Omega_s^2} \\ & - \frac{2I_{Lp} I_{Ls}\left(\pi + C_p L_s \pi \Omega_s^2 - \theta_{ss} + \cos[\theta_{ss}]\sin[\theta_{ss}]\right)}{2C_p I_{Lp} L_s \pi \Omega_s^2} \end{aligned} \tag{B.19}$$

$$b_{33} = U_{sc} \tag{B.20}$$

$$b_{43} = -U_{ss} \tag{B.21}$$

$$b_{53} = -\frac{C_p U_o}{2C_L \pi} \tag{B.22}$$

$$c_{21} = \frac{I_{Ls}}{I_{Lp}\pi} \tag{B.23}$$

$$c_{22} = \frac{I_{Lc}}{I_{Lp}\pi} \tag{B.24}$$

$$c_{25} = -\frac{C_p \Omega_s}{2\pi} \tag{B.25}$$

$$c_{31} = \frac{I_{Ls}}{I_{Lp}} \tag{B.26}$$

$$c_{32} = \frac{I_{Lc}}{I_{Lp}} \tag{B.27}$$

$$e_{23} = -\frac{C_p U_o}{2\pi} \tag{B.28}$$

Appendix C

Parameters in the Small-Signal Circuit Model

Referring to Fig. 3.5, the parameters in the small-signal circuit model are provided below.

$$K_v = \frac{4}{\pi}\sin\left(\frac{\pi}{2}D\right) \tag{C.1}$$

$$E_d = 2U_{in}\cos\left(\frac{\pi}{2}D\right) \tag{C.2}$$

$$M_1 = I_{Ls}\cos\left(\theta_{ss}\right) - I_{Lc}\sin\left(\theta_{ss}\right) \tag{C.3}$$

$$M_2 = I_{Lc}\cos\left(\theta_{ss}\right) + I_{Ls}\sin\left(\theta_{ss}\right) \tag{C.4}$$

$$E_s = L_s I_{Lc}\omega_0 + \frac{2U_o\omega_0 M_1}{I_{Lp}\pi\Omega_s} + \frac{I_{Ls}\omega_0\sin^2\left(\theta_{ss}\right) + I_{Lc}\omega_0\gamma_{ss}}{C_p\pi\Omega_s^2} \tag{C.5}$$

$$E_c = L_s I_{Ls}\omega_0 - \frac{2U_o\omega_0 M_2}{I_{Lp}\pi\Omega_s} + \frac{I_{Ls}\omega_0\gamma_{ss} - I_{Lc}\omega_0\sin^2\left(\theta_{ss}\right)}{C_p\pi\Omega_s^2} \tag{C.6}$$

$$Z_{Lc} = L_s\Omega_s - \frac{2I_{Lc}U_o M_1}{I_{Lp}^3\pi} - \frac{\gamma_{ss}}{C_p\pi\Omega_s} \tag{C.7}$$

$$Z_{Ls} = L_s\Omega_s + \frac{2I_{Ls}U_o M_2}{I_{Lp}^3\pi} - \frac{\gamma_{ss}}{C_p\pi\Omega_s} \tag{C.8}$$

$$Z_s = \frac{2I_{Ls}U_o M_1}{I_{Lp}^3\pi} + \frac{C_p\pi R_s\Omega_s + \sin^2\left(\theta_{ss}\right)}{C_p\pi\Omega_s} \tag{C.9}$$

$$Z_c = \frac{2I_{Lc}U_o M_2}{I_{Lp}^3\pi} + \frac{C_p\pi R_s\Omega_s + \sin^2\left(\theta_{ss}\right)}{C_p\pi\Omega_s} \tag{C.10}$$

$$K_{us} = \frac{2M_1}{I_{Lp}\pi} \tag{C.11}$$

$$K_{uc} = \frac{2M_2}{I_{Lp}\pi} \tag{C.12}$$

$$G_s = C_s\Omega_s \tag{C.13}$$

$$J_c = C_s U_{ss}\omega_0 \tag{C.14}$$

$$J_s = C_s U_{sc}\omega_0 \tag{C.15}$$

$$H_f = \frac{C_p\omega_0 U_o}{2\pi} \tag{C.16}$$

$$H_c = \frac{I_{Ls}}{I_{Lp}\pi} \tag{C.17}$$

$$H_s = \frac{I_{Lc}}{I_{Lp}\pi} \tag{C.18}$$

$$H_u = \frac{C_p\Omega_s}{2\pi} \tag{C.19}$$

Appendix D

Non-Zero Element in Normalized System Matrices: $\mathbf{A}_{cn}$, $\mathbf{B}_{cn}$, $\mathbf{C}_{cn}$

Referring to Eq. 3.44, the non-zero elements in normalized system matrices: $\mathbf{A}_{cn}$, $\mathbf{B}_{cn}$, $\mathbf{C}_{cn}$, are represented below.

$$a_{11n} = -Q_s\Omega_0 - \frac{2I_{Lsn}^2 U_{on}\Omega_0 \cos[\theta_{ss}]}{I_{Lpn}^3\pi]} + \frac{2I_{Lcn}I_{Lsn}U_{on}\Omega \sin[\theta_{ss}]}{I_{Lpn}^3\pi} - \frac{\sin[\theta_{ss}]^2}{C_pF_{sn}\pi Z} \tag{D.1}$$

$$a_{12n} = \frac{I_{Lpn}^3(-\pi + C_pF_{sn}^2\pi\Omega_0 Z + \theta_{ss}) + 2C_pF_{sn}I_{Lcn}^2U_{on}\Omega_0 Z\sin[\theta_{ss}]}{C_pF_{sn}I_{Lpn}^3\pi Z} - \frac{\cos[\theta_{ss}](2C_pF_{sn}I_{Lcn}I_{Lsn}U_{on}\Omega_0 Z + I_{Lpn}^3\sin[\theta_{ss}])}{C_pF_{sn}I_{Lpn}^3\pi Z} \tag{D.2}$$

$$a_{13n} = -\Omega_0 \tag{D.3}$$

$$a_{15n} = \frac{2\Omega_0(I_{Lsn}\cos[\theta_{ss}] - I_{Lcn}\sin[\theta_{ss}])}{I_{Lpn}\pi} \tag{D.4}$$

$$a_{21n} = \frac{-4C_pF_{sn}I_{Lcn}I_{Lsn}U_{on}\Omega_0 Z\cos[\theta_{ss}] - 4C_pF_{sn}I_{Lsn}^2U_{on}\Omega_0 Z\sin[\theta_{ss}]}{2C_pF_{sn}I_{Lpn}^3\pi Z} + \frac{I_{Lpn}^3(2\pi - 2C_pF_{sn}^2\pi\Omega_0 Z - 2\theta_{ss} + \sin[2\theta_{ss}])}{2C_pF_{sn}I_{Lpn}^3\pi Z} \tag{D.5}$$

$$a_{22n} = -Q_s\Omega_0 - \frac{2I_{Lcn}^2U_{on}\Omega_0\cos[\theta_{ss}]}{I_{Lpn}^3\pi} - \frac{2I_{Lcn}I_{Lsn}U_{on}\Omega_0\sin[\theta_{ss}]}{I_{Lpn}^3\pi} - \frac{\sin[\theta_{ss}]^2}{C_pF_{sn}\pi Z} \tag{D.6}$$

D. NON-ZERO ELEMENT IN NORMALIZED SYSTEM MATRICES: $\mathbf{A}_{CN}$, $\mathbf{B}_{CN}$, $\mathbf{C}_{CN}$

$$a_{24n} = -\Omega_0 \tag{D.7}$$

$$a_{25n} = \frac{2\Omega_0(I_{Lcn}\cos[\theta_{ss}] + I_{Lsn}\sin[\theta_{ss}])}{I_{Lpn}\pi} \tag{D.8}$$

$$a_{31n} = \frac{C_g\Omega_0}{C_s} \tag{D.9}$$

$$a_{34n} = F_{sn}\Omega_0 \tag{D.10}$$

$$a_{42n} = \frac{C_g\Omega_0}{C_s} \tag{D.11}$$

$$a_{43n} = -F_{sn}\Omega_0 \tag{D.12}$$

$$a_{51n} = \frac{I_{Lsn}\Omega_0(C_gI_{Lpn} + C_pF_{sn}U_{on} - C_gI_{Lpn}\cos[\theta_{ss}])}{2C_LI_{Lpn}^2\pi} \tag{D.13}$$

$$a_{52n} = \frac{I_{Lcn}\Omega_0(C_gI_{Lpn} + C_pF_{sn}U_{on} - C_gI_{Lpn}\cos[\theta_{ss}])}{2C_LI_{Lpn}^2\pi} \tag{D.14}$$

$$a_{55n} = -\frac{(2C_g\pi + C_pF_{sn}Q)\Omega_0}{2C_L\pi Q} \tag{D.15}$$

$$b_{11n} = \frac{4\Omega_0\sin[\frac{D\pi}{2}]}{\pi} \tag{D.16}$$

$$b_{12n} = 2\Omega_0\cos[\frac{D\pi}{2}] \tag{D.17}$$

$$\begin{aligned} b_{13n} = {} & \frac{I_{Lcn}I_{Lpn}(\pi + C_pF_{sn}^2\pi\Omega_0Z - \theta_{ss}) - 2C_pF_{sn}I_{Lcn}U_{on}\Omega_0Z\sin[\theta_{ss}]}{C_pF_{sn}^2I_{Lpn}\pi Z} \\ & + \frac{I_{Lpn}I_{Lsn}\sin[\theta_{ss}]^2 + \cos[\theta_{ss}](2C_pF_{sn}I_{Lsn}U_{on}\Omega_0Z + I_{Lcn}I_{Lpn}\sin[\theta_{ss}])}{C_pF_{sn}^2I_{Lpn}\pi Z} \end{aligned} \tag{D.18}$$

$$\begin{aligned} b_{23n} = {} & \frac{4C_pF_{sn}I_{Lcn}U_{on}\Omega_0Z\cos[\theta_{ss}] + 4C_pF_{sn}I_{Lsn}U_{on}\Omega_0Z\sin[\theta_{ss}] + 2I_{Lcn}I_{Lpn}\sin[\theta_{ss}]^2}{2C_pF_{sn}^2I_{Lpn}\pi Z} \\ & - \frac{2I_{Lpn}I_{Lsn}(\pi + C_pF_{sn}^2\pi\Omega_0Z - \theta_{ss} + \cos[\theta_{ss}])\sin[\theta_{ss}])}{2C_pF_{sn}^2I_{Lpn}\pi Z} \end{aligned} \tag{D.19}$$

$$b_{33n} = U_{scn}\Omega_0 \tag{D.20}$$

$$b_{43n} = -U_{ssn}\Omega_0 \tag{D.21}$$

$$b_{53n} = -\frac{C_pU_{on}\Omega_0}{2C_L\pi} \tag{D.22}$$

$$c_{21n} = \frac{I_{Lsn}}{I_{Lpn}\pi} \tag{D.23}$$

$$c_{22n} = \frac{I_{Lcn}}{I_{Lpn}\pi} \tag{D.24}$$

$$c_{25n} = -\frac{C_p F_{sn}}{2C_g \pi} \tag{D.25}$$

$$c_{31n} = \frac{I_{Lsn}}{I_{Lpn}} \tag{D.26}$$

$$c_{32n} = \frac{I_{Lcn}}{I_{Lpn}} \tag{D.27}$$

$$e_{23n} = -\frac{C_p U_{on}}{2C_g \pi} \tag{D.28}$$

Appendix E

Copper Loss Analysis Considering Eddy Current Effect

According to [EM00] and [HGB00], for the purpose of determining leakage inductance and winding eddy current, a layer consisting of N_p turns of round wire carrying current $i_p(t)$ can be approximately modeled as an effective single turn of foil, which carries current $Np \cdot i_p(t)$. The steps of transforming a layer of round conductors into a foil conductor are explained in Fig. E.1(a) - Fig. E.1(d).

From Fig. E.1(a) and (b), since the approximated square conductors have the same copper cross-sectional area as the round conductors, the thickness h of the square conductors can be represented as:

$$h = \sqrt{\frac{\pi}{4}} \cdot d \tag{E.1}$$

These square conductors are then joined together into a foil layer (Fig. E.1(c)). Further, the width of the foil is expanded so that it spans the width of the core window l_w (Fig. E.1(d)).

Since this stretching process increases the conductor cross-sectional area, the resistivity ρ' and skin depth δ' in the final foil layer has the following relationship with the original resistivity ρ and skin depth δ in the round conductors.

$$\rho' = \frac{\rho}{\eta} \tag{E.2}$$

$$\delta' = \frac{\delta}{\sqrt{\eta}} \tag{E.3}$$

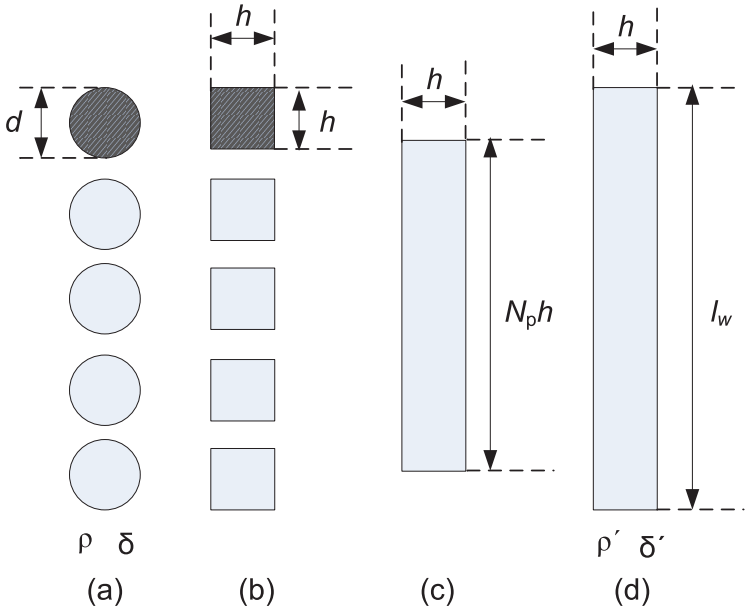

Figure E.1: Approximating a layer of round conductors as an effective foil conductor

The winding porosity η is:

$$\eta = \frac{N_p \cdot h^2}{h \cdot l_w} = \sqrt{\frac{\pi}{4}} \cdot d \cdot \frac{N_p}{l_w} \in (0, 1) \tag{E.4}$$

In the following analysis, the factor φ for foil conductors is defined as:

$$\varphi = \frac{h}{\delta'} = \frac{\sqrt{\pi/4} \cdot d}{\delta/\sqrt{\eta}} = \sqrt{\eta \cdot \frac{\pi}{4}} \cdot \frac{d}{\delta} \tag{E.5}$$

The average power loss P in a uniform layer of thickness h can be determined based on Maxwell's equations and the following assumptions [EM00]:

1. The component of the magnetic field normal to the conductor surface is zero;

2. Sinusoidal waveforms are assumed and rms magnitudes are employed;

3. The magnetic field strengths on the left and right sides of the conductor are denoted $H(0)$ and $H(h)$, respectively; these magnetic fields are driven by the magnetomotive forces (MMF) $F(0)$ and $F(h)$, respectively, as shown in Fig. E.2;

4. $H(0)$ and $H(h)$ are in phase.

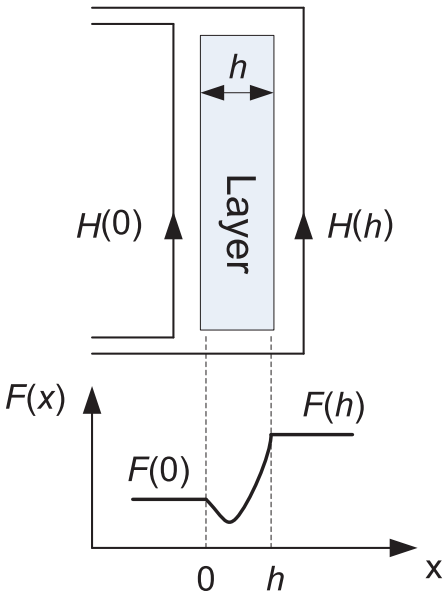

Figure E.2: The power loss for a uniform layer, uniform tangential magnetic fields $H(0)$ and $H(h)$ are applied to the layer surfaces

The resulting P is represented as follows:

$$P = R_{dc} \cdot \frac{\varphi}{{N_p}^2} \left[(F^2(h) + F^2(0)) G_1(\varphi) - 4F(h)F(0)G_2(\varphi) \right] \tag{E.6}$$

where N_p is the number of turns in the layer, R_{dc} is the DC resistance of the layer. The functions $G_1(\varphi)$ and $G_2(\varphi)$ are

$$G_1(\varphi) = \frac{\sinh(2\varphi) + \sin(2\varphi)}{\cosh(2\varphi) - \cos(2\varphi)} \tag{E.7}$$

$$G_2(\varphi) = \frac{\sinh(\varphi)\cos(\varphi) + \cosh(\varphi)\sin(\varphi)}{\cosh(2\varphi) - \cos(2\varphi)} \tag{E.8}$$

If the winding carries current of rms magnitude I_{rms}, then

$$F(h) - F(0) = N_p \cdot I_{rms} \tag{E.9}$$

$$F(h) = m \cdot N_p \cdot I_{rms} \tag{E.10}$$

$$\frac{F(0)}{F(h)} = \frac{m-1}{m} \tag{E.11}$$

The layer number m is therefore the ratio of the MMF $F(h)$ to the layer ampere-turns $N_p \cdot I_{rms}$.

Based on Eq. E.6 - Eq. E.11, the factor between the power loss P and the low-frequency copper loss $R_{dc} \cdot {I_{rms}}^2$ in a layer can be derived:

$$\frac{P}{R_{dc} \cdot {I_{rms}}^2} = \frac{P}{P_{dc}} = \varphi[(2m^2 - 2m + 1)G_1(\varphi) - 4m(m-1)G_2(\varphi)] \tag{E.12}$$

Appendix F

Overview of General Control Design Process

Based on the conventional control theory and techniques, the formulating description for a general control design process of a continuous-time nonlinear system is briefly represented below.

Considering a nonlinear open-loop system of the form:

$$\dot{\mathbf{x}}(t) = \mathbf{f}(\mathbf{x}(t), \mathbf{u}(t)). \tag{F.1}$$

Let $\mathbf{X}_d$ be a given operating point and $\mathbf{U}_d$ be the correspondingly input. Note that $\mathbf{X}_d$ and $\mathbf{U}_d$ are not functions of time, while $\mathbf{x}(t)$ and $\mathbf{u}(t)$ are functions of time. By introducing the new state vector $\delta\mathbf{x}(t)$ and the new input vector $\delta\mathbf{u}(t)$:

$$\delta\mathbf{x}(t) = \mathbf{x}(t) - \mathbf{X}_d, \tag{F.2}$$

$$\delta\mathbf{u}(t) = \mathbf{u}(t) - \mathbf{U}_d, \tag{F.3}$$

the equivalent modified nonlinear open-loop system can be obtained:

$$\delta\dot{\mathbf{x}}(t) + \dot{\mathbf{X}}_d = \mathbf{f}(\delta\mathbf{x}(t) + \mathbf{X}_d, \delta\mathbf{u}(t) + \mathbf{U}_d). \tag{F.4}$$

The linearized version of above modified nonlinear open-loop system Eq. F.4 at $(\mathbf{X}_d, \mathbf{U}_d)$ can be derived as

$$\delta\dot{\mathbf{x}}(t) + \dot{\mathbf{X}}_d = \mathbf{f}(\mathbf{X}_d, \mathbf{U}_d) + \mathbf{A}(\mathbf{X}_d, \mathbf{U}_d) \cdot \delta\mathbf{x}(t) + \mathbf{B}(\mathbf{X}_d, \mathbf{U}_d) \cdot \delta\mathbf{u}(t), \tag{F.5}$$

where

$$\mathbf{A}(\mathbf{X}_d, \mathbf{U}_d) = \left(\frac{\partial \mathbf{f}(\mathbf{x}, \mathbf{u})}{\partial \mathbf{x}} \right)_{\mathbf{x}=\mathbf{X}_d, \mathbf{u}=\mathbf{U}_d},$$

$$\mathbf{B}(\mathbf{X}_d, \mathbf{U}_d) = \left(\frac{\partial \mathbf{f}(\mathbf{x}, \mathbf{u})}{\partial \mathbf{u}} \right)_{\mathbf{x}=\mathbf{X}_d, \mathbf{u}=\mathbf{U}_d},$$

are the Jacobian matrices of $\mathbf{f}(\mathbf{x}(t), \mathbf{u}(t))$ evaluated at $(\mathbf{X}_d, \mathbf{U}_d)$.

Since

$$\dot{\mathbf{X}}_d = \mathbf{f}(\mathbf{X}_d, \mathbf{U}_d), \tag{F.6}$$

Eq. F.5 can be rewritten as a linearized small-signal model form:

$$\delta\dot{\mathbf{x}}(t) = \mathbf{A}(\mathbf{X}_d, \mathbf{U}_d) \cdot \delta\mathbf{x}(t) + \mathbf{B}(\mathbf{X}_d, \mathbf{U}_d) \cdot \delta\mathbf{u}(t). \tag{F.7}$$

If the corresponding control law is of the following form:

$$\delta\mathbf{u}(t) = -\mathbf{K}(\mathbf{X}_d, \mathbf{U}_d) \cdot \delta\mathbf{x}(t), \tag{F.8}$$

where $\mathbf{K}(\mathbf{X}_d, \mathbf{U}_d)$ denotes the gain matrix, which is dependent on the operating point $(\mathbf{X}_d, \mathbf{U}_d)$, by inserting the control law Eq. F.8 into the linearized open-loop system Eq. F.7, the resulting closed-loop system is obtained:

$$\delta\dot{\mathbf{x}}(t) = \lfloor \mathbf{A}(\mathbf{X}_d, \mathbf{U}_d) - \mathbf{B}(\mathbf{X}_d, \mathbf{U}_d) \cdot \mathbf{K}(\mathbf{X}_d, \mathbf{U}_d) \rfloor \cdot \delta\mathbf{x}(t). \tag{F.9}$$

Since

$$\delta\mathbf{x}(t) = \mathbf{x}(t) - \mathbf{X}_d,$$

$$\delta\dot{\mathbf{x}}(t) = \dot{\mathbf{x}}(t) - \dot{\mathbf{X}}_d,$$

and

$$\dot{\mathbf{X}}_d = 0,$$

Eq. F.9 is equivalent to the following form:

$$\dot{\mathbf{x}}(t) = \lfloor \mathbf{A}(\mathbf{X}_d, \mathbf{U}_d) - \mathbf{B}(\mathbf{X}_d, \mathbf{U}_d) \cdot \mathbf{K}(\mathbf{X}_d, \mathbf{U}_d) \rfloor \cdot (\mathbf{x}(t) - \mathbf{X}_d). \tag{F.10}$$

From linear control theory, the control law for which $\mathbf{X}_d$ is the asymptotically stable equilibrium of Eq. F.10 should be such that $\mathbf{A}(\mathbf{X}_d, \mathbf{U}_d) - \mathbf{B}(\mathbf{X}_d, \mathbf{U}_d) \cdot \mathbf{K}(\mathbf{X}_d, \mathbf{U}_d)$ is a Hurwitz matrix [PDH96].

Appendix G

Continuous Lyapunov Equation Solutions

The continuous Lyapunov equation solution can be obtained in MATLAB, syntax P=lyap(A, H) is adopted to solve the Lyapunov equation Eq. 7.10. Among which, P=$\mathbf{P}$, A=$\mathbf{A}$, H=$\mathbf{BB}^T$. Some results are extracted from MATLAB and represented below. The LCC resonant converter has the following parameters: $C_s = 200$ nF, $C_p = 50$ nF, $L_s = 500$ μH, $C_L = 10$ nF, $R_s = 1$ Ω.
On the operating point: $Q = 3$, $F_{sn} = 0.899$, $D = 0.373$.

$$\mathbf{A} = \begin{bmatrix} -0.4038 & 0.8285 & -1.0000 & 0 \\ -0.7934 & -0.0097 & 0 & -1.0000 \\ 0.2000 & 0 & 0 & 0.8990 \\ 0 & 0.2000 & -0.8990 & 0 \end{bmatrix} \tag{G.1}$$

$$\mathbf{H} = \begin{bmatrix} 3.6951 & 0.8711 & 0.1732 & -0.2599 \\ 0.8711 & 0.8264 & 0.1643 & -0.2466 \\ 0.1732 & 0.1643 & 0.0327 & -0.0490 \\ -0.2599 & -0.2466 & -0.0490 & 0.0736 \end{bmatrix} \tag{G.2}$$

» P=lyap(A,H)

$$\mathbf{P} = \begin{bmatrix} 6.2206 & 0.8996 & 0.0808 & -0.9995 \\ 0.8996 & 4.7370 & 0.4878 & -0.3465 \\ 0.0808 & 0.4878 & 0.8902 & -0.0362 \\ -0.9995 & -0.3465 & -0.0362 & 1.0586 \end{bmatrix} \tag{G.3}$$

» eig(P)

$$ans = \begin{bmatrix} 6.8497 \\ 4.3640 \\ 0.8636 \\ 0.8291 \end{bmatrix} \tag{G.4}$$

On the other operating point: $Q = 20$, F_{sn} =1.019, $D = 0.536$.

$$\mathbf{A} = \begin{bmatrix} -0.7572 & 0.8636 & -1.0000 & 0 \\ -0.4632 & -0.0625 & 0 & -1.0000 \\ 0.2000 & 0 & 0 & 1.0190 \\ 0 & 0.2000 & -1.0190 & 0 \end{bmatrix} \tag{G.5}$$

$$\mathbf{H} = \begin{bmatrix} 2.5802 & 4.5581 & 0.5620 & -0.4954 \\ 4.5581 & 25.7789 & 3.1785 & -2.8015 \\ 0.5620 & 3.1785 & 0.3919 & -0.3454 \\ -0.4954 & -2.8015 & -0.3454 & 0.3045 \end{bmatrix} \tag{G.6}$$

» P=lyap(A,H)

$$\mathbf{P} = \begin{bmatrix} 37.3719 & 39.2874 & 6.9229 & -7.4270 \\ 39.2874 & 53.6799 & 8.8315 & -8.6638 \\ 6.9229 & 8.8315 & 2.8536 & -1.5511 \\ -7.4270 & -8.6638 & -1.5511 & 2.9169 \end{bmatrix} \tag{G.7}$$

» eig(P)

$$ans = \begin{bmatrix} 88.6893 \\ 5.4323 \\ 1.3969 \\ 1.3038 \end{bmatrix} \tag{G.8}$$